STUDY OF FLOW ACCELERATED CORROSION OF CARBON STEEL PIPELINE IN OILFIELD ENVIRONMENT

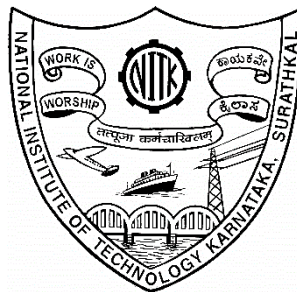Thesis

Submitted in partial fulfilment of the requirements for the degree of

DOCTOR OF PHILOSOPHY

by

AJMAL T S

DEPARTMENT OF METALLURGICAL AND

MATERIALS ENGINEERING

NATIONAL INSTITUTE OF TECHNOLOGY KARNATAKA

SURATHKAL, MANGALORE, INDIA - 575025

OCTOBER, 2021

D E C L A R A T I O N

I hereby *declare* that the Research Thesis entitled "**Study of Flow Accelerated Corrosion of Carbon Steel Pipeline in Oilfield Environment**" which is being submitted to the National Institute of Technology Karnataka, Surathkal in partial fulfillment of the requirements for the award of the Degree of **Doctor of Philosophy** in the Department of Metallurgical and Materials Engineering, is a *bonafide report of the research work carried out by me*. The material contained in this Research Thesis has not been submitted to any University or Institution for the award of any degree.
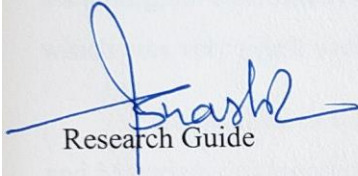
Place: Surathkal, India

Date: 18th October 2021

Ajmal T S

145021MT14F01

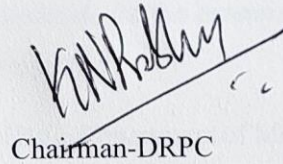Department of Metallurgical and Materials Engineering

CERTIFICATE

This is to *certify* that the Research Thesis entitled **"Study of Flow Accelerated Corrosion of Carbon Steel Pipeline in Oilfield Environment"** submitted by **Mr. Ajmal T S (Register Number: 145021MT14F01)** as the record of the research work carried out by him, is *accepted as the Research Thesis submission* in partial fulfillment of the requirements for the award of degree of **Doctor of Philosophy**.

Research Guide

Dr. Shashi Bhushan Arya
Assistant Professor
Department of Metallurgical
and Materials Engineering
NITK, Surathkal

Chairman-DRPC

Department of Metallurgical
and Materials Engineering
NITK, Surathkal

Chairman - DRPC
Dept. of Metallurgical and Materials Engineering
National Institute of Technology Karntaka, Surathkal
Post Srinivasnagar, Mangaluru - 575 025
Karnataka, India

ACKNOWLEDGEMENT

Dedicated to my beloved wife and son

TABLE OF CONTENTS

ABSTRACT

Flow accelerated corrosion (FAC) and erosion-corrosion (EC) are the major reasons for steel pipeline failure in the oil and gas industry. The present thesis focuses on the FAC and EC study of API X70 steel in a synthetic solution of oilfield water under a turbulent flow condition. The tests were carried out at a more critical location (90° pipe elbow) in a circulating loop system at a fixed flow velocity of 3 m s^{-1}. Multiple electrodes were located at intrados (inner face) and extrados (outer face) of the 90° pipe elbow.

The influence of flow on corrosion (FAC) and passivation was examined using potentiodynamic polarization tests and electrochemical impedance spectroscopy (EIS) tests. Corrosion rates of the electrodes located at the intrados are more than that at the extrados. Shear stresses are simulated using the CFD method and it is observed that the corrosion rate is inversely proportional to shear stresses. The effect of oleic acid hydrazide (OAH), a green inhibitor on X70 steel was investigated for the first time under flow condition. The maximum inhibition efficiency is found at 87.7% (extrados electrode E4) for 0.30 g/L OAH concentration. The studied inhibitor is good in the protection of the API X70 steel with higher efficiency in the dynamic corrosive environment.

The laser surface melting (LSM) technique is used to examine the corrosion behavior of X70 steel using laser powers of 2, 2.5, and 3 kW. It is found that the resistance against FAC of the X70 steel is significantly improved by surface modification. LSM treated X70 steel exhibited higher corrosion resistance than untreated and inhibitor-used conditions. Slurry erosion-corrosion behavior by electrochemical and weight loss measurements for both untreated and laser melted samples located at the 90° elbow test section was tested and compared. Laser surface melted samples exhibited improved hardness with enhanced EC resistance as compared to that of untreated counterparts due to alteration of surface metallurgy.

Keywords: Flow accelerated corrosion (FAC), Erosion-corrosion (EC), API X70 steel, Oleic acid hydrazide (OAH) inhibitor, Laser surface melting (LSM).

List of Figures

List of Tables

List of Abbreviations

FAC	Flow Accelerated Corrosion
EC	Erosion-corrosion
NACE	National Association of Corrosion Engineers
ASTM	American Society for Testing and Materials
AISI	American Iron and Steel Institute
MTR	Mass Transfer Rate
HSLA	High Strength Low Alloy
API	American Petroleum Institute
CRA	Corrosion-Resistant Alloy
TMP	Thermomechanical processing
OES	Optical Emission Spectroscopy
CFD	Computational Fluid Dynamics
RCE	Rotating Cylinder Electrode
RDE	Rotating Disk Electrode
MIC	Microbiologically Influenced Corrosion
UDC	Under Deposit Corrosion
OAH	Oleic Acid Hydrazide
EIS	Electrochemical Impedance Spectroscopy
WE	Working Electrode
CE	Counter Electrode
RE	Reference Electrode
SCE	Saturated Calomel Electrode

OCP   Open Circuit Potential

LSM   Laser Surface Melting

UT   Untreated

LSA   Laser Surface Alloying

LTH   Laser Transformation Hardening

EDM   Electrical Discharge Machining

SEM   Scanning Electron Microscope

XPS   X-ray Photoelectron Spectroscopy

EDS   Energy Dispersive X-Ray Spectroscopy

XRD   X-ray diffraction

JCPDS   Joint Committee on Powder Diffraction Standards

EBSD   Electron backscatter diffraction

AFM   Atomic Force Microscopy

OP   Optical Profilometry

SYMBOLS

ρ Density

μ Dynamic viscosity

v Kinematic viscosity

$\math₵$ Centerline of pipe

τ Shear stress

η Inhibition Efficiency

β_c Cathodic Tafel slope

β_a Anodic Tafel slope

1 INTRODUCTION

1.1 Pipeline corrosion and its impact on the oil and gas industry

In the oil and gas industry, fractional distillation of energy-containing products from crude oil and natural gas often entails drilling and transportation from the wells to refineries (Papavinasam 2014a). Pipelines are considered the most significant transportation mode for the oil and gas industry (Karami 2012). A schematic of upstream field installation of the oil and gas industry is illustrated in Figure 1.1 (Palacios 2016). It primarily includes a reservoir, wellhead, process plants, and storage tanks connected with pipelines.
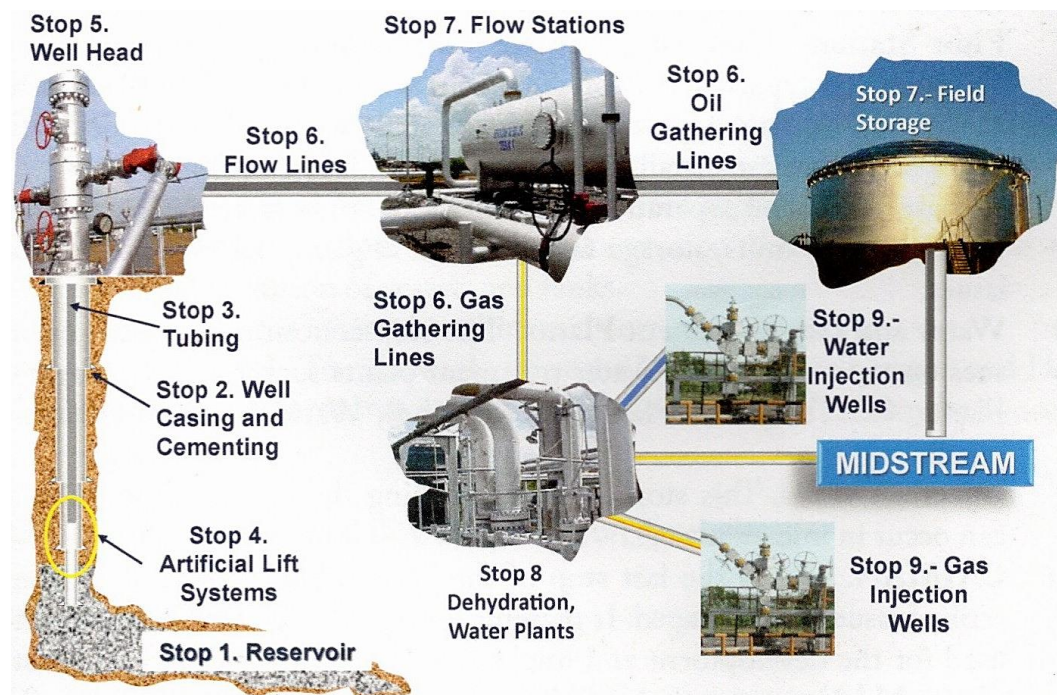
Figure 1.1 Schematic of upstream installation of oil and gas industry

The hydrocarbon products handling pipelines in offshore and onshore oil and gas networks need to be more reliable, economical, and safe during the whole operations (Kennedy 1993). But unfortunately, many a time, pipeline corrosion leads to catastrophic failures and enormous economic loss to the oil and gas industry, nuclear power stations, and chemical process industry (Dooley and Chexal 2000). Figure 1.2(a) represents a catastrophic pipeline failure at Ghislenghien city, Belgium, in 2004, which caused many fatalities (Ossai et al. 2015). Another incident [Figure 1.2(b, c)]

occurred at the Kaohsiung city, South Taiwan, in 2014, killed 25 people and injured more than 259 others (Ossai et al. 2015). Figure 1.3 depicts a catastrophic failure of an overhead pipeline at the Humber Refinery (United Kingdom) in 2001 (Carter et al. 2006). After a detailed investigation, it was found that the cause of the pipeline failure was the erosion-corrosion of 6 inch diameter 90° elbow (Carter et al. 2006). Similarly, in a GAIL pipeline leakage and explosion that occurred in 2014 in Nagaram village in the East Godavari district of Andhra Pradesh, 23 lives were lost and many people got injured. The root cause of this failure is due to internal corrosion of 18 inch diameter steel pipeline (Lakshmi and Kumar 2015).

Figure 1.2 Some catastrophic pipeline failures occurred at, (a) Belgium, (b) and (c) Taiwan (Ossai et al. 2015)

Failed 90° elbow

Figure 1.3 Catastrophic failure of an overhead pipeline

Corrosion is a naturally occurring phenomenon commonly defined as the deterioration of a material (usually a metal) that results from a chemical or electrochemical reaction with its environment (NACE/ASTM 2012). Material properties such as microstructure and hardness influence pipeline corrosion to a greater extent. Therefore, material selection for the pipeline depending upon its application is very important. Modification of metal surface which is directly in contact with the solution by changing the surface metallurgy or surface chemistry or by adding a surface layer or coating can improve the corrosion and erosion resistance of pipeline material. The environment can affect corrosion by governing the electrochemical reactions. The pipeline corrosion can be controlled by adding a chemical substance in the appropriate concentration in the environment (fluid) which can alter the electrochemical reactions without changing the fundamental properties of the fluid. The hydrodynamics behavior of the fluid flow (environment) is also playing a vital role in pipeline corrosion. Components (such as elbow, tee, orifice, and reducer) with increased turbulence levels due to their design are more susceptible to corrosion.

2 LITERATURE REVIEW

2.1 Causes and types of pipeline corrosion

Pipeline corrosion occurs due to several reasons which consist of physical, chemical, and environmental factors. The major factors influencing pipeline corrosion are summarized in Figure 2.1 (Ossai et al. 2015). The physical factors are classified as structural (material properties, crevices, inclusions, etc.) and product (temperature, pressure, flow rate, flow pattern, etc.) properties. However, chemical factors are controlled by pH, dissolved solids, Sulphur, H_2S, CO_2, microorganisms. Environmental factors are the most important factors which consist of oilfield composition, soil composition, temperature and moisture level, and nature of the operating area. There are various types of corrosion problems that could be encountered in the oilfield pipelines which are significantly influenced by the factors which are well reported by Palacios (Palacios 2016).

- ❖ Pitting corrosion
- ❖ Under Deposit Corrosion (UDC)
- ❖ Microbiologically Influenced Corrosion (MIC)
- ❖ Crevice Corrosion
- ❖ Galvanic Corrosion
- ❖ Cavitation
- ❖ Impingement
- ❖ CO_2 Corrosion
- ❖ H_2S Corrosion
- ❖ Flow Accelerated Corrosion (FAC)
- ❖ Erosion Corrosion (EC)
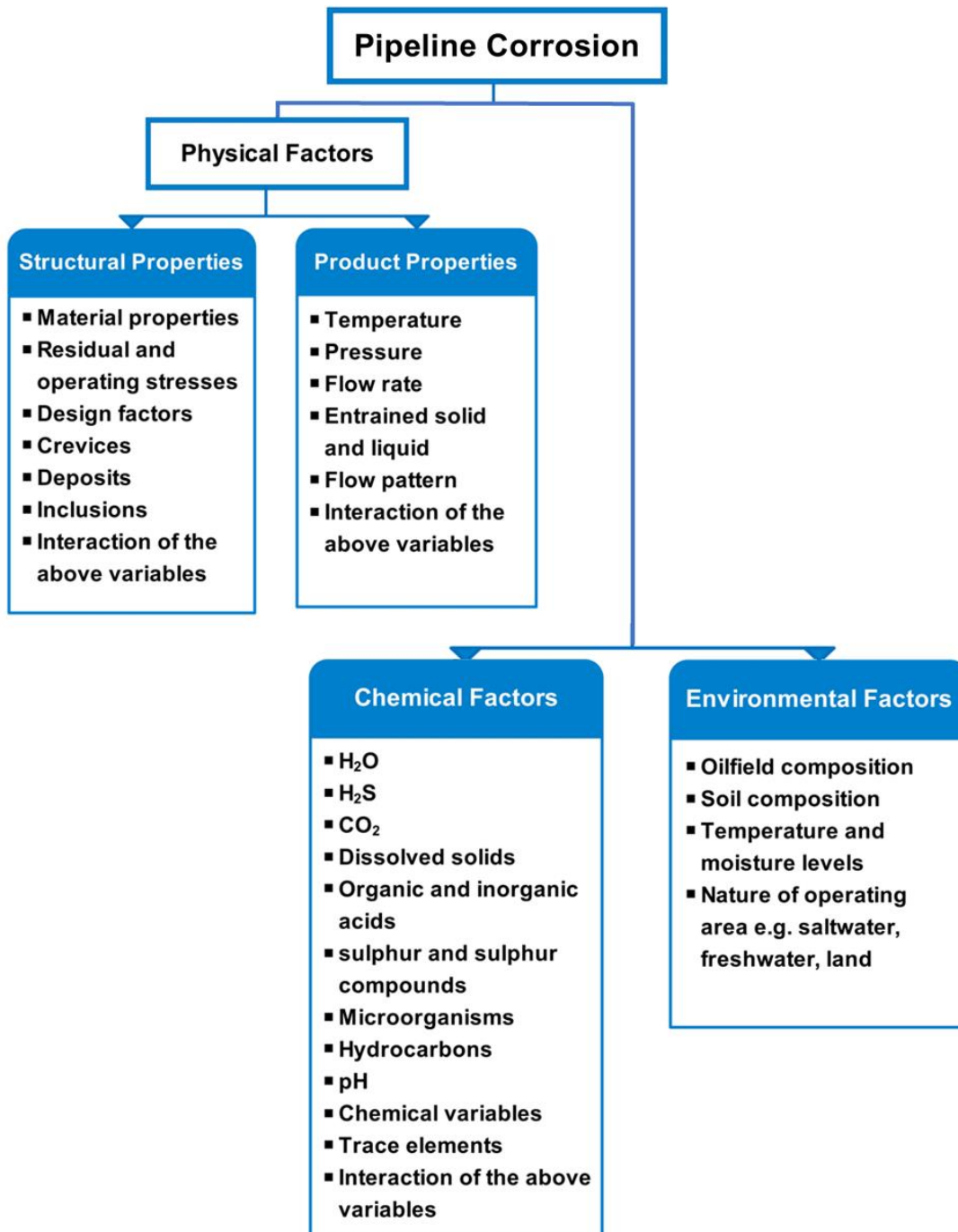
Figure 2.1 Causes of pipeline corrosion (Ossai et al. 2015)

- **Flow accelerated corrosion (FAC) and erosion-corrosion (EC)**

For clarity of discussion, it is important to distinguish the flow accelerated corrosion and erosion-corrosion. These two types of corrosion are quite distinct; however, it is not well distinguished by several authors in the literature. *Flow accelerated corrosion (FAC)* is defined as accelerated corrosion by the turbulent fluid flow over a surface, which promotes mass transfer and enhances the dissolution and thinning of protective films in carbon steel pipes protected by magnetite (Efird 2011a; Efird et al. 1993). In this study, the term FAC is used to indicate the flow assisted corrosion caused by a **single-phase** (only liquid phase) oilfield water (Zeng et al. 2020). However, *Erosion-corrosion (EC)* is the enhanced corrosion caused by the flowing fluid, which contains **two or more phases** with various combinations of gas, water, oil, and sand (Efird 2011a; Efird et al. 1993). In this study, the term EC is used to specify the corrosion caused by **two-phase** (oilfield water with sand particles) flow (Zeng et al. 2020). Figure 2.2 shows a pipe elbow that was degraded due to the effect of fluid flow in a desalination station (Muthanna et al. 2019).
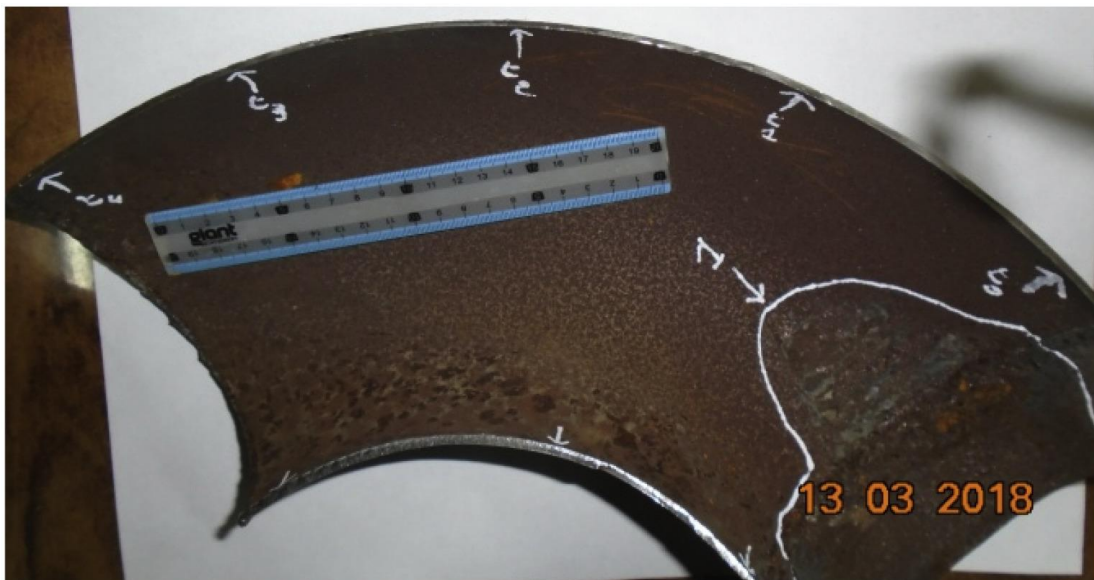
Figure 2.2 Pipe elbow degraded by corrosive fluid flow (Muthanna et al. 2019)

2.2 Fluid dynamics basics

Pipeline corrosion and failures occur due to the synergetic effect of electrochemical reactions and fluid flow. To understand the causes and their mechanisms involved in pipeline corrosion, electrochemistry and fluid dynamics fundamentals must be cleared. In case of corrosion, type of materials and electrolyte are governing the reactions, whereas on the fluid dynamics side, type of flow (such as steady, unsteady, laminar, turbulent, single-phase, and multiphase) must be considered (Schmitt and Bakalli 2009).

Steady and unsteady flow

In a steady flow, fluid properties do not change with respect to time at a specific point. However, fluid flow is mostly unsteady by nature (Murdock 2006).

Laminar and turbulent flow

Fluid flow through a pipe can be subdivided into laminar or turbulent. Reynolds number (R_e) is used to classify the flow based on its intensity. It can be calculated using equation 2.1 (Murdock 2006).

$$\textit{Reynolds number } (\boldsymbol{R_e}) = \frac{inertia\ forces}{viscous\ forces} = \frac{\rho V D}{\mu} \tag{2.1}$$

Reynolds number (R_e), significantly depends on the average fluid velocity (V), internal diameter or hydraulic diameter of the pipe (D), density (ρ), and dynamic viscosity (μ) of the fluid. Based upon the domination of inertia force or viscous force, flow through a pipe could be divided into three regimes,

- Laminar flow – $R_e < 2300$
- Transition flow – $R_e > 2300$ and $R_e < 4000$
- Turbulent flow – $R_e > 4000$.

Further, when the pipe diameter is the same, the flow regime appears different due to the variation in density, viscosity, and velocity (Murdock 2006).

A two-dimensional velocity profile of laminar flow through a pipe is illustrated in Figure 2.3(a). The laminar flow is smooth and easy to predict in which the fluid particles move in streamlines parallel to the centerline (₵) of the pipe with different velocities. The velocity profile distribution of the laminar flow would increase parabolically and velocity is maximum at the centerline of the pipe. A two-dimensional velocity profile of turbulent flow through a pipe is depicted in Figure 2.3(b). The fluid particles move randomly due to mixing phenomena and eddies (flow turbulence) within the flow. It is clear that fluid particles deviate from the streamline and move in irregular paths which results in an unsteady flow rate. The velocity is not uniform across the cross-section and it is maximum at the centerline of the pipe (Shalaby 2018a).

Maximum velocity

(a) *Laminar Flow*   **(b)** *Turbulent Flow*
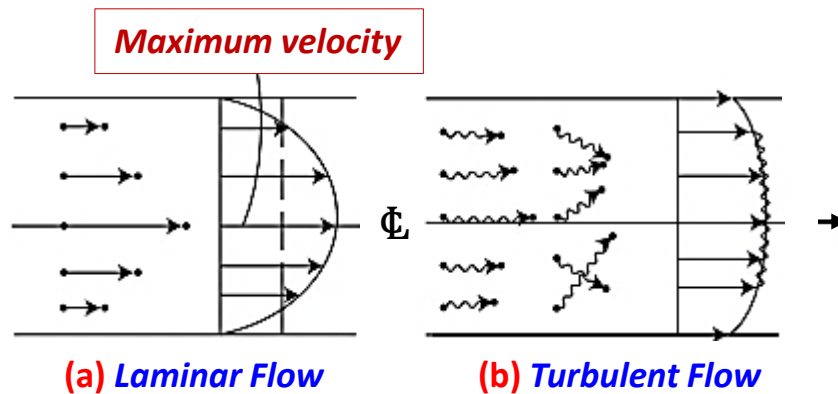
Figure 2.3 Two-dimensional velocity profiles of (a) laminar and (b) turbulent flow

Shear stress (τ) distribution in a pipe

Shear stress (τ) is defined as the tangential force per unit area that is applied by the fluid flow on the surface of the pipe. Figure 2.4(a and b) illustrates a velocity profile and shear stress distribution of a fluid flow. It is clear from Figure 2.4(b) the shear stress depends linearly from the centerline to the pipe wall ($0 < \tau_1 < \tau_2 < \tau_{max}$). However, maximum shear stress (τ_{max}) exerted by the flow is known as wall shear stress (τ_w) and is controlled by various factors such as turbulent intensity and flow velocity (Katritsis et al. 2007).

(a) *Velocity profile*   **(b)** *Shear stress (τ)*
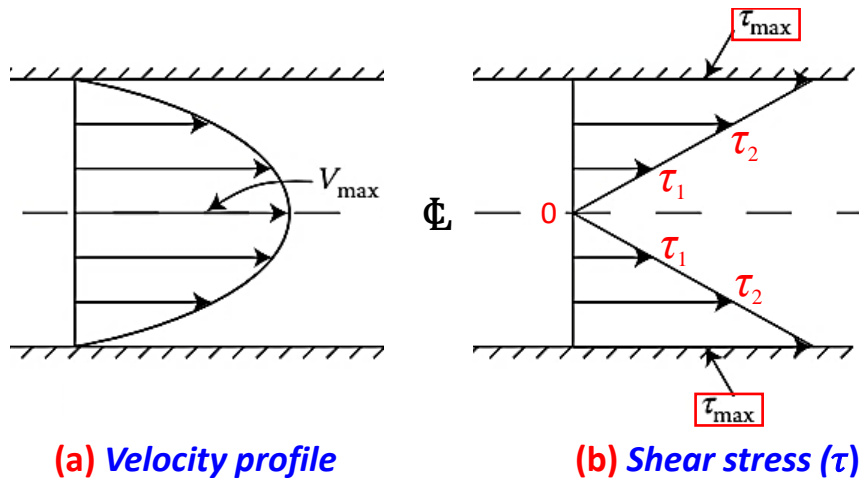
Figure 2.4 (a) Velocity profile, (b) Shear stress (τ) distribution of a fluid flow

Developing flow and developed flow

The velocity profile and shear stress of a fluid flow fluctuate with the length of the pipe until it attains a fully developed steady flow as illustrated in Figure 2.5. At the entrance of the pipe, flow is unsteady, where the velocity is not constant. After flowing through a particular length of pipe, the fluid flow will be in steady and developed condition until the direction of the flow changes. This developing length is called entrance length (L_e). For a turbulent fluid flow, the entrance length is 50 times the hydraulic diameter (D), whereas, for a laminar flow, it is a function of Reynolds number (R_e) and hydraulic diameter (D) (Shalaby 2018a). The boundary layer is a small layer between the bulk flow and solid wall where the effect of friction is significant, as shown in Figure 2.5. The fluid velocity in this near-wall region (viscous sublayer) is decreasing (non-uniform) due to the effect of viscosity and shear stress. The thickness of the boundary layer (laminar and turbulent) grows until it fully covers the inner diameter of the pipe (Schmitt and Bakalli 2009; Shalaby 2018b). The boundary layer disruption occurs by the vortices and turbulent bursts due to an aggressive turbulent flow which is seen in various oil-carrying pipelines (Efird 2011a).
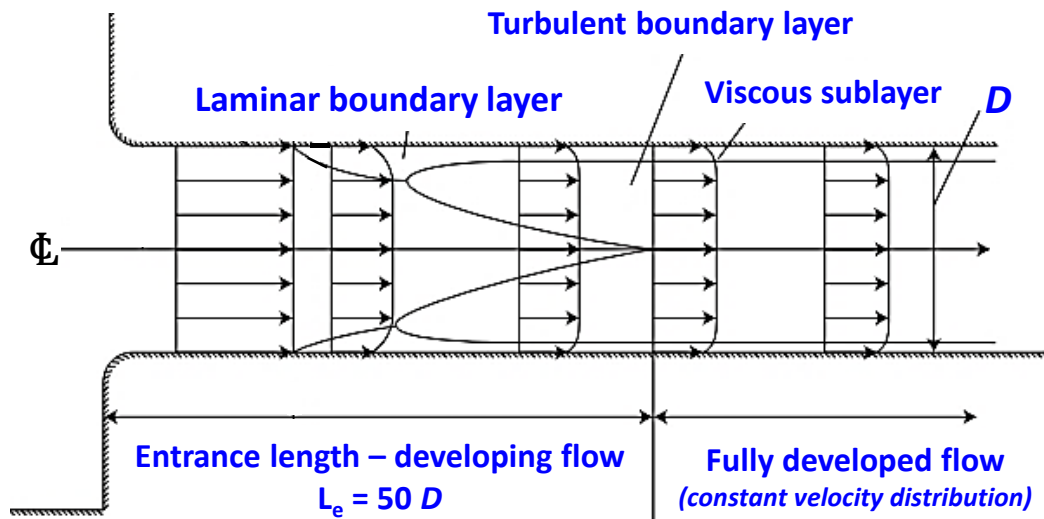
Figure 2.5 Illustration of developing and developed turbulent fluid flow

2.3 Effect of flow velocity on corrosion

The influence of flow velocity on corrosion rate is illustrated in Figure 2.6. Flow through a pipe is clearly divided into three regions based on the assumption that fluid velocity is increasing along the pipe from sections 1 to 3. It is also noticed that fluid velocity is directly proportional to the mass transfer rate (MTR) and inversely proportional to the thickness of the mass transfer boundary layer (δ_{MT}) (Palacios 2016).

Electrochemical corrosion and mass transfer process occur by diffusion, migration, and convection under flow condition and are major factors that influence corrosion. Concentration gradient due to a chemical change at the metal surface leads to diffusion, whereas potential gradients result in the migration of charged species. Forces exerted by the fluid flow enhance the movement of a species, thus convection (Wood 2007). A high flow velocity accelerates the corrosion rate by influencing anodic and cathodic reactions. Moreover, it also removes or dissolves the protective film and results in exposure of bare metal and sometimes significant localized corrosion. Precisely, corrosion can be controlled or mitigated by the alteration of cathodic and/or anodic reactions of the electrochemical cell (Jones 1996).
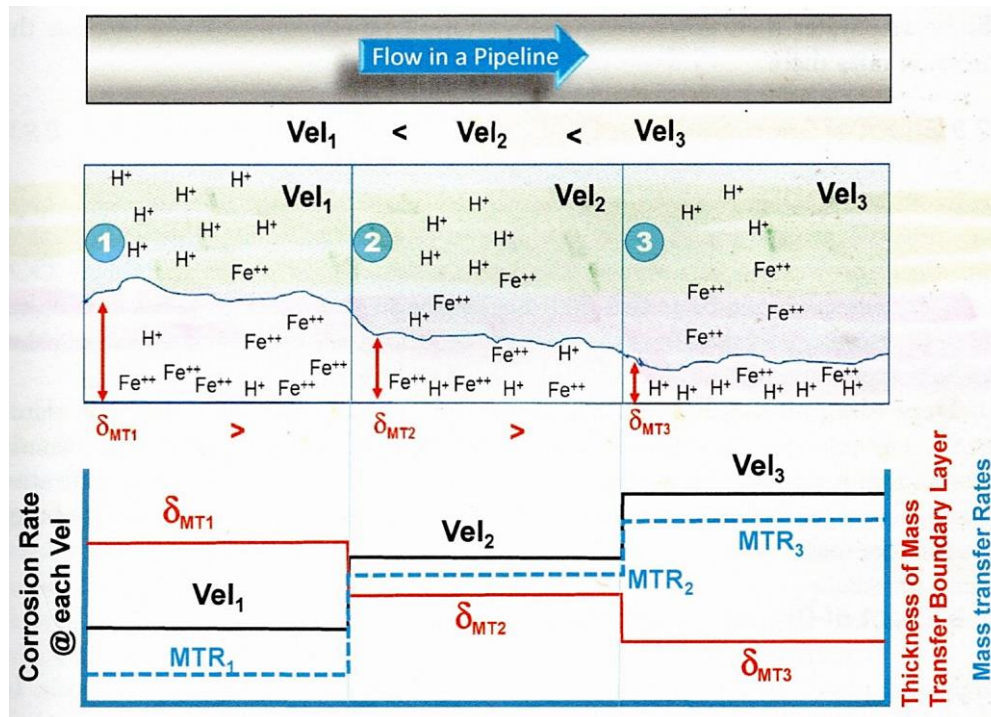
Figure 2.6 Influence of flow velocity on corrosion

2.4 Effect of flow regime or flow pattern on corrosion

It is well known that corrosion depends on the flow regime or flow pattern in the pipeline. A single-phase flow consists of only one phase either gas or liquid, while a multiphase flow indicates a simultaneous flow of more than one phase such as liquid-solid, liquid-gas, and gas-solid. The multiphase flow regime influences the turbulence of the fluid flow and increases the severity of degradation (Efird 2011a). Figure 2.7 depicts fluid–wall interactions for single and multiphase flow systems. The mechanical forces exerted by the hydrodynamics will rupture or remove the possible thin passive layer formed on the pipe wall and result in accelerated corrosion of the metal surface. It also includes mass transfer, heat transfer, fluctuating shear stresses parallel to the surface, fluctuating energy densities (fluctuating pressures) perpendicular to the surface, particle impact (erosion), and near-wall gas bubble collapse (Postlethwaite and Nesic 2011; Schmitt and Bakalli 2009).
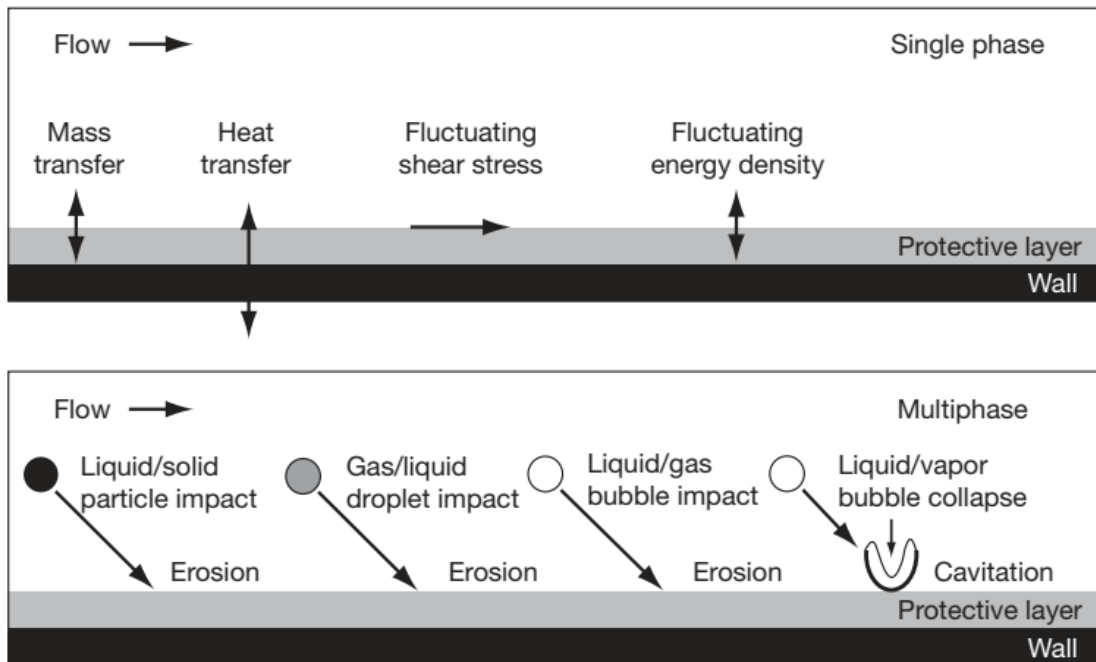
Figure 2.7 Fluid-wall interactions in single and multiphase flow (Heitz 1991; Schmitt and Bakalli 2009)

2.5   Effect of disturbed (unsteady) flow on corrosion

Disruption of a fully developed flow regime leads to a disturbed fluid flow. Fluid flow enhances corrosion and failure of components at the locations of disturbed or unsteady flow which mainly occurs due to the flow restricting or redirecting geometries such as weld beads, elbow, tee, and reducer. Among these pipe fittings, the 90º elbow is a vital and unavoidable element of any constructive piping system and they are susceptible to accelerated corrosion (Zeng et al. 2014; Zhang et al. 2013). The flow disturbance destroys the fully developed boundary layers and increases the corrosion rate at the component (Ahmed 2012; Efird 2011a). Hence, it is recommended for a pipeline designer to make the piping system more hydro-dynamically friendly. For example, it would be good to use a long radius elbow over a short radius to avoid sharp corners and reduce the effect of turbulence (Palacios 2016).

2.6   Effect of oilfield water chemistry

It is found that the oilfield solution, which consists of various complex compositions, is an aggressive environment to influence the piping system corrosion. Oil and gas production always encounters the presence of oilfield water or produced water along with hydrocarbon products. This oilfield water is rich in corrosive species such as chloride, sulfate, carbonate ions, dissolved gases, along with sand particles that responsible to promote flow accelerated corrosion (FAC) and erosion-corrosion (EC) or even an amalgamation of both (Popoola et al. 2013). The single or multiphase fluid flow enhances the removal of protective or semi-protective corrosion product film from the pipe wall by mechanical force, which will lead to the exposure of new steel surfaces to the aggressive corrosive fluid repeatedly - thereby increasing the ionic exchange or mass transfer rate leading to pipe wall thinning (Zeng et al. 2014).

The presence of sand particles in the flowing water enhances the erosion-corrosion of the pipeline materials (Ossai et al. 2015; Zhao et al. 2016). This problem is severe under turbulent flow conditions determined by the prevailing flow velocity and wall shear stress (Muhammadu et al. 2013; Zeng et al. 2014), which is becoming the main reason for the unplanned and frequent shutdown of the production facilities and sometimes even causing catastrophic pipeline failures or fatalities (Popoola et al. 2013). It is predicted that the probability of increasing this EC problem in the oil gas industry is more due to the aging of producing wells entail higher water cut and sand production (Zhao et al. 2016). Indeed, the synergetic effect of electrochemical reactions and hydrodynamics is a serious threat to the pipeline integrity and sustainability of the petrochemical industry.

2.7   Steel for pipelines

Carbon steels and alloy steels are generally used for oil and gas applications such as crude pipelines, flow lines, water, and steam injection lines, production and test separators, and storage tanks due to low cost, good mechanical properties, and fabricability (Popoola et al. 2013). High Strength Low Alloy (HSLA) steel is low-carbon steel ($< 0.3\%$ C) containing small amounts of alloying elements to get excellent mechanical properties and weldability (Ju et al. 2002; Kostic 1996; Sant'anna et al.

2002). These steels (HSLA) are designed and classified by American Petroleum Institute (API), USA, in the order of their yield strength (X42, X46, X52, X56, X60, X65, X70, X80, X100, and X120) and they can withstand high operating pressure at reduced wall thickness (Shukla et al. 2016; Zhao et al. 2019). These low-carbon steels are quite susceptible to corrosion due to the influence of highly corrosive fluid flow and increase in operational expenditure (Li et al. 2019; Shabarchin and Tesfamariam 2016; Yaro et al. 2015; Zeng et al. 2016b).

To minimize this issue there could be a possibility to use corrosion-resistant alloys (CRAs) that give more protection against corrosion. Although, CRAs protect the pipeline material by forming a passive layer due to the presence of high quantity chromium content and other alloying elements such as Cu, Ni, Mo, W, Ti, etc. But these alloys also failed due to the presence of high quantity chloride content coupled with the presence of erodent sand particles in the solution. Additionally, huge capital expenditure would be required for their use in pipeline networks (Palacios 2016). Hence, during the design stage, it is very important to decide whether to use CRAs with high cost or to select carbon steel (Papavinasam 2014b).

API steels are manufactured through the thermomechanical processing (TMP) method. Cautious selection of microalloying elements and optimization of TMP parameters play a vital role in the production of these steels with desired properties (Shukla et al. 2013). The major constituents of API steels are carbon (0.05–0.25%), manganese (maximum 2%), and a minor quantity of chromium, nickel, molybdenum, copper, nitrogen, vanadium, niobium, titanium, and zirconium (Takahashi and Iino 1996). Microstructure and manufacturing process details of API steels are illustrated in Figure 2.8. Various ranges of alloying elements and yield strength of commonly used API steels are depicted in Table 2.1 (API 5L 2018; Deardo 2003; Villalobos et al. 2018).
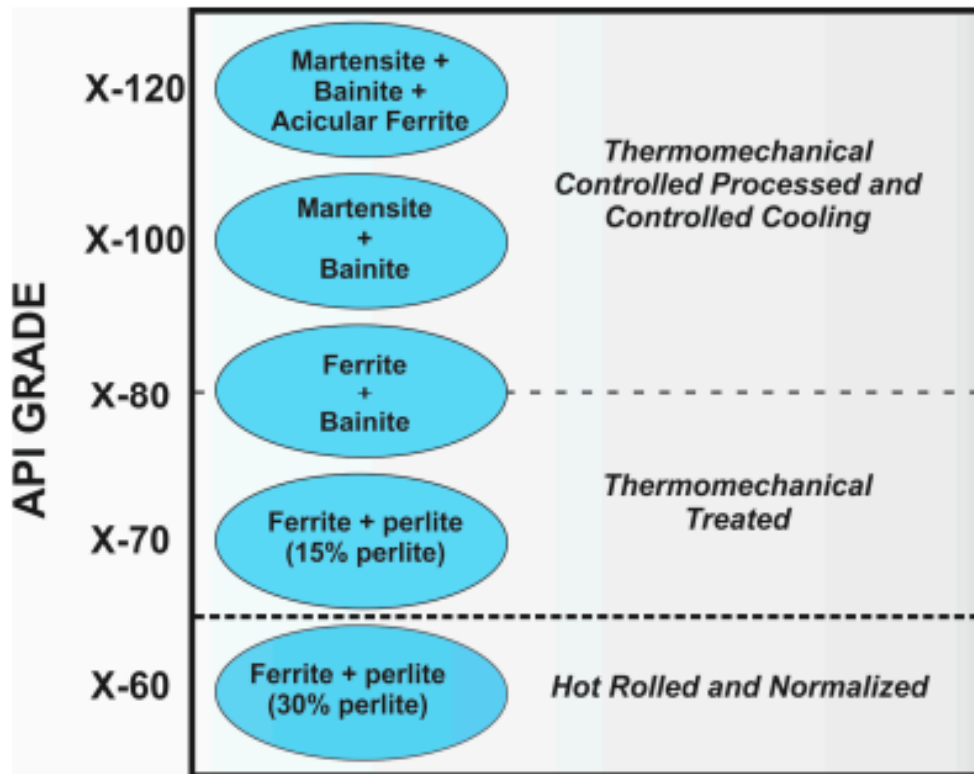
Figure 2.8 Microstructure and manufacturing process of API 5L grade steels

Table 2.1 Chemical composition and Yield Strength of API 5L steels (from API 5L Specification, 46th Edition, 2018)

Pipe Grade	C	Mn	Cr	Mo	Ti	Cu	V	S	Nb	Ni	Si	Yield Strength (psi)	Tensile Strength (psi)
X65	0.041-0.17	0.30-1.68	0.02-0.157	0.005-0.14	0.002-0.01	0.02-0.31	0.042-0.21	0.0002-0.03	0.018-0.06	0.005-0.8	0.02-1.39	65300-87000	77600-110200
X70	0.037-0.125	1.44-1.76	0.007-0.266	0.01-0.3	0.009-0.03	0.006-0.27	0.001-0.095	0.001-0.015	0.051-0.092	0.02-0.23	0.14-0.44	70300-92100	82700-110200
X80	0.028-0.142	1.52-1.90	0.015-0.12	0.05-0.3	0.007-0.024	0.015-0.20	0.002-0.1	0.001-0.009	0.038-0.09	0.02-0.75	0.17-0.31	80500-102300	90600-119700
X100	0.025-0.1	1.56-2.0	0.016-0.42	0.19-0.43	0.011-0.02	0.25-0.46	0.003-0.07	0.001-0.0024	0.043-0.089	0.13-0.54	0.1-0.25	100100-121800	110200-143600
X120	0.027-0.05	0.54-2.14	0.22-0.42	0.001-0.40	<0.015	0.010-0.015	<0.025	0.001-0.004	0.048-0.1	0.017-1.35	0.08-0.31	120400-152300	132700-166100

N.B.: *All the values are represented as **minimum-maximum***

2.8 Influence of fluid flow on corrosion of steels

Corrosion under flow conditions is a complex phenomenon that changes based on both the chemistry and physics of the system. Flow corrosion depends on both the electrochemical corrosion reactions and fluid flow. Fluid turbulence is the primary factor governing flow corrosion (Efird 2011b). Flow accelerated corrosion (FAC) and erosion-corrosion (EC) of different grade steels have been studied in different environments by several researchers in the past decades. Important remarks made by some of the researchers are discussed in this section.

Zhang and Cheng (2009) investigated the electrochemical corrosion behavior of API X65 steel in oilfield water and also observed it under influence of acetic acid. They have been found dominated by the anodic process without any active-passive dissolution in static condition tests. As corrosion proceeds, the surface of the steel sample was covered with iron carbonate film and acetic acid reduces the protective nature of scale (Zhang and Cheng 2009). The authors also characterized the flow corrosion of X65 steel in oilfield water using an impingement jet system. It is found that fluid hydrodynamics played a key role in steel degradation. Early corrosion products which provide short-time protection are removed by the fluid velocity and shear stress and thereby an accelerated mass transfer and corrosion occurred on the steel (Zhang and Cheng 2010). Similarly, another study is carried out under the static condition to know the corrosion behavior of X65 steel in an oilfield solution. The study revealed that a galvanic effect existed between the bare steel (acted as an anode) and the scale-covered region (acted as a cathode) and localized corrosion was accelerated significantly. It is clearly found that with increased time and temperature a stable iron carbonate scale was formed on the steel surface (Zhang and Cheng 2011).

Zhang et al. (2013) describe the effect of FAC on X65 pipeline steel with the help of a loop system. Simulated oilfield water was circulated through a loop system with a flow velocity of 3.4 m s^{-1}. This study revealed that the corrosion rates of various electrodes were varying with respect to the location of the electrodes in the pipe elbow. The author reported good agreement with his experimental data with computational fluid dynamic (CFD) simulation results (Zhang et al. 2013). Ilman et al. (2014) presented a case study of a failed API 5L X52 subsea oil pipeline that was prone to leak

after 27 years of service. After a detailed investigation, it was concluded that the synergetic effect of electrochemical corrosion and mechanical forces (flow velocity and shear stress) was the major reason for the failure (Ilman and Kusmono 2014).

Rosa Vera et al. (2015) analyzed the corrosion behavior of X65 steel and ASTM 53-B steel in seawater under static and dynamic conditions. They revealed that the X65 steel exhibits better corrosion resistance in seawater. The corrosion rates under flow condition for X65 and ASTM 53-B steels were 0.41 µm/year and 0.59 µm/year respectively after 10 days (Vera et al. 2015). Tobón et al. (2015) compared the effect of flow corrosion on two different compositions of X70 steel [traditional (T) and new generation (NG)] in a brine solution using the rotating-cylinder electrode (RCE) technique. The synthetic brine solution containing hydrogen sulfide and kerosene was prepared according to NACE standard 1D-196. Flow rates of the electrolyte (with temperature 60°C) were selected in the range of 1-4 m s^{-1}. The observed variations in corrosion rate for flow rate are depicted in Figure 2.9. It reveals that the corrosion rate is increasing with the flow rate. The X70-NG steel with more copper content and increased ferrite phase exhibited better corrosion resistance due to more stable and protective oxide film formation on the sample surface. The presence of the copper element reduced the cathodic reaction (Cervantes Tobón et al. 2015). The reduction in corrosion rate benefited from the delayed anodic reaction or ferrite dissolution due to the availability of nickel and chromium elements in the particular X70 steel (Cervantes Tobón et al. 2015).
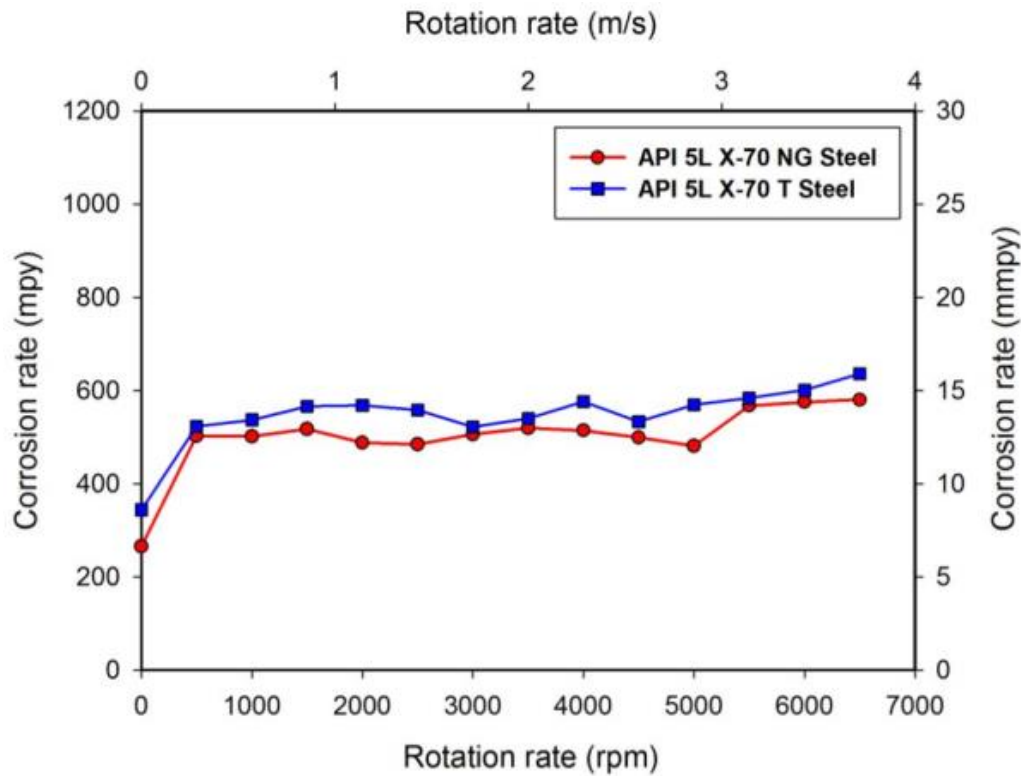
Figure 2.9 Corrosion rate as a function of flow rate for X70-T and X70-NG samples

Huang et al. (2016) studied the corrosion behavior of X52 steel at a pipe elbow with the help of a flow loop apparatus and CFD simulation. It was found that the corrosion behavior in the simulated cooling water of high salinity is in accordance with the fluid flow properties. The corrosion rate was maximum at the outer wall side of the pipe elbow (Huang et al. 2016). Jiang et al. (2017) examined the effect of chromium on flow corrosion behavior of low alloy steels (carbon steel composition and Cr-containing steels) in a 3.5% NaCl solution. The weight loss and electrochemical methods were adopted for this investigation. Tests were conducted with the help of a loop system and rotating-cylinder electrode (RCE) at different flow rates. Cr-containing steels exhibited superior corrosion resistance than carbon steel due to the presence of chromium content that resulted in the formation of a protective passive layer on the metal surface and inhibition of cathodic reaction of low alloy steels under flow conditions (Jiang et al. 2017).

Si et al. (2009) investigated the effect of turbulent flow (velocity) on the corrosion behavior of low carbon steel (ASTM A106 Gr. B). Electrochemical corrosion

tests were conducted by placing steel samples at the 90° elbow test section. An alkaline aqueous solution with 25° C temperature and atmospheric pressure was circulated with a flow velocity of 1.5 m s^{-1} through a loop system. Corrosion rate values were maximum at the outer wall side of the elbow, while the minimum at the inner wall side. Comparison of the experimental (corrosion) and CFD simulation results reveal that the flow velocity accelerates the electrochemical corrosion and pipe wall thinning (Si et al. 2019). A similar study performed by the authors, using circulating distilled water with a flow velocity of 3 and 1.5 m s^{-1}, also confirmed the FAC rate and mass transfer of A106 Gr. B steel are maximum at the extrados (outer wall) of the elbow (Si et al. 2020). Recently, a study was conducted by Li et al. (2021), to know the flow corrosion characteristics of X100 line pipe steel in simulated oilfield water with an in-house design flow apparatus using an electrochemical corrosion test. The results were compared with the computational fluid dynamics (CFD) simulation. As the velocity increases from 0.5 to 2.0 m s^{-1} corrosion current and corrosion rate of X100 steel increased. The corrosion rate was more at the sample kept at a minimum impact angle of 30°, due to the highest flow velocity and shear stress (LI et al. 2021).

2.9 Corrosion mitigation methods in the oil and gas industry

It is important to select suitable mitigation methods for corrosion of pipelines economically to improve the age of pipes. There are several proven techniques that are widely used to control and minimize the corrosion of oil and gas pipelines (Palacios 2016; Papavinasam 2014b).

- ❖ Chemical Treatment (Biocides, Surfactants, etc.)
- ❖ Inhibitors (Anodic, Cathodic, and Mixed type)
- ❖ Internal lining, coating, and cladding
- ❖ Corrosion Allowance (extra thickness on material)
- ❖ Removal of corrosive species
- ❖ Pipeline Scraping or Equipment Cleaning
- ❖ Cathodic Protection

2.10 Corrosion inhibitors for steel pipelines

A corrosion inhibitor is a chemical substance or combination of substances that, when present in the proper concentration and forms in the environment, reduces the corrosion rate (NACE/ASTM 2012). Corrosion control using inhibitors is a proven practice in various industries including petrochemical industries (Durnie et al. 1999; Jovancicevic 1999; Okafor et al. 2009). Inhibitors can control the corrosion by altering anodic and/or cathodic reactions without changing the fundamental processes (Raja and Sethuraman 2008).

Classification of various types of inhibitors is given in Figure 2.10 (Ahmad 2006). Ecological and health risks of inhibitors are a global concern. Most of the inorganic inhibitors which are good in material protection are not environment-friendly. There is a possibility of a harmful effect on the human organ system during the synthesis or application of these toxic inhibitors (Raja and Sethuraman 2008). Inorganic inhibitors are either anodic or cathodic, whereas organic inhibitors are anodic-cathodic mixed types.
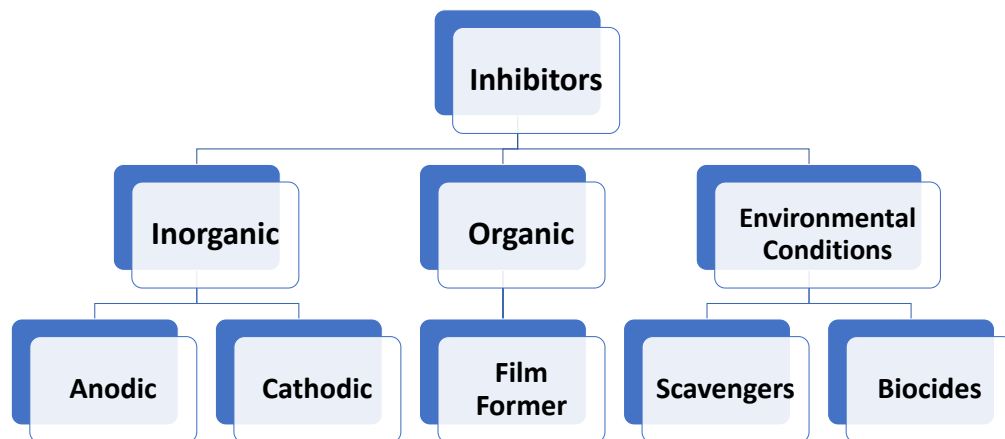
Figure 2.10 Classification of inhibitors

The organic inhibitor molecules (a combination of polar head group and hydrocarbon chain) generally form a protective barrier at the metal-electrolyte interface as shown in Figure 2.11 (L. Riggs Jr 1973). The polar headgroup adsorbs on the metal surface by chemical and physical adsorption process. Corrosive species such as oxygen and hydrogen sulfide can be removed by scavengers. Biocides control the bacteria population and thus microbiologically influenced corrosion (MIC). Nitrogen-based organic compounds such as fatty acid salts, amines, imidazolines, hydrazides, and amides can be effectively used to mitigate corrosion in the oil and gas industry (Heydari and Javidi 2012; Palacios 2016).
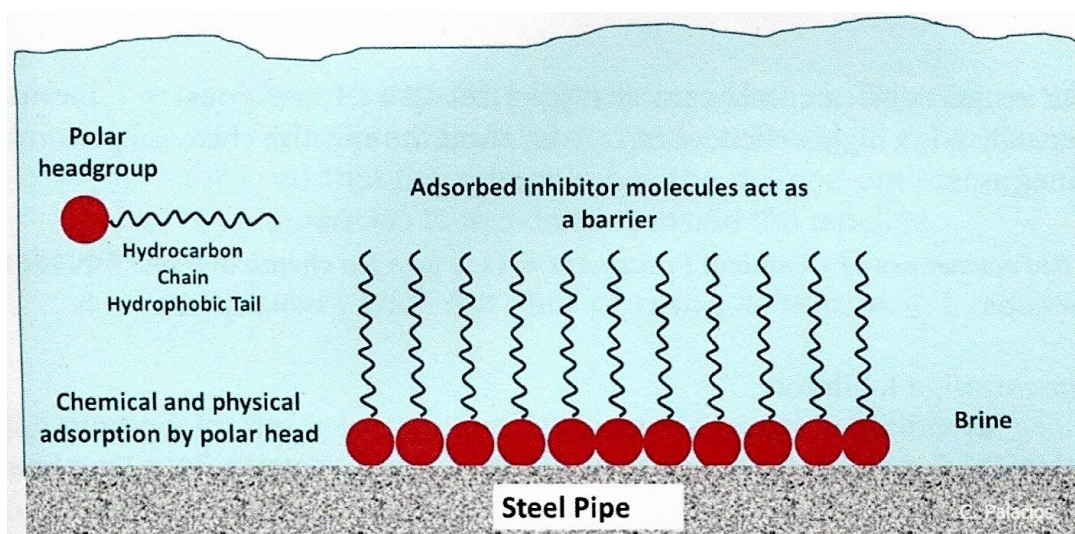
Figure 2.11 Illustration of inhibitor molecule adsorption

Many researchers studied the performance and protective behavior of several corrosion inhibitors under oil and gas industry environments. Some of the important outcomes of those studies are discussed in this section.

Zeng et al. (2015) investigated the influence of thioureidoimidazoline inhibitor (TAI) containing nitrogen and sulfur atoms on FAC of a pipe elbow in oilfield water using a loop system. Corrosion tests were performed by placing X65 steel samples at different locations of the elbow with a flow velocity of 4 m s^{-1}. It is found that TAI is an anodic type inhibitor and its inhibition efficiency was varying in accordance with the hydrodynamic parameters such as flow velocity, shear stress, and turbulent kinetic energy. They have noticed that using 1 mg/L, 10 mg/L, 50 mg/L, and 200 mg/L, only 100 mg/L is exhibited the best protective behavior over other concentrations (Zeng et al. 2015). Further, they studied the effect of TAI for X65 line pipe steel under static and flow conditions using a loop system. FAC tests were conducted at two different flow velocities such as 2 and 4 m s^{-1} of formation water containing TAI of 100 ppm concentration. Electrochemical corrosion analysis stated that the efficiency of thioureidoimidazoline inhibitor under flow condition is lower over static condition due to the influence of hydrodynamics. The inhibition efficiencies at static condition, 2 and 4 m s^{-1} velocities are 95.8%, 63%, and 59.1% respectively (Zeng et al. 2016b). Zeng et al. presented another work on the influence of TAI on flow corrosion of X65. It is noticed from electrochemical impedance spectroscopy (EIS) results shown in Figure 2.12, that the charge transfer resistance and inhibition efficiencies vary with respect to the position of steel sample at pipe elbow. Computational fluid dynamics (CFD) simulation results demonstrated that turbulence and shear stress of fluid flow restricts the adsorption of inhibitor and removes the adsorbed film from the steel surface (Zeng et al. 2017).
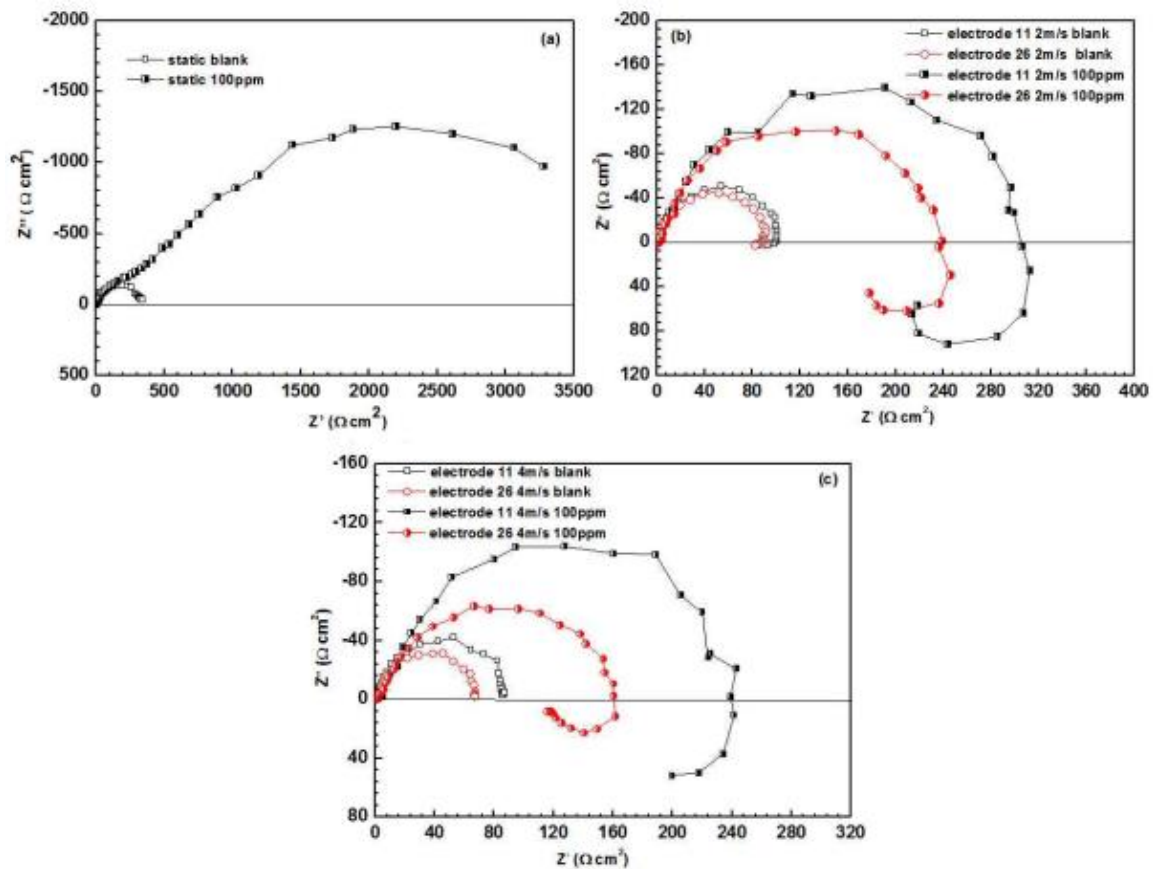
Figure 2.12 Nyquist plots: (a)static, (b) 2 m s⁻¹, and (c) 4 m s⁻¹

Zhong et al. (2020) investigated the localized corrosion behavior of N80 steel and its mitigation under flow condition using a loop system. The samples were placed at a gradual contraction (reduced diameter) location of a straight pipe and tested using a circulating oilfield (formation) water with velocities of 2 and 4 m s⁻¹. CFD simulation was also performed to understand the synergetic effect of corrosion and hydrodynamics. FAC mitigation study was performed by utilizing a 100 ppm concentration imidazoline derivative inhibitor which contains imidazoline rings that hold Nitrogen content and carbon (C-11) saturated hydrophobic groups. Comparative analysis of CFD simulation and electrochemical impedance spectroscopy results demonstrate that corrosion rate distribution of steel samples is in accordance with flow velocity and wall shear stress. Imidazoline derivative inhibitor reduced the corrosion by reducing the mass transfer and charge transfer processes particularly at low velocity (Zhong et al. 2020).

Lopes-Sesenes et al. (2013) studied the influence of fluid flow on corrosion mitigation of AISI 1018 carbon steel in 0.5 M sulfuric acid solution. Extract of Buddleia Perfoliata leaves (100 ppm) was used as the natural green inhibitor using the rotating disk electrode (RDE) technique at speeds of 0, 250, 500, 1000, and 2000 rpm. Electrochemical corrosion analysis results have revealed that corrosion rate was highest at the rotation speed of 500 rpm without using an inhibitor. But, in the presence of green inhibitor, the corrosion rate was increased with an increase in the rotation speed due to the detachment of inhibitor molecules from the metal surface. It further led to form an active site and resulted in rapid degradation of the metal surface (Lopes-Sesenes et al. 2013). Barker et al. (2013) investigated the performance of commercially available nitrogen and carboxylic acid-containing corrosion inhibitor on carbon steel under flow condition. Experiments were conducted using a submerged impinging jet system at a flow velocity of 7 m s^{-1}. It is noticed that the inhibition efficiency under flow conditions are lower than static condition (Barker et al. 2013).

Quraishi et al. studied the inhibition efficiency of long-chain fatty acid derivatives, in particular, OAH inhibitor, in the static condition. The oleic acid hydrazide (OAH), an organic compound is found as a promising environmentally-friendly, green inhibitor which can be used to protect alloy steels against corrosion with high efficiency, low cost, easily obtainable, and ease of synthesis (Quaraishi et al. 2000; Quraishi and Ansari 2003).

2.11 Surface engineering for corrosion and erosion resistance of steels

Surface engineering techniques are mostly employed to improve the performance and lifespan of materials. It is basically a treatment of the surface and near-surface regions of a material to allow the surface to perform functions that are distinct from those functions demanded from the bulk of the material (Cotell and Sprague 1994). There are a number of applications to increase resistance against corrosion, oxidation, wear, mechanical properties, electronic or electrical properties, thermal insulation, and aesthetic appearance. Properties of the surface can be modified by the improvement in surface metallurgy of the metal by shot peening, laser melting, flame hardening, electron-beam hardening, laser hardening, or induction hardening. Surface chemistry alteration methods such as nitriding, carburizing, laser alloying, anodizing, boronizing, and steam treating are also employed to improve the serviceability of the material. Adding a surface layer or coating to a metal surface is also a proven method to improve the functionality of materials. It includes galvanizing, aluminizing, electroplating, thermal spraying, cladding, and organic coatings, etc. (Davis 2001). Among these surface engineering methods, laser surface melting (LSM) is a promising and cost-effective technique, which can be used to improve the surface performance of materials through grain refinement and the development of fine distributions of precipitates in solid solutions (Davis 2001; Kusinski et al. 2012).

2.12 Effect of laser surface melting (LSM) to improve the resistance against FAC and EC

Laser surface melting (LSM) is an advanced technique, using a laser as a high energy density heat source without vacuum, as it can be transmitted through the air (Kwok et al. 2007). Figure 2.13 shows an illustration of the LSM process. Locations of the piping system, which are severely affected by localized corrosion or erosion-corrosion, such as elbows, tees, reducers, and weld joints can be successfully treated locally utilizing a laser integrated with a robot/CNC workstation, wherever required, with precision (Hu et al. 2011). Additionally, the LSM process involves low or negligible distortion on the treated parts (Shi 2013; Zhao et al. 2016). Thus to enhance the service life of these parts by imparting improved resistance to erosion, corrosion, and mechanical properties of the steels (Kwok et al. 2007; Shariff et al. 2010). LSM modifies the surface without

affecting the bulk chemical composition of the steel at a low cost (Zhao et al. 2016). LSM involves rapid heating and cooling due to the localized process with unaffected lower bulk material acting as a heat sink without changing the core's microstructure. Since, LSM is known as a "self-quenching" process, it needs no separate quenching medium (Li et al. 2011; Vora and Dahotre 2013). Often, a fine metastable phase results in the treated layer with a non-equilibrium microstructure with higher hardness (Iordanova et al. 2002). The modified microstructure of the steel determines the corrosion resistance, especially when appropriate alloying species are involved. However, during the rapid cooling process, melted steels promote the transformation of austenite into martensite, a diffusionless transformation (Vilar 2012).
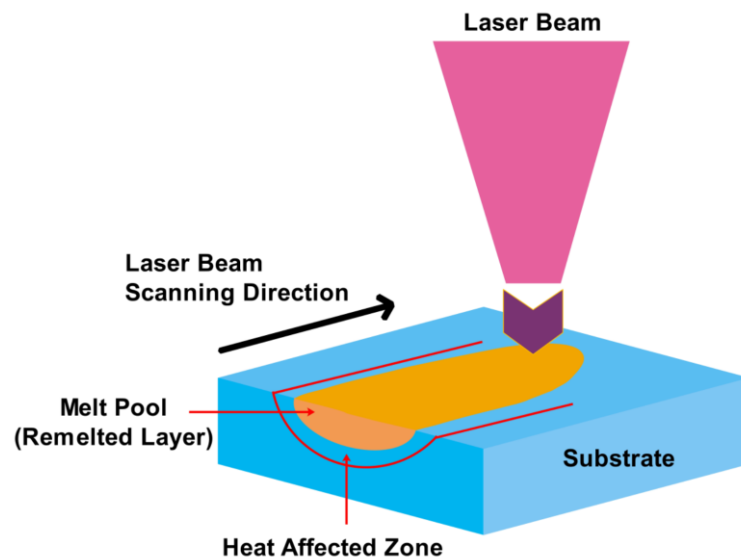
Figure 2.13 Schematic of laser surface melting (LSM) process

Many researchers are looking to improve corrosion, and erosion-corrosion resistance of ferrous alloys by LSM process which results in grain refinement, increase of the alloying elements content in solid solution, surface hardening, and surface strengthening (Davis 2001; Krastev 2012). Some key findings of those investigations are discussed in this section.

Zhao et al. (2016) studied the effect of LSM on erosion-corrosion of X65 line pipe steel under slurry flow with a velocity and temperature of 20 m s^{-1} and 50 °C respectively. In this study, a carbon dioxide laser with laser power of 1.3 kW, and scanning speed 2000 mm min^{-1} was utilized for the LSM process. Circular samples with

25 mm diameter and 6 mm thickness were prepared from laser melted X65 steel plates. The total thickness of the melted layer was 800 μm. The erosion-corrosion study was carried out in a synthetic brine solution containing sand particles (1000 ppm) with a jet impingement apparatus. Erosion-corrosion rates varied concerning the impact angles and reduced by the laser surface melting. Change in microstructure from ferrite to lath martensite, and enhancement in surface hardness reduces the corrosion rate and erosion-corrosion rate in slurry jet flow conditions (Zhao et al. 2016).

In general, the martensitic transformation in steels occurs due to a very high quenching rate, which will provide insufficient time for carbon diffusion. This diffusionless transformation leads to the transformation of face-centered cubic (fcc) austenite to body-centered tetragonal (bct) martensite, which has a unit cell different from body-centered cubic (bcc: a = b = c) ferrite (which forms during the slow cooling). The martensitic structure shows high hardness due to its distorted lattice structure in which two edges are equal, and the third one is elongated (bct: a = b ≠ c), due to the presence of interstitial carbon atoms. Hence, it is also called the solid solution of iron and carbon (Avner 1997; Callister Jr. and Rethwisch 2014; Luo et al. 2010; Vilar 2012; Vora and Dahotre 2013).

However, the lattice parameters of martensite in steels vary with carbon content in a nearly linear fashion. The tetragonality (c/a ratio or axial ratio) and the volume of the unit cell increase with the carbon content based on the following equation 4.18 (Nishiyama 1978).

$$c/a = 1 + 0.045 \text{ wt.\% C}. \hspace{3cm} (4.18)$$

It is clear from equation 4.18 that, when the carbon content is very low (< 0.25 wt.%), the structure of martensite would be cubic and it is mainly due to the axial ratio is so close to unity that the tetragonality cannot be detected as well as if the martensite can be cubic as long as the carbon content is very small (Nishiyama 1978; Sauvage et al. 2003; Zhang et al. 2016). To use the term 'martensite', the existence of carbon-producing tetragonality is not an important requirement. The martensitic transformation can be defined as a phase transformation, occurs by a cooperative atomic movement that directly affects the crystal structure and tends to change. A given martensitic

structure produced by cooperative atomic movements can be confirmed by the existence of various characteristics such as lattice imperfections (example: dislocations). In low carbon steels, the martensite crystals are lath-shaped, and dislocations can be seen in the crystals (Nishiyama 1978).

Sivanandham et al. (2013) analyzed the microstructural and corrosion properties of laser surface melted Grade 420F stainless steel and EN32B low carbon steel. The laser surface treatments were performed using laser powers of 2, 2.5, and 3 kW with maintaining scan rate of 12 and 20 mm s^{-1}. The SEM analysis revealed that the microstructures of the steels were altered due to fast heating and cooling rates associated with the LSM process. It was noticed in Grade 420F SS, martensite with retained austenite formed. Whereas full lath martensite is developed in EN32B steel. An electrochemical corrosion study indicates that the LSM process increased the resistance against corrosion for both the steels in corrosive solution (Sivanandham et al. 2013). A study that describes the influence of LSM on surface properties of EN353 steel is carried out by Sivanandham et al. (2017). The LSM treatment is done using laser powers of 2, 2.5, and 3 kW and a scan rate of 12 mm s^{-1}. An interesting microstructure containing ferrite and pearlite transformed to martensite by the LSM process of low carbon alloy steel. The XRD patterns of LSM and untreated steels are given in Figure 2.14(a-d). It indicates the existence of the ferrite phase in the untreated steel. The LSM process resulted in the formation of Fe-C and martensite, along with Fe-Cr-C and Fe-Mn-C. The effect of modification of the surface directly influenced the hardness and increased wear and corrosion resistance (Sivanandham et al. 2017).
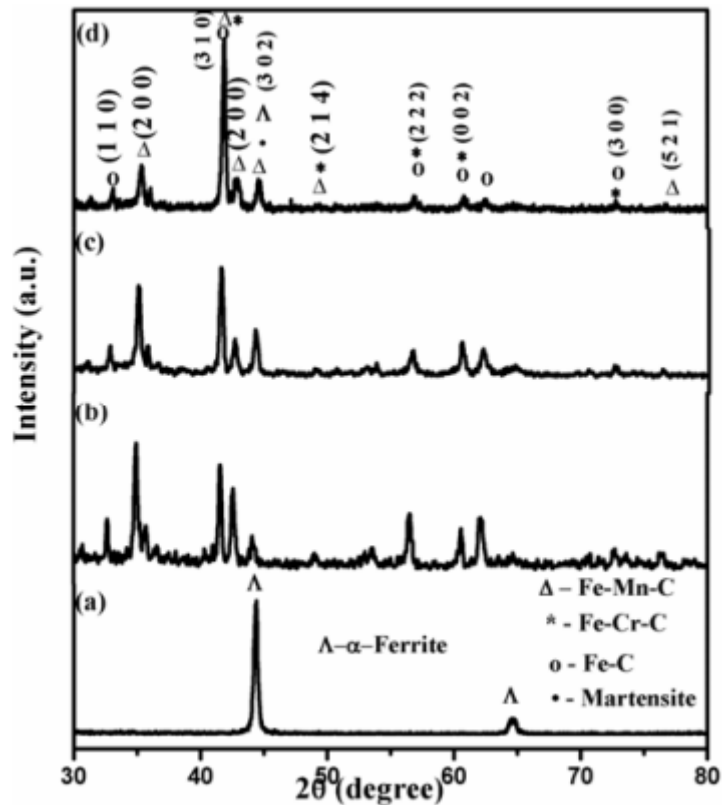
Figure 2.14 XRD pattern of EN353 steel, (a) untreated, laser treated at (b) 2.0 kW (c) 2.5 kW and (d) 3.0 kW

Kwok et al. (2007) investigated the effect of LSM (at 2.5 kW) on corrosion properties of high-speed steels (HSSs) by potentiodynamic polarization technique. Surfaces of HSSs were melted by an Nd: YAG (Neodymium: Yttrium-Aluminum-Garnet) laser with a power of 2.5 kW. Microstructural analysis revealed fine-grained martensite with little retained austenite after the LSM process. It is also observed, LSM process benefited in improved microhardness. A noble shift in the corrosion potential and a reduction in the corrosion current density proved that the LSM process is quite superior in spontaneous passivation and beneficial in the improvement of corrosion resistance in 0.6 M NaCl and 0.5 M NaHCO$_3$ solutions at 25 °C. They concluded that the microstructural alteration with disconnection and refinement of large carbides and the rise in passivating alloying elements such as Cr, Mo, and W in solid solution resulted in improved corrosion resistance of high-speed steels (Kwok et al. 2007).

Majumdar and Manna studied the effect of laser surface alloying (LSA) of Grade 304 stainless steel to examine the localized corrosion (pitting) and erosion-

31

corrosion resistance. LSA was performed after the deposition of Mo on the substrate by the plasma spray method. The LSA process resulted in enhancement of microhardness values and alteration of the microstructure of the surface. Corrosion and erosion-corrosion resistances of surface modified stainless steel were improved as compared to without treatment in 20 wt.% sand in corrosive 3.5 wt.% NaCl solution (Majumdar and Manna 1999). Basha et al. (2013) studied the surface properties of 16Cr-5Ni martensite stainless steel by laser surface alloying (LSA) and laser transformation hardening (LTH). The slurry erosion resistance of 16Cr-5Ni steel was improved by LSA and LTH. Commercially available Co-based Wallex-50 and Ni-based Tribaloy-700 powders were used for laser surface alloying. They have conducted slurry jet erosion tests with silica sand particles (average size 200 μm) and maintained flow velocities of 10 and 12 m s^{-1}. Improved hardness and altered microstructures are important factors for the enhancement of slurry erosion wear resistance by about 3 times as compared to untreated samples (Basha et al. 2013).

Carboni et al. studied the effect of LSM using 1 kW on Grade 316L stainless steel in 0.05 M NaCl solution. Microstructural and phase analyses of melted layers with a thickness of 400 μm were examined. The pitting corrosion resistance was significantly improved due to the development of fine-grained and homogenized microstructure. It is also found that the elimination of unfavorable inclusions also benefited in the enhancement of corrosion resistance (Carboni et al. 2002).

Elemuren et al. studied the slurry erosion-corrosion behavior of AISI 1018 (a low carbon steel) long radius pipe elbow using a loop apparatus. Potash slurry (containing 95.6 wt.% KCl and 3.2 wt.% NaCl, and 1.2 wt.% Insoluble) with different sand concentrations (10, 20, and 30 wt.% particles) are circulated at a flow velocity of 4 m s^{-1} for five days. Authors have found weight loss, surface roughness, and hardness are highest at the downstream side of the elbow where the sand concentration is also highest (Elemuren et al. 2019). It also analyzed the slurry EC behavior of AISI 1018 steel and observed that the EC rate of steel pipe elbow was enhanced by the wear phenomena. The tests were carried out for 120 h and found that the EC rate is directly proportional to the fluid velocity (2.5, 3, 3.5, and 4 m s^{-1}) and sand concentration (10, 20, and 30 wt.%) (Elemuren et al. 2018). The surface morphology of the EC sample

was examined using SEM and found evidence for pitting corrosion. The Raman spectra show the existence of γ-FeOOH, α-FeOOH, α-Fe_2O_3, and Fe_3O_4 as corrosion products (Elemuren et al. 2020).

Walczak et al. conducted experiments to analyze the erosion-corrosion behavior of X65 steel coupled with modeling. The EC tests were done using an impingement test rig which circulates a slurry containing different chloride concentrations of 0.005, 0.05, and 0.5 M and silica particles (250–350 μm) with a velocity of 3 m s^{-1}. They have concluded that high chloride ions directly influence and play a significant role in the erosion-corrosion of low carbon steel (Walczak et al. 2020).

Islam and Farhat investigated the combined effect of erosion and corrosion of X70 line pipe steel under an impingement slurry (containing 2.0 g/L NaCl and Al_2O_3 particles) flow condition. The test outcomes revealed that erosion and corrosion mutually increase one another, hence an additional material removal. They found that damage mechanisms include plastic deformation and fracture of worn surfaces. Moreover, slurry EC eliminates the work-hardened layer along with the passive layer and enhances erosion-corrosion of the X70 steel (Islam and Farhat 2013). The authors also presented a comparative EC study of different API (X42, X70, and X100) steels under a similar environment. It is found that X100 steel exhibited maximum EC resistance as compared to X42 and X70 because of better surface properties and corrosion resistance (Islam and Farhat 2017).

Khan et al. studied the EC behavior of two different steel pipe elbows. EC tests were conducted by utilizing a loop system. Silica sand particles (average size 50 μm and concentration of 5 wt.%) were dispersed in water and circulated. They observed that the EC rate is about four times more in AISI 1018 as compared to Grade 304L stainless steel. A higher erosion rate is noticed at the exit side of the elbow due to high particle-wall impaction (Khan et al. 2019).

2.13 Tools for the investigation of FAC and EC

Various tools are available for investigating flow corrosion and erosion on the laboratory scale. Major tools used by the researchers include rotating probes, jet impingement system, and flow loop system. There are a number of rotating probe techniques namely rotating disk electrode (RDE), rotating cylinder electrode (RCE), and rotating cage (RC), [Figure 2.15] (Efird 2011c; Schmitt and Bakalli 2009). Each technique has its own merits and demerits. In rotating probes methods, the sample rotates in stationary electrolytes and it is appropriate to analyze the mass transfer process along with corrosion kinetics. Furthermore, this method is quite effective when the electrolyte contains a high concentration of sand particles. The jet impingement system (Figure 2.16) impinges the electrolyte or fluid to the sample from a nozzle. The main advantage of this technique is impact angle control. However, rotating probe and jet impingement techniques are not suitable choices to replicate the flow regime of a practical pipe flow. The flow loop system (Figure 2.17) is more suitable to investigate the flow corrosion and erosion by imitating the flow pattern more realistically. This method provides a better insight into the effect of hydrodynamic parameters on flow accelerated corrosion and erosion-corrosion (Schmitt and Bakalli 2008; Zhang et al. 2013).
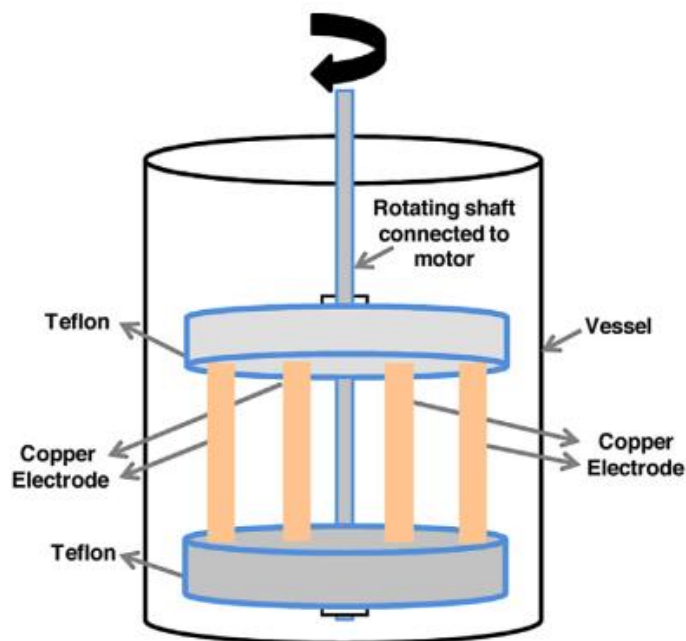
Figure 2.15 Rotating Cage (RC) with test coupons (Khan et al. 2015)

34
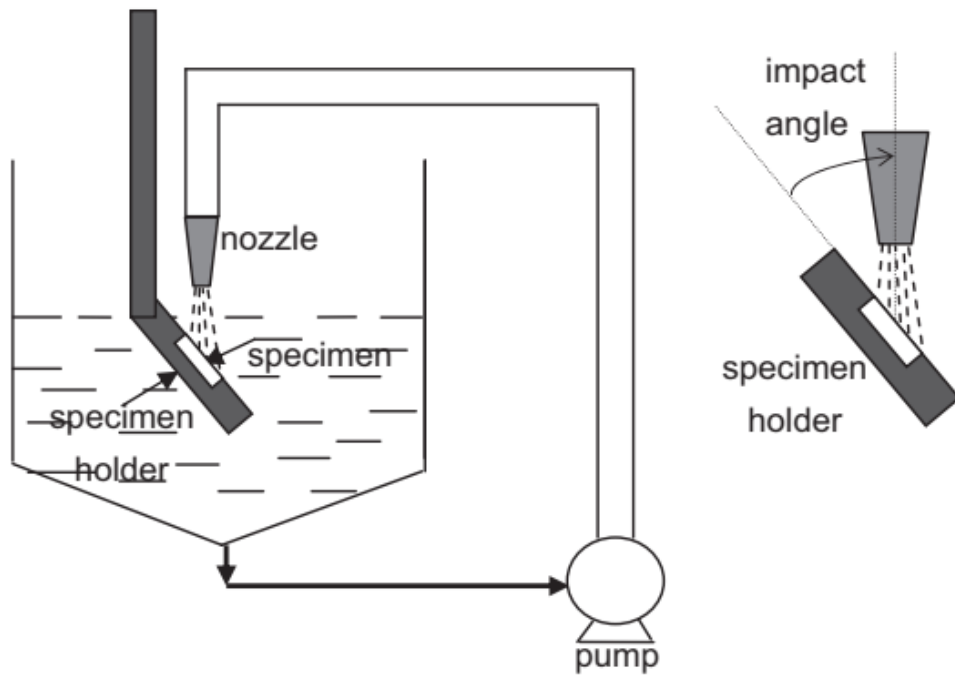
Figure 2.16 Jet impingement system (Zhao et al. 2015)
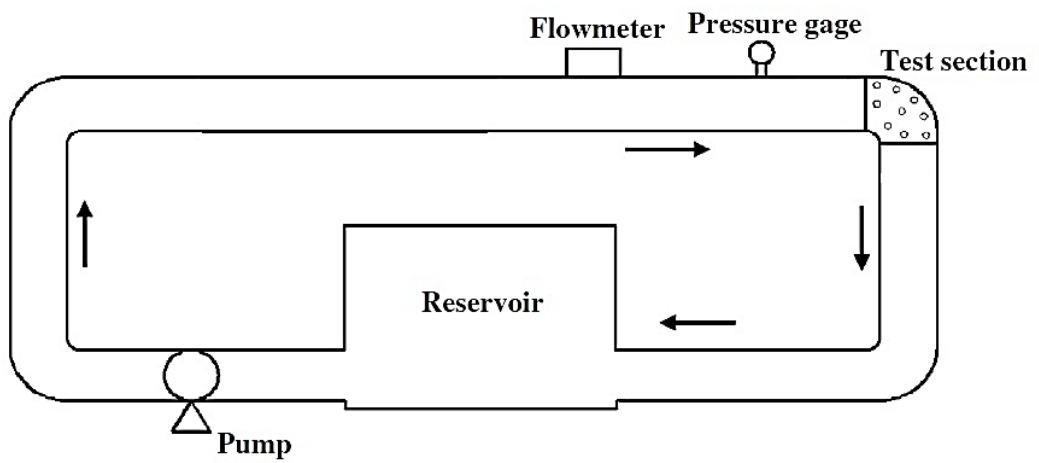
Figure 2.17 Schematic of a flow loop system (Zhang et al. 2013)

2.14 Summary of literature and importance of the study

Flow accelerated corrosion (FAC) and erosion-corrosion (EC) are the major threat to the low carbon low alloy steel pipelines of the oil gas industry particularly at the pipe elbow due to the complex flow pattern. It is necessary to study the FAC behavior of 90° pipe elbow under an Indian oilfield water environment using a circulating flow loop apparatus, which can simulate the functional conditions of a practical piping system more realistically. API X70, one of the widely used (in oil and gas field) line pipe steel is chosen for this study. Computational fluid dynamics (CFD) analysis can be used for a better understanding of the synergetic effect of electrochemical behavior and hydrodynamics.

Researchers have studied the performance of various corrosion inhibitors for pipeline applications. Most of them are not environmentally friendly. The oleic acid hydrazide (OAH), a capable green inhibitor protects the steel under static conditions. However, there is no report available to see the inhibition efficiency of OAH under flow conditions particularly at a steel pipe elbow. Since the fluid flow plays a vital role in the mass transfer process and the removal of corrosion products on the metal surface (Zhang et al. 2013), the inhibition efficiency of the OAH inhibitor on X70 steel in FAC condition needs to be examined. Furthermore, it is understood that laser surface melting (LSM) is one of the promising and cost-effective techniques, which can be used to improve the surface performance of the pipeline steels by altering surface metallurgy. It is essential to study the FAC and EC behavior of laser surface melted X70 line pipe steel at a 90° pipe elbow coupled with computational fluid dynamics (CFD).

2.15 Objectives of the study

❖ To study the Flow Accelerated Corrosion at pipe elbow using loop system and CFD.

❖ To investigate the effect of inhibition using organic inhibitors on Flow Accelerated Corrosion.

❖ To study the Erosion-Corrosion behavior using sand particles.

❖ To evaluate the effect of surface modification on Flow Accelerated Corrosion and Erosion-Corrosion.

2.16 Outline of the thesis

Chapter 1 presents the **introduction** to the research work.

Chapter 2 delivers the **literature review and importance of the study**, where a critical review on flow accelerated corrosion (FAC), and erosion-corrosion (EC) of iron-based alloys and its mitigation using inhibitors and surface modification techniques were explained.

Chapter 3 contains the **materials and methods**, where the details of the experimental setup and the procedures.

Chapter 4 contains the **results and discussion**, where all the experimental, simulation, and characterization results were explained in the following subsection.

4.1: discusses the experimental and simulation results of **flow-accelerated corrosion (FAC) of API X70 steel**.

4.2: presents the detailed investigation on the **effect of oleic acid hydrazide inhibitor on FAC of X70 steel**.

4.3: discusses the experimental and characterization results of the **effect of laser surface melting on FAC of X70 steel**.

4.4: discusses the results of the experiments and simulation on the **effect of laser surface melting on slurry erosion-corrosion of X70 steel**.

Chapter 5 delivers the **conclusions of the thesis**, presenting the significant findings from all the studies carried out towards the research objectives and the major conclusions drawn.

3   MATERIALS AND METHODS

3.1   API X70 Steel

The material used for the flow accelerated corrosion (FAC), and erosion-corrosion (EC) studies is API X70 steel. The steel was procured from JSW Bellary as 13 mm thick plate of dimension 40 × 60 mm. The chemical composition (wt.%) of X70 steel examined using OES (according to ASTM standard: E415-14) is given in Table 3.1 (ASTM 2014).

Table 3.1 Composition (wt.%) of the API X70 steel

Element	Composition (wt.%)
C	0.050
Mn	1.488
S	0.004
P	0.011
Si	0.217
Al	0.039
Cr	0.164
Ni	0.011
Nb	0.046
Mo	0.098
V	0.043
Ti	0.014
Ca	0.0027
B	0.0003
N	0.0045
Fe	Balance

▪ **Microstructure of the as-received API X70 sample**

A small section of API X70 steel obtained from the plate is used for the microstructural examination, which is sectioned through the wire electrical discharge machining (EDM) to avoid thermal effects on the microstructure and other properties such as corrosion and hardness. The sample was ground by 320, 400, 600, 800, 1000, 1200 grit emery papers and further cloth polishing was done up to 0.5-1-micron diamond paste to achieve a mirror finish surface. The samples were cleaned with deionized water and acetone, followed by ultrasonication for final cleaning to start experiments. The dried sample is etched with a 2% nital solution for 30 s. The microstructure of steel was observed using an optical microscope (Axio Lab.A1 by ZEISS Germany).

3.2 Design and fabrication of flow loop system for FAC and EC tests

A piping loop apparatus is utilized in this flow accelerated corrosion and erosion-corrosion study that can imitate the flow pattern in a piping system more realistically (Zeng et al. 2015). The flow loop system containing an in-house design and assembly of pipes, a centrifugal pump, a reservoir, a paddle-wheel flow meter, a pressure gauge, and a 90º elbow test section is illustrated in Figure 3.1. Polypropylene pipes with an inner diameter (D) of 48 mm were used to fabricate the flow loop system. The centrifugal pump with 1 HP Motor was used to circulate the electrolyte through the loop system at a flow velocity of 3 m s^{-1} from a 40 L reservoir. The surfaces of pump interior parts, which will contact the electrolyte, such as the impeller and casing wall, were coated with an erosion-corrosion resistant, industrial polymer coating, Rilsan$^{®}$ Fine Powders by Arkema France. To understand the basic characteristics of fluid flow and determine the entrance length, the density, viscosity, Reynolds number are calculated. The calculated values of density, kinematic viscosity, and dynamic viscosity of the fluid are 1030.4 kg m^{-3}, 0.7178 mm^2 s^{-1}, and 0.00074 kg m^{-1} s^{-1} respectively. Reynolds number based on fluid characteristics, flow velocity, and the dimension of the pipe was obtained as 200613. Since the Reynolds number is much greater than 4000, the fluid flow is turbulent. To achieve a fully developed steady flow at the elbow test section, sufficient entrance length (L_e) must be provided. Since the fluid flow is turbulent, the entrance length is 50 times the hydraulic diameter (D) (Shalaby 2018a). The loop system was fabricated by providing the minimum entrance length 2.4 m at the

upstream of the elbow test section. To eliminate the recirculation of the fluid, 1.3 m length was given downstream of the elbow test section. The detailed calculations are provided in the appendix.
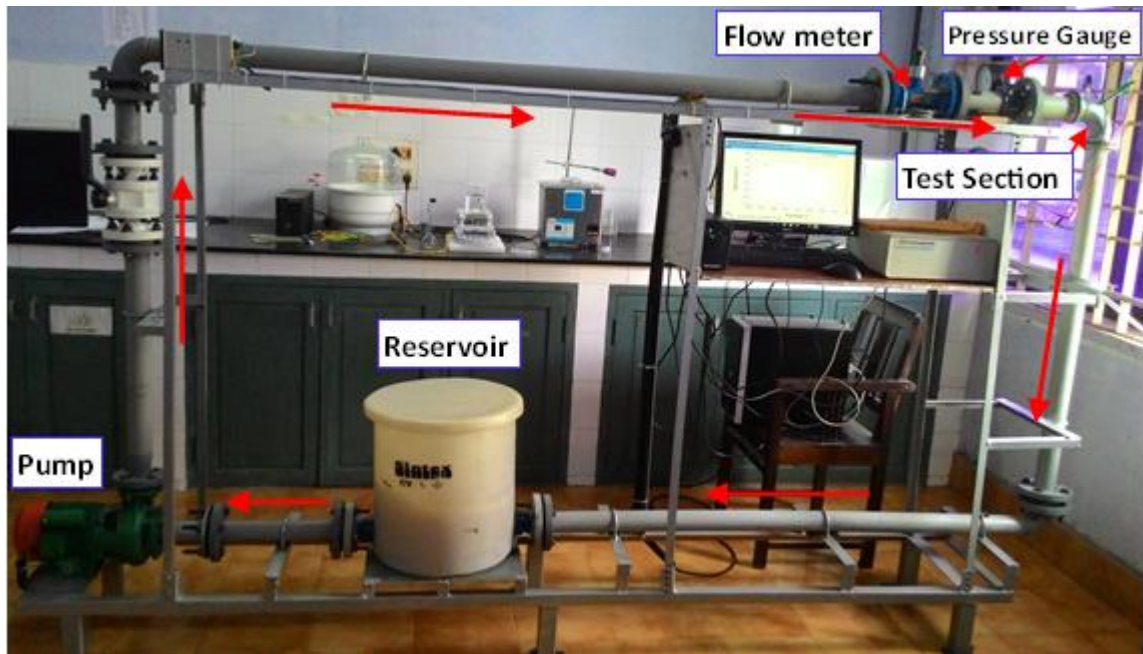
Figure 3.1 Photograph of fabricated flow loop system

3.3 In-situ corrosion and erosion-corrosion tests

- **Electrochemical measurements for FAC and EC study**

Electrochemical measurements were performed by utilizing a potentiostat with a computer as per the ASTM standard (ASTM G3 2013). For that, a three-electrode electrochemical cell was incorporated into the elbow test section as shown in Figure 3.2a. API X70 steel samples, a platinum plate, and a saturated calomel electrode (SCE) were utilized as working electrodes (WE), a counter electrode (CE), and a reference electrode (RE) respectively. All the electrochemical tests were conducted after 5 h of stabilization run in the loop system. The electrochemical impedance spectroscopy (EIS) experiments were carried out at open circuit potential (OCP) with a sinusoidal alternating amplitude of 10 mV from 10,000 Hz–0.1 Hz to obtain the charge transfer resistance (R_{ct}). The Tafel extrapolations were conducted at −250 to +250 mV (SCE) vs OCP with a scan rate of 0.5 mV s^{-1} to quantify the corrosion rate. The electrochemical experiments and analyses were carried out by using an SP-150 Bio-Logic Potentiostat

with the help of EC-Lab® V10.44 software. The same input parameters were used for conducting electrochemical corrosion tests in static conditions for ease of comparison. All the tests were conducted at room temperature and atmospheric pressure.
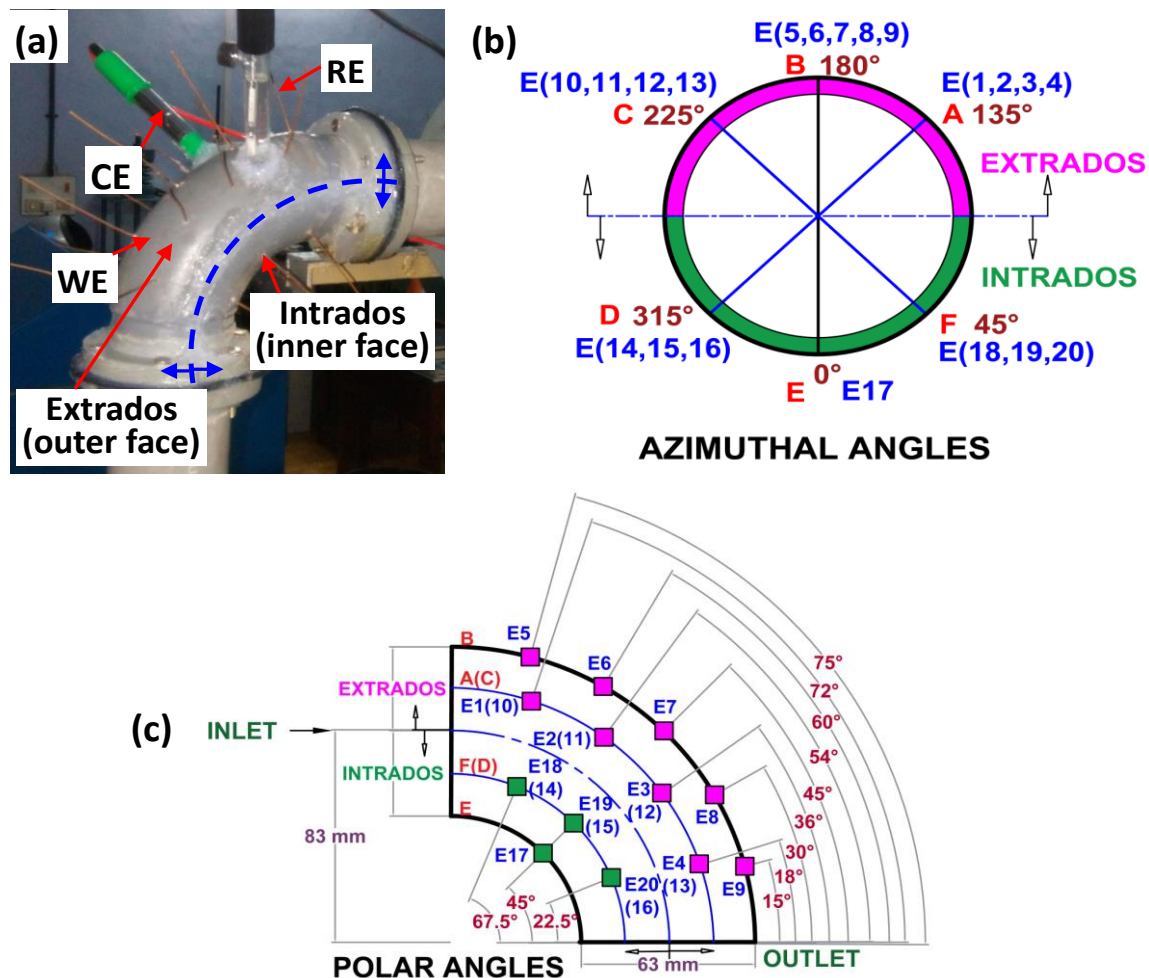
Figure 3.2 (a) Distribution of electrodes at 90° pipe elbow test section (b) azimuthal angles with annotation of angles φ, (c) polar angles with annotation of angles θ

▪ **Weight loss measurement for erosion-corrosion (EC) study**

After continuous 14 h of EC tests, all the working electrodes were removed carefully, cleaned based on ASTM standard (ASTM G1 2003), and weight loss was measured using a CONTECH high precision balance (CAS-234) with an accuracy of 0.0001 g to obtain the EC rate.

42

3.4   Position of electrodes at 90º elbow test section

A detailed illustration of the 90º elbow test section is given in Figure 3.2(a-c). After polishing and drying, the test specimens with an exposed area of 5×5 mm were joined to copper wires to establish the electrical connections for electrochemical analysis. A total of twenty test specimens including 13 at the extrados (outer face) and 7 at the intrados (inner face) are anchored and fixed into the elbow test section using silicone sealant. It was applied in such a way that it does not block the fluid flow over the electrodes. The electrodes E1, E2, E3, and E4 in column A are located at the extrados of the elbow test section at a common azimuthal angle (φ) 135º and polar angles (θ) 72º, 54º, 36º, and 18º respectively. The electrodes E5, E6, E7, E8, and E9 in column B are located at the extrados of the elbow test section at a common azimuthal angle (φ) 180º and polar angles (θ) 75º, 60º, 45º, 30º, and 15º respectively. The electrodes E10, E 11, E12, and E13 in column C are located at the extrados of the elbow test section at a common azimuthal angle (φ) 225º and polar angles (θ) 72º, 54º, 36º, and 18º respectively. The electrodes E14, E15, and E16 in column D are located at the intrados of the elbow test section at a common azimuthal angle (φ) 315º and polar angles (θ) 67.5º, 45º, and 22.5º respectively. The electrode E17 in column E is located at the intrados of the elbow test section at an azimuthal angle (φ) 0º and a polar angle (θ) 45º. The electrodes E18, E19, and E20 in column F are located at the intrados of the elbow test section at a common azimuthal angle (φ) 45º and polar angles (θ) 67.5º, 45º, and 22.5º respectively. The angles for locating the electrodes are selected by giving some gap between two electrodes to understand the synergetic effect of hydrodynamic parameters and electrochemical reactions of X70 steel on FAC at various sites of the pipe elbow.

3.5   Composition of the oilfield water

A simulated oilfield (Indian) water solution was used as the electrolyte in this study. The composition of synthetic oilfield water is given in Table 3.2. The pH of this synthetic solution prepared from analytical grade (Sigma-Aldrich) reagents was 7.5.

Table 3.2 Chemical composition of synthetic oilfield water

Chemical compound	Weight per liter (g/L)
NaCl	47.385
$MgCl_2$	0.5718
$MgCO_3$	0.5069
$CaCO_3$	0.7985
$NaHCO_3$	1.931
$CaSO_4$	0.1415

3.6   Oleic Acid Hydrazide (OAH) inhibitor for FAC study

OAH inhibitor is a mixture of ethyl oleate (0.042 mol) and hydrazine hydrate (0.042 mol) in ethanol (120 ml) which was refluxed on a water bath for 3 h. After completion of the reaction, the solvent was removed and dried. The residue was poured into the ice-cold water under mechanical agitation to get the homogeneous product. The mass obtained was filtered, washed with water, and recrystallized from ethanol (Jayaroopa et al. 2013). The chemical structure of OAH is shown in Figure 3.3. The concentrations of OAH used in the FAC study were 0.05 g/L (0.168 mM), 0.15 g/L (0.506 mM) and 0.30 g/L (1.012 mM). Before mixing with the electrolyte, the OAH was dissolved in acetone in the ratio of 1:5 (OAH to acetone) and formed various concentrations of OAH.

$$CH_3 — (CH_2)_7 — CH = CH — (CH_2)_7 — \overset{\displaystyle O}{\overset{\displaystyle \|}{C}} — NHNH_2$$
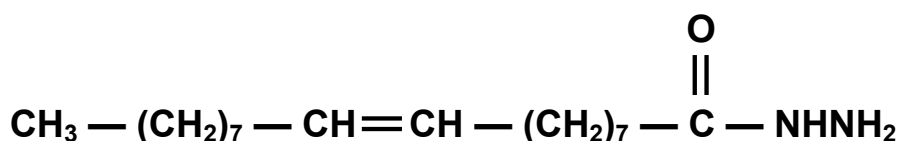
Figure 3.3 Chemical structure of Oleic Acid Hydrazide (Quaraishi et al. 2000)

3.7   Silica sand (erodent) particles for erosion-corrosion (EC) tests

Silica sand particles with an average size of 400-500 µm with sand loading of 1.5 wt.% were used as erodent particles in erosion-corrosion experiments. Before the EC tests, the silica sand particles were washed in boiling water, hydrochloric acid, acetone, and deionized water to eliminate the contaminations and microorganisms. From the SEM image (Figure 3.4), it is clear that the sand particle grains have sharp corners and edges.

In general, the range of silica sand hardness is about 750–1200 HV, higher than steel hardness (Ajmal et al. 2019; Gheisari and Polycarpou 2018). The density of the sand particles used in this study is 2153 kg m^{-3}. The sand particle density calculation is provided in the appendix.
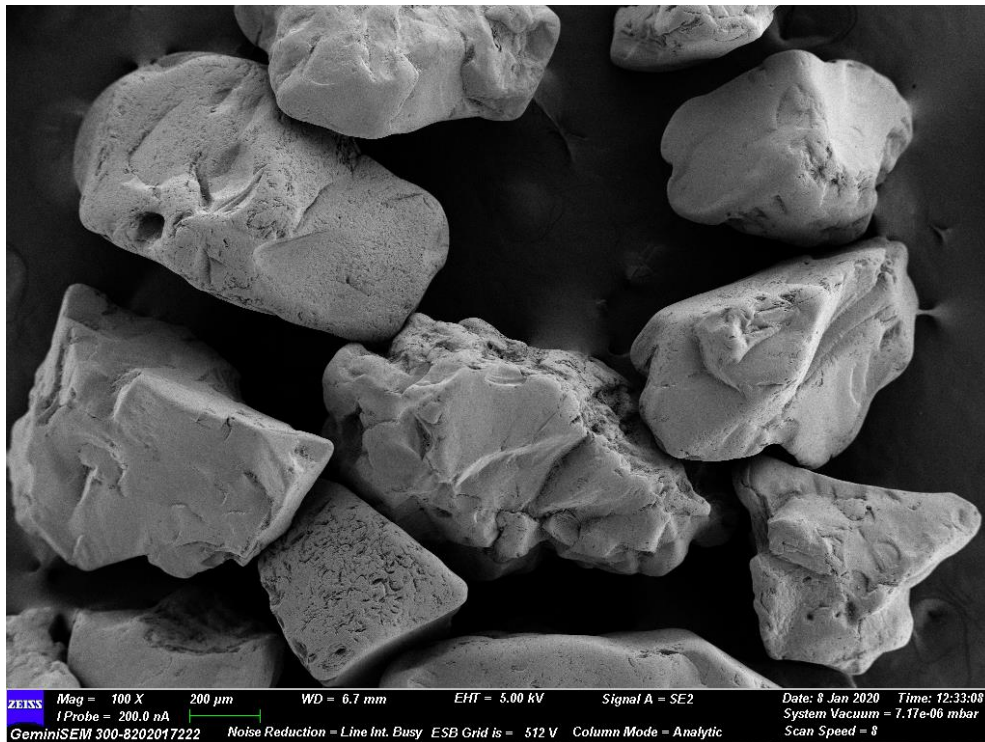
Figure 3.4 SEM image of silica sand (erodent) particles used in the EC study

3.8 Laser surface melting (LSM) of API X70 steel

LSM of the API X70 steel plates (13 mm thickness) was carried out utilizing a 10-kW diode laser (LDF-60-10000, Laserline GmbH, Germany) integrated to 1000-micron fiber (NA: 0.22 micron) and 6+2 axis robotic workstation. Figure 3.5 illustrates the processing setup utilized for laser surface melting. A 20 × 5 mm laser beam with a multi-mode intensity profile (top-hat profile in slow axis and Gaussian profile in fast axis) obtained by employing a combination of collimating, homogenizing and focusing optics was used for the purpose. The rectangular laser beam of 915–1050 wavelength was focused at 185 mm on the surface of the steel plate and scanned with a speed of 10 mm s^{-1}, laser powers of 2, 2.5, and 3 kW (under pulsed mode with 90-millisecond pulse width and 10 Hz frequency) and under nitrogen-shielding (at 2 bar pressure) atmosphere. The laser powers and the scanning speed selected for the purpose were

45

based on preliminary experiments performed for assessing the influence of processing parameters in obtaining an LSM depth of more than 300 microns on the X70 steel plate of 13 mm thickness.

Figure 3.5 Laser processing setup integrated with a robotic system

3.9 Surface analyses

- **SEM analysis**

A detailed surface observation is the first step of a scientific study. Compared to a traditional optical (light) microscope, a scanning electron microscope (SEM) offers clear, high-resolution images of the sample surface. SEM utilizes an electron beam whose wavelength is shorter than that of light and targets the specimen, which interacts with the atoms of the sample. It leads to the formation of a high-resolution image with nano-scale features by detecting secondary electrons (Zhou et al. 2007). The higher magnification SEM images deliver much useful information regarding the morphology of the sample. In this work, the surface morphologies of the representative corroded samples were examined with the help of an SEM by ZEISS (GeminiSEM 360) Germany, after the FAC and EC tests. It helps to analyze the protective nature of the

46

corrosion products formed on the surface of the sample. The operating voltages used in this study were 5 kV, 10 kV, 15 kV, and 20 kV. The mode of operation was secondary electron imaging mode.

- **Surface and cross-sectional microstructure**

To understand the microstructural changes that occurred by laser surface melting, detailed analysis of surface and cross-sectional microstructures of the UT and LSM samples were performed using an optical microscope (Axio Lab.A1 by ZEISS Germany) and SEM (by JEOL JDX-3530, Japan). Before the examination polishing and etching were done as described in *section 3.1*.

- **EDS analysis**

EDS (Energy Dispersive X-Ray Spectroscopy) is an analytical technique used for the elemental analysis or chemical characterization of a sample. It identifies the elements present along with their distribution and concentration by detecting the X-ray. These X-rays are generated by the following process. The electron beam hits the inner shell of an atom and knocks off an electron and leaves a positively charged hole which attracts another electron from an outer shell to fill the vacancy. Then an electron moves from the outer higher-energy to the inner lower-energy shell and releases the characteristic X-ray. The energy of this X-ray is unique to each element (Anderhalt 2007). In this work, the EDS analysis was performed on UT and LSM sample surfaces. This study helps to determine the atomic composition of the elements segregated at the grain boundaries of the samples.

- **Raman spectroscopy analysis**

Raman spectroscopy identifies the chemical compound and molecular structure. This non-destructive chemical analysis technique works based on the interaction of light with the chemical (molecular) bonds within a material. The light scattering technique utilized by Raman spectroscopy facilitates the scattering of incident light (wavelength 750–850 nm) from a high-intensity laser light source by a molecule. A minor amount of light is scattered at different wavelengths due to the Raman effect, which provides the required chemical structure information. This scattering is termed the Raman

scattering (Synetos and Tousoulis 2018). In this work, the corrosion products (compounds) were characterized by Raman spectroscopy analysis by using a HORIBA JOBIN – YVON, LabRAM HR Raman microscope. The Raman peaks were obtained from the corrosion products (powder), which were carefully removed from the sample surface after the experiments.

- **FTIR-ATR analysis**

The existence of specific functional groups can be confirmed by the Fourier transform infrared spectroscopy – attenuated total reflectance (FTIR–ATR) technique. The variations in the chemical structure (surface chemistry) or alteration in the environment are confirmed by the shift in the FTIR spectrum (frequency of absorption bands) and intensity variations (Anderson and Voskerician 2010). In this work, the adsorption of the oleic acid hydrazide (OAH) inhibitor molecule on the specimen was confirmed by FTIR- ATR analysis.

- **XPS analysis**

X-ray photoelectron spectroscopy (XPS) is a surface analysis technique that works based on the photoelectric effect. It is used to confirm the presence of an element and species of an element based on the electron configuration of an atom and chemical bonds. Each element has characteristic binding energy. The binding energy varies depending upon the chemical environment of the atom. The achievable analysis depth of this surface chemistry study is about 10 nm and it requires an ultra-high vacuum (Verma 2007). In this work, the presence of oleic acid hydrazide (OAH) inhibitor film on the exposed electrode surface was confirmed by XPS analysis by utilizing an X-ray photoelectron spectrometer (Thermo scientific, Multilab 2000).

- **Microhardness analysis**

Hardness, a characteristic of a material, is defined as the resistance to indentation (the smaller the indentation, the harder the material). The Vickers hardness testing method works based on an optical measurement system. According to ASTM E-384 standard, hardness value can be obtained by converting the measured indentation, that formed by the application of a light load with a diamond indenter at a definite dwell time.

Microhardness measurements on the surface as well as across the treated layer depth were carried out on untreated (UT) and laser surface melted (LSM) samples utilizing a Vickers micro-hardness-testing machine (SHIMADZU HMV-G20ST Version 1.03) with 0.2 kg load for 15 seconds. A pyramidal indenter (angle between opposite forces at the vertex of 136°) was utilized for this study.

- **XRD analysis**

X-ray diffraction (XRD) is an analytical technique used to perform the microstructural analysis of crystalline material. It can be used to determine the crystallographic structural properties such as lattice parameters, crystallite size, micro-strain, crystal imperfections, and crystalline phases by a detailed analysis of a diffraction pattern (Cullity and Stock 2001). A qualitative microstructural analysis was conducted on UT and LSM (2.5 kW) sample surfaces by XRD with Cu-Kα radiation (wavelength of 1.542 Å). The X-ray diffractometer used for this study (D/MAX-RAPID II, Rigaku, Japan) is a highly sophisticated and sensitive equipment, available on the laboratory scale.

- **EBSD analysis**

Electron backscatter diffraction (EBSD), when working with a Scanning electron microscopy (SEM), assists for the characterization of the grain orientations, local texture, and phase identification of a material (Schwarzer et al. 2009). In this study, the EBSD technique was utilized to analyze the microstructures and phase transformation of untreated (UT) and treated (LSM) samples, more effectively and efficiently than the traditional light microscopy or SEM. A surface area of 200×80 μm^2 [Radial Direction (RD) × Transverse Direction (TD)] was scanned with a step size of 0.15 μm and a magnification of 1000X. The SEM-EBSD system used for this scan was Hitachi S3400N- TSL Hikari, Tokyo, Japan.

- **AFM analysis**

The atomic force between the probe and the sample surface facilitates the observation of the surface topography (primary shape) by the atomic force microscopy (AFM) technique. This advanced surface analysis provides high-resolution 3D nano-scale

images which can be used to understand the properties such as morphology, surface texture, and roughness. The AFM scan permit the characterization of the particles with a wide range of sizes (1 nm to 8 µm) and it works based on the van der Waals forces between the sample and the AFM tip (Barceló and Farré 2012). In this study, AFM was also utilized to observe the 3D surface topographies of the eroded sample surfaces by using Park systems AFM – NX 20 with tapping mode in the air, silicon nitride probe; k = 42 N/m and f_o = 300 kHz, at 20 µm.

- **Optical profilometry analysis**

Surface features such as irregularities and topography can be detected by conducting a non-contact optical profilometry (OP) scan that utilizes light. The wear-scar analysis can be accurately done by this simple and cost-effective method with the vertical resolution of several angstroms and lateral resolution in the range of 0.3 - 0.5 µm (Visscher and Struik 1994). The 3D surface topographies and surface roughness parameters of the demonstrative eroded samples (wear profile) were obtained by optical profilometry scans using Taylor Hobson PRECISION (TALYSURF CCI) optical profilometer. All profilometry scans were performed according to ISO 25178-2 standard (ISO 25178 2012).

3.10 Computational fluid dynamics (CFD) simulation

Professional fluid simulation software ANSYS FLUENT was utilized for the computational fluid dynamics (CFD) simulation. A 3D geometrical model which is matching with the loop system used for the study was drawn using pre-processing software Gambit. The horizontal pipe, upstream of the elbow test section, was set as 2.4 m to reach a fully-developed steady flow, before entering the elbow (test section) region. The vertical pipe downstream of the elbow test section exit was set as 1.3 m to avoid possible backflow at the outlet of the elbow. The interval size of 0.004 m was selected for volume meshes. To get more stability and to generate less diffusivity, hexahedral cells were utilized in the simulation. The simulation was executed in two stages.

- **Single-phase CFD analysis**

In the first stage, single-phase flow (only liquid phase) was considered, and the behavior of fluid flow at the elbow test section was analyzed. The boundary conditions were fixed as the flow velocity of 3 m s^{-1} at the inlet and a pressure outlet at the outlet. Reynolds number 200613 (>4000) recommend that the fluid is in turbulent flow condition (Murdock 2006). The density and viscosity of the fluid were calculated and set as 1030.4 kg m^{-3} and 0.00074 kg m^{-1} s^{-1} respectively. The fluid was considered incompressible. Hence, the numerical simulation was solved by using K-ε turbulent model (double equation model). Turbulent kinetic energy (K), the measure of the intensity of turbulence of fluid, the kinetic energy per unit mass of the turbulent fluctuations, was set as 1 m^2 s^{-2}. The rate at which turbulent kinetic energy is converted to internal thermal energy is the turbulent dissipation rate (ε), which was set as 1 m^2 s^{-3} (Huang et al. 2016; Zhang et al. 2013). Turbulent intensity (I) obtained from the Reynolds number was fixed as 3.5% (Ajmal et al. 2019; Zeng et al. 2016b). The inner wall roughness of the polypropylene pipe was set as 10 μm. A convergence criterion of 1×10^{-10} was utilized to solve the K-ε turbulent equation by the iterative method.

- **Multiphase CFD analysis**

In the second stage, the numerical simulation of two-phase flow (liquid with sand particle) was performed. To examine the contours of erosion rate and sand concentration at the elbow test section, the discrete phase model (DPM) was enabled to a single-phase flow model by adopting the two-way coupled Eulerian-Lagrangian approach. The liquid phase was considered as a continuous phase and sand particles as a discrete phase. The sand particles were treated as inert particles with an average size of 0.5 mm. The primary and secondary phases were set as liquid and solid, respectively. The density of the sand particles was set as 2153 kg m^{-3}. The sand particles' mass flow rate based on sand loading (1.5 wt.%) of the erosion-corrosion test was set as 0.175 kg s^{-1}. The mass flow rate calculation of sand particles is provided in the appendix.

4   RESULTS AND DISCUSSION

Pipeline corrosion is a critical problem in almost all industries including petroleum, gas, refineries, nuclear, and water transportation. However, flow accelerated corrosion (FAC) and erosion-corrosion (EC) are found to be a dominating factor of failure of materials due to the presence of an aggressive corrosive environment and slurry in the pipeline. This chapter deals with understanding the corrosion and erosion-corrosion kinetics and their influence by hydrodynamic parameters such as velocity and shear stresses at the 90º elbow test section. It also explored the possible mitigation strategies using green inhibition and surface modification to improve the life of the pipeline (API X70 steel). Results and discussion chapter consists of four sections as (i) Flow-accelerated corrosion of X70 steel, (ii) influence of various concentration of green inhibitor (Oleic acid hydrazide - OAH) on FAC, Effect of laser surface melting (LSM) on (iii) FAC and (iv) EC in simulated oilfield solution.

4.1   Flow-accelerated corrosion (FAC) of API X70 steel

The effect of flow accelerated corrosion on API X70 steel was studied in the simulated oil field water. Twenty electrodes were placed at the 90º elbow test section of the flow loop system which can imitate the flow pattern in a piping system more realistically. A comparative study of the electrochemical analyses and the computational fluid dynamic (CFD) simulation was performed in the pipe elbow to understand the synergetic effect of electrochemical reactions and hydrodynamics in FAC. Surface morphology and corrosion products were examined using characterization tools, SEM, and Raman spectroscopy.

4.1.1   *Microstructure of API X70 steel*

It is well known that microstructural characteristics directly influence the mechanical, tribological properties, and corrosion behavior of steel (Verlinden et al. 2007). To examine a microstructure of the as-received API X70 line pipe steel, a standard metallographic method was used, the obtained microstructure is shown in Figure 4.1. It is found that ferrite and pearlite are the major constituents in the microstructure of the steel. A large amount of ferritic phase matrix appears as white in color and non-uniform polygonal shapes, whereas the pearlite appears as dark in color. Other researchers also

reported that thermomechanical treated steel exhibited a mixture of ferritic and pearlitic microstructure (Cervantes-Tobón et al. 2014; Villalobos et al. 2018).
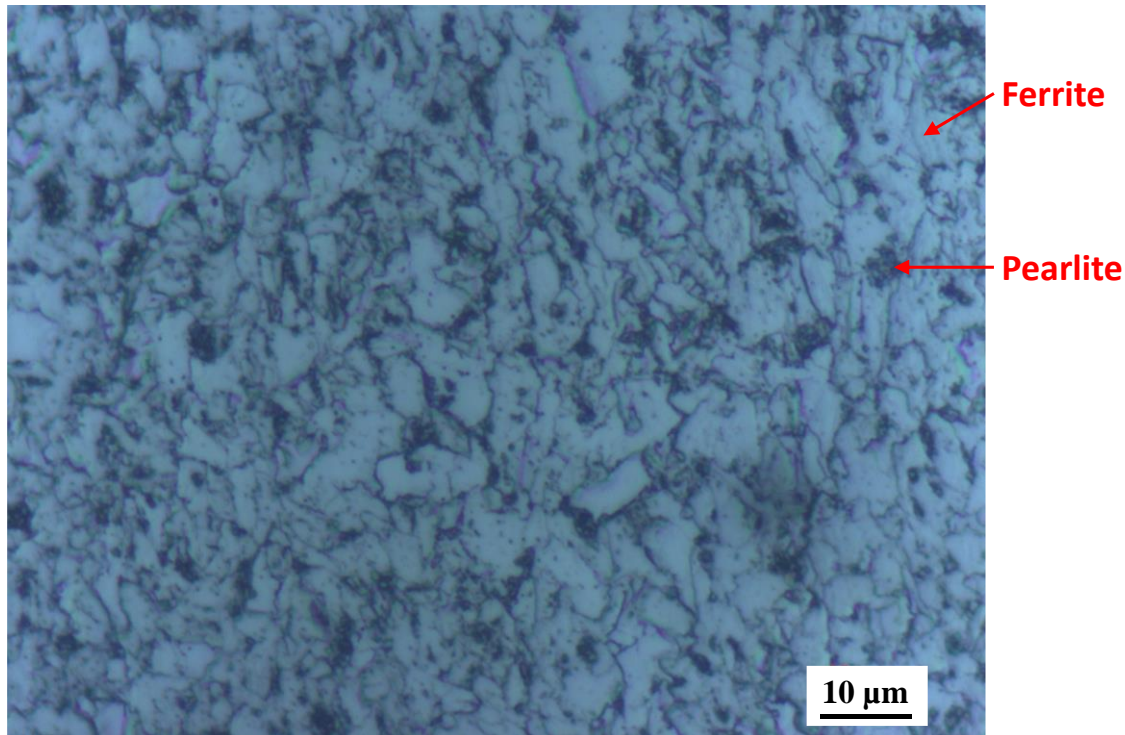
Figure 4.1 Optical micrograph of as-received API X70 steel (1000X)

4.1.2 Phase analysis of API X70 steel

X-ray diffraction technique (using Cu-Kα radiation) is used to examine phases present in the API X70 steel. The recorded X-ray diffractogram is shown in Figure 4.2. Lattice parameters and the Miller indices (hkl) of lattice planes are calculated by considering the wavelength of Cu-Kα radiation (1.542 Å). The lattice planes were identified as (110), (200), (211), and (220) which are corresponding to Bragg's diffraction angles (2θ) of 44.56º, 64.80º, 82.17º, and 98.77º respectively (JCPDS: 03-065-7528 and 01-085-1410). These peaks and corresponding Miller index confirm the presence of the bcc-ferritic phase (α). Furthermore, a minor peak at the lower diffraction angle of about 40.03° represents the presence of cementite [(hkl):(201), (JCPDS: 01-072-1110)]. These results obtained from the XRD data proved the presence of pearlite (a mixture of α and Fe_3C) in the X70 steel which is also confirmed through the microstructure observed in Figure 4.1 by optical microscope (Benarrache et al. 2019; Masoumi et al. 2019).
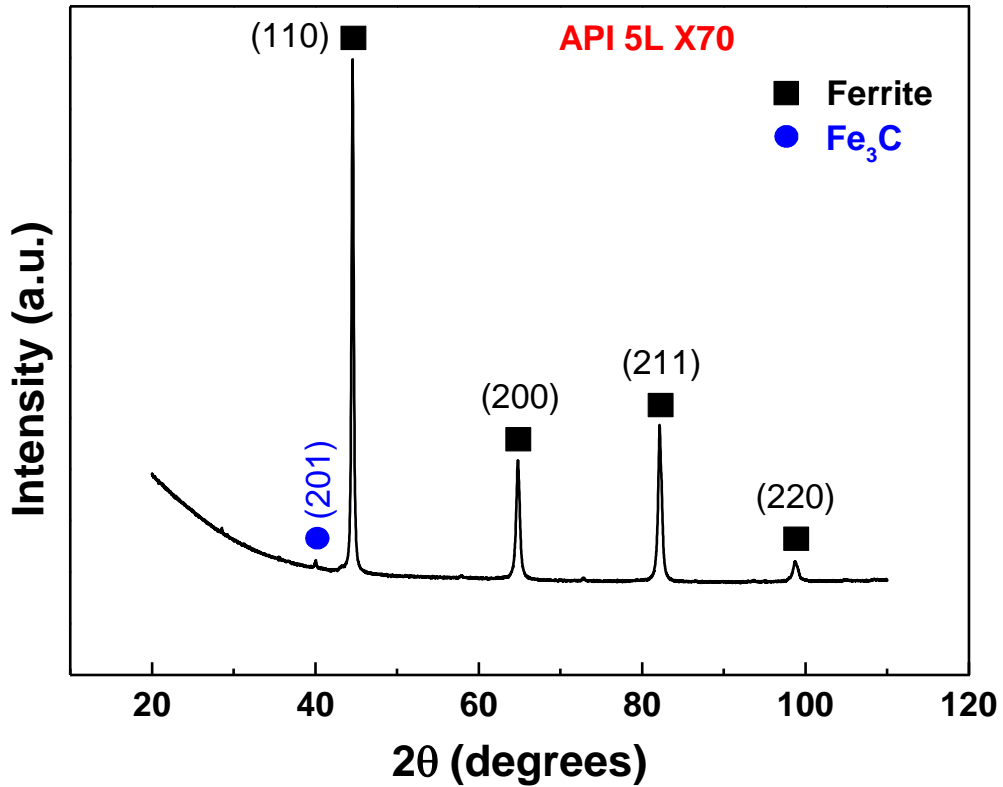
Figure 4.2 X-ray diffractogram of as-received API X70 steel

4.1.3 *Computational fluid dynamics (CFD) simulation*

CFD results, including velocity contours and wall shear stress contours, were obtained by post-processing simulation data and shown in Figure 4.3(a, b) and Figure 4.4(a, b), respectively. The magnitudes of shear stresses obtained from CFD simulation are listed in Table 4.1. From the cross-sectional planar views (Figures 4.3b and 4.4b), it is clear that the velocity and wall shear stress at the 90º elbow test section are proportional with the reference to the central plane of the pipe. It is also revealed that compared to extrados, fluid velocity and wall shear stress are greater at the intrados. It is interesting to see a small variation in shear stress values at columns A, B, and C for extrados of the elbow [see Figure 3.2(a-c)]. However, at different polar angles, shear stresses were significantly changed due to high turbulence and flow velocity at the extrados. Similarly, to examine and compare shear stress at various polar angles at the intrados for different columns D, E, and F with respect to the extrados columns of A, B, and C. It is found that the significant increment of shear stress at different polar angles and fixed azimuthal angle along the flow direction ($\theta = 90º$ to $\theta = 0º$). The lowest shear

stress 8.4 Pa is obtained at the extrados electrode E5 ($\theta = 75º$, $\varphi = 180º$) and the maximum wall shear stress 27.6 Pa is simulated at intrados electrode E17 ($\theta = 45º$, $\varphi = 0º$).

(a)

(b)

θ = 0°   θ = 20°   θ = 45°   θ = 70°   θ = 90°
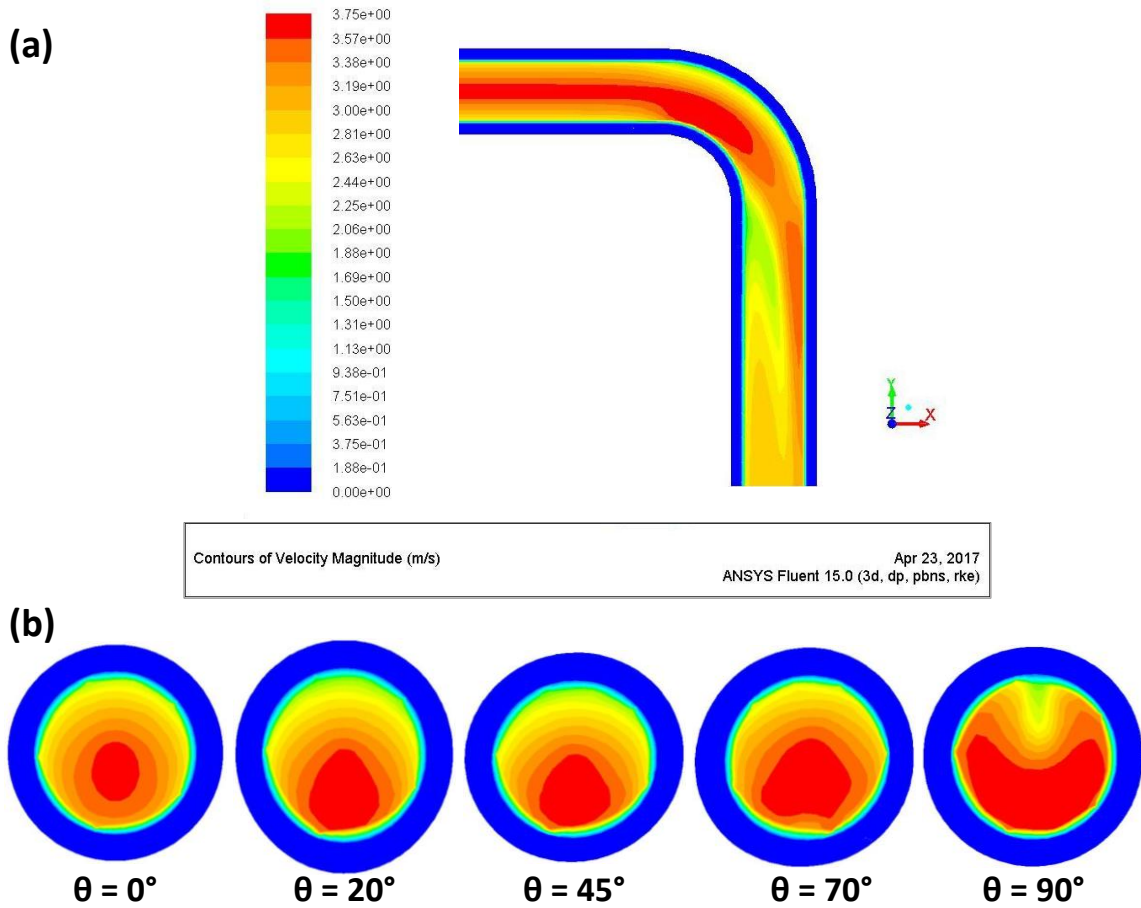
Figure 4.3 Contours of velocity magnitude for elbow test section obtained by CFD simulation (a) elbow view, (b) cross-sectional planar views at various angles of elbow

(a)

3.55e+01	
3.43e+01	
3.30e+01	
3.18e+01	
3.05e+01	
2.93e+01	
2.81e+01	
2.68e+01	
2.56e+01	
2.43e+01	
2.31e+01	
2.19e+01	
2.06e+01	
1.94e+01	
1.82e+01	
1.69e+01	
1.57e+01	
1.44e+01	
1.32e+01	
1.20e+01	
1.07e+01	

Contours of Wall Shear Stress (pascal)

Apr 23, 2017
ANSYS Fluent 15.0 (3d, dp, pbns, rke)

(b)

θ = 0°   θ = 20°   θ = 45°   θ = 70°   θ = 90°
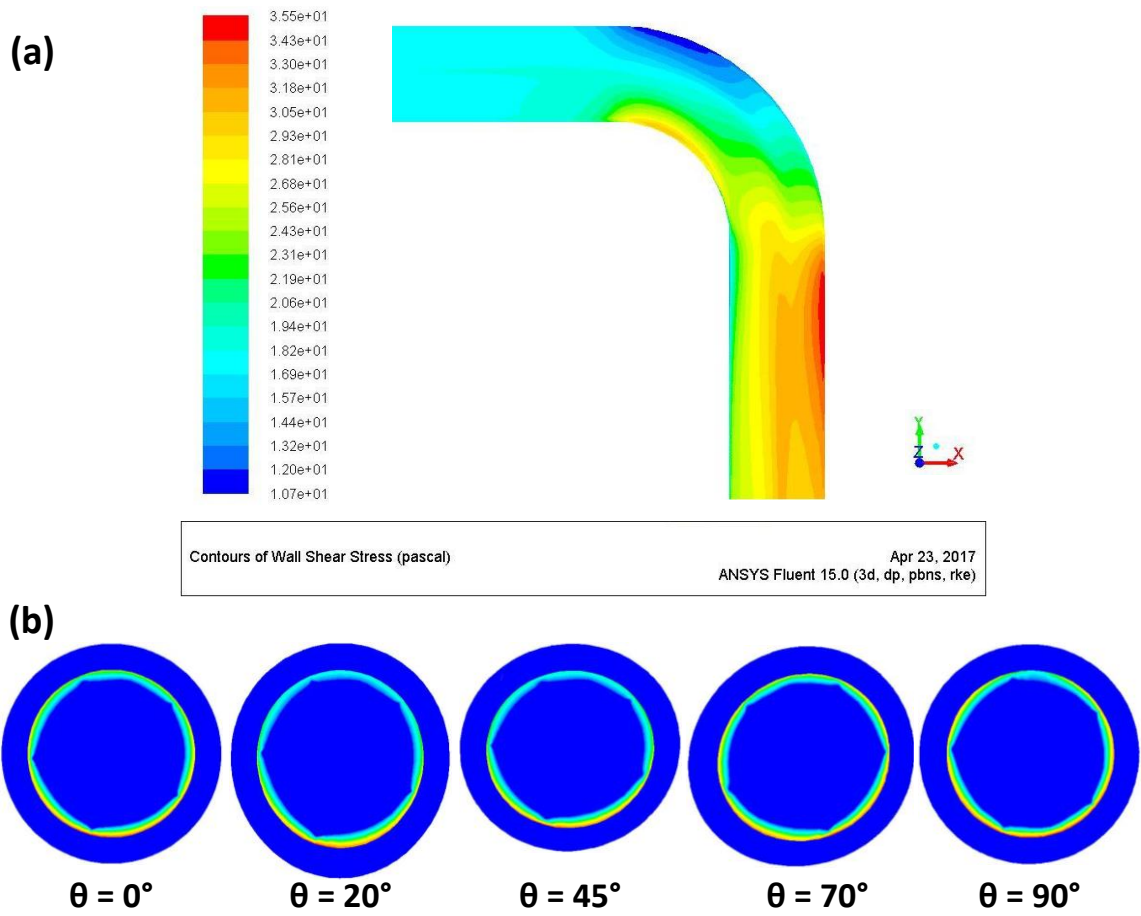
Figure 4.4 Contours of wall shear stress for the elbow test section obtained by CFD simulation (a) elbow view, (b) cross-sectional planar views at various angles of elbow

Table 4.1 Shear stress values corresponding to the electrodes located at different angles

	Azimuthal Angle (φ)	Polar Angle (θ)	Electrodes	Shear Stress (Pa)
Extrados (Outer face)	135° (Column A)	72°	E1	11.3
		54°	E2	15.2
		36°	E3	18.2
		18°	E4	20.5
	180° (Column B)	75°	E5	8.4
		60°	E6	10.5
		45°	E7	13.3
		30°	E8	16.1
		15°	E9	20.8
	225° (Column C)	72°	E10	11.5
		54°	E11	14.3
		36°	E12	17.2
		18°	E13	20.4
Intrados (Inner face)	315° (Column D)	67.5°	E14	24.8
		45°	E15	25.2
		22.5°	E16	25.6
	0° (Column E)	45°	E17	27.6
	45° (Column F)	67.5°	E18	24.0
		45°	E19	24.7
		22.5°	E20	25.7

4.1.4 Corrosion behavior

- **Under static condition**

Corrosion tests of X70 steel were carried out using the Tafel extrapolation method in the synthetic oil field water in the static condition. Tafel plot is given in Figure 4.5. Fitted corrosion kinetics parameters such as corrosion potential (E_{corr}), Tafel slopes (β_a and β_c), corrosion current density (i_{corr}) are tabulated in Table 4.2. The corrosion current density and corrosion rate under the static condition were 4.4 $\mu A/cm^2$ and 2 mpy respectively. Sherif and Almajid studied the corrosion behavior of X70 steel in static condition after its immersion for 24 h in high concentrated chloride (4.0 wt.% NaCl) solution. They noticed a corrosion rate of about 3.7 mpy (Sherif and Almajid 2015).
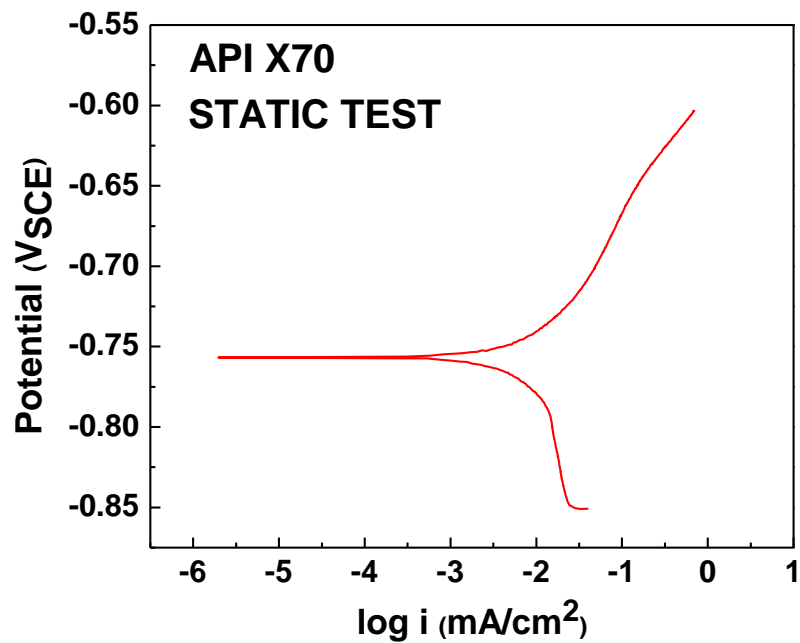
Figure 4.5 Tafel plot of API X70 sample under static condition test in synthetic oilfield water

Table 4.2 Fitted parameters and corrosion rates from static corrosion test

E_{corr} (mV) SCE	β_a (mV/decade)	β_c (mV/decade)	i_{corr} ($\mu A/cm^2$)	Corrosion Rate (mpy)
-755.5	40.8	-65.4	4.4	2.0

- **Under flow condition (FAC)**

Figure 4.6(a-e) exhibits the Tafel plots for API X70 steel electrodes, namely E1-E4 (Figure 4.6a), E5-E9 (Figure 4.6b), E10-E13 (Figure 4.6c), E14-E16 (Figure 4.6d), and E17-E20 (Figure 4.6e) obtained after FAC test in the loop system. It is analyzed from Tafel plots shown in Figure 4.6(a-e) that, all the samples are quite prone to the active dissolution of metal while electrolyte is flowing in the loop system and anodic Tafel plots of the entire electrodes exhibited a higher current density trend (Lopes-Sesenes et al. 2013) over static condition (Figure 4.5). Corrosion kinetics parameters such as corrosion potential (E_{corr}), Tafel slopes (β_a and β_c), corrosion current density (i_{corr}), and corrosion rates acquired from Tafel plots [Figure 4.6(a-e)] are listed in Table 4.3.

Corrosion current densities of the electrodes of column A [E1-E4, azimuthal angle ($\varphi = 135º$)] are noted about 252.9 $\mu A/cm^2$ [E1, polar angle ($\theta = 72º$)], 256.7 $\mu A/cm^2$ [E2, polar angle ($\theta = 54º$)], 259.6 $\mu A/cm^2$ [E3, polar angle ($\theta = 36º$)], and 261.4 $\mu A/cm^2$ [E4, polar angle ($\theta = 18º$)]. Corrosion current densities of the electrodes of column B [E5-E9, azimuthal angle ($\varphi = 180º$)] are observed about 248.6 $\mu A/cm^2$ [E5, polar angle ($\theta = 75º$)], 250.9 $\mu A/cm^2$ [E6, polar angle ($\theta = 60º$)], 253.3 $\mu A/cm^2$ [E7, polar angle ($\theta = 45º$)], 257.4 $\mu A/cm^2$ [E8, polar angle ($\theta = 30º$)], and 262.2 $\mu A/cm^2$ [E9, polar angle ($\theta = 15º$)]. Corrosion current densities of the electrodes of column C [E10-E13, azimuthal angle ($\varphi = 225º$)] are found about 253.5 $\mu A/cm^2$ [E10, polar angle ($\theta = 72º$)], 255.4 $\mu A/cm^2$ [E11, polar angle ($\theta = 54º$)], 257.8 $\mu A/cm^2$ [E12, polar angle ($\theta = 36º$)], and 260.2 $\mu A/cm^2$ [E13, polar angle ($\theta = 18º$)]. Corrosion current densities of the electrodes of column D [E14-E16, azimuthal angle ($\varphi = 315º$)] are noted about 283.6 $\mu A/cm^2$ [E14, polar angle ($\theta = 67.5º$)], 291.2 $\mu A/cm^2$ [E15, polar angle ($\theta = 45º$)], and 297.5 $\mu A/cm^2$ [E16, polar angle ($\theta = 22.5º$)]. Corrosion current density of the electrode E17 of column E [azimuthal angle ($\varphi = 0º$), polar angle ($\theta = 45º$)] is noted about 322.8 $\mu A/cm^2$. Corrosion current densities of the electrodes of column F [E18-E20, azimuthal angle ($\varphi = 45º$)] are found about 283.2 $\mu A/cm^2$ [E18, polar angle ($\theta = 67.5º$)], 290.8 $\mu A/cm^2$ [E19, polar angle ($\theta = 45º$)], and 298.5 $\mu A/cm^2$ [E20, polar angle ($\theta = 22.5º$)].

Similarly, corrosion rates of the electrodes of column A (E1, E2, E3, and E4) are noted about 467.6 mpy (E1), 474.5 mpy (E2), 479.9 mpy (E3), and 483.2 mpy (E4). However, corrosion rates of the electrodes of column B (E5, E6, E7, E8, and E9) are

found about 459.5 mpy (E5), 463.9 mpy (E6), 468.3 mpy (E7), 475.9 mpy (E8), and 484.7 mpy (E9). Similarly, corrosion rates of the electrodes of column C (E10, E11, E12, and E13) are observed about 468.7 mpy (E10), 472.2 mpy (E11), 476.6 mpy (E12), and 481.0 mpy (E13). Corrosion rates of the electrodes of column D (E14, E15, and E16) are found approximately 524.3 mpy (E14), 538.3 mpy (E15), and 550.1 mpy (E16). The corrosion rate of electrode E17 of column E is noted to be about 596.8 mpy. For column F, corrosion rates of the electrodes (E18, E19, and E20) are observed about 523.7 mpy (E18), 537.6 mpy (E19), and 552.0 mpy (E20).

From Table 4.3, it can be summarized that the corrosion current density and corrosion rate are increased onward the fluid flow path (Figure 3.2); however, corrosion potentials did not shift significantly. Moreover, the corrosion rates of the electrodes in column A are similar to that of column C. Similarly, the corrosion rates of the electrodes in column D, are quite similar to the used electrodes in column F. A careful examination of corrosion behavior of various electrodes shows that the corrosion rate reduces from intrados to extrados (El-Gammal et al. 2010; Poulson 1999). However, the corrosion rate is the highest at intrados electrode E17 at a polar angle (45º) and a fixed azimuthal angle (0º) and the lowest at extrados electrode E5 at a polar angle (75º) and a fixed azimuthal angle (180º). It can be deduced that the effect of flow is quite significant for the internal corrosion of pipeline steel as corrosion current density and corrosion rate under flow condition are adequately more than that under static condition (Jiang et al. 2005; Lopes-Sesenes et al. 2013; Vera et al. 2015).
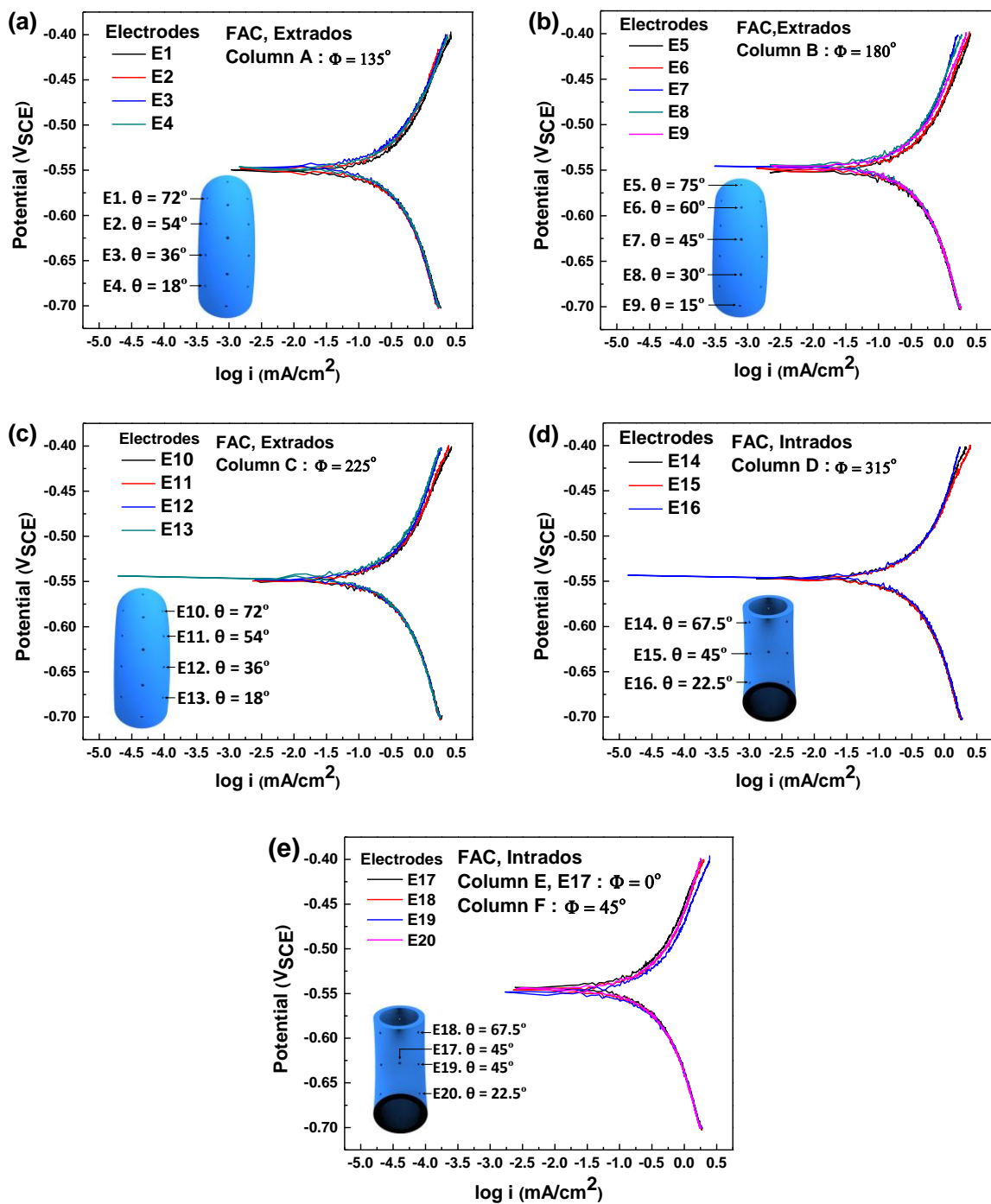
Figure 4.6 Tafel plots for the electrodes (a) E1-E4, (b) E5-E9, (c) E10-E13, (d) E14-E16, and (e) E17-E20 of FAC tests with velocity of 3 m s⁻¹ in synthetic oil field water

Table 4.3 Fitted parameters and corrosion rates for the Tafel plots of working electrodes from the FAC test

	Column, Azimuthal Angle (φ), Polar Angle (θ)	Electrode	Shear Stress (Pa)	E_{corr} (mV) SCE	β_a (mV/decade)	β_c (mV/decade)	i_{corr} (μA/cm^2)	Corr. Rate (mpy)
Extrados (Outer face)	A, 135º, 72º	E1	11.3	-548.2	124.5	-149.3	252.9	467.6
	A, 135º, 54º	E2	15.2	-547.9	137.7	-159.6	256.7	474.5
	A, 135º, 36º	E3	18.2	-544.5	137.9	-164.6	259.6	479.9
	A, 135º, 18º	E4	20.5	-543.2	133.3	-165.7	261.4	483.2
	B, 180º, 75º	E5	8.4	-547.8	117.8	-146.6	248.6	459.5
	B, 180º, 60º	E6	10.5	-542.7	111.8	-153.2	250.9	463.9
	B, 180º, 45º	E7	13.3	-544.4	144.6	-152.5	253.3	468.3
	B, 180º, 30º	E8	16.1	-539.5	142.3	-166.9	257.4	475.9
	B, 180º, 15º	E9	20.8	-543.5	137.1	-159.3	262.2	484.7
	C, 225º, 72º	E10	11.5	-547.3	123.7	-144.5	253.5	468.7
	C, 225º, 54º	E11	14.3	-544.3	121.5	-154.3	255.4	472.2
	C, 225º, 36º	E12	17.2	-546.5	138.7	-148.7	257.8	476.6
	C, 225º, 18º	E13	20.4	-545.2	148.9	-155.8	260.2	481.0
Intrados (Inner face)	D, 315º, 67.5º	E14	24.8	-550.8	160.7	-154.9	283.6	524.3
	D, 315º, 45º	E15	25.2	-545.8	148.3	-170.2	291.2	538.3
	D, 315º, 22.5º	E16	25.6	-546.2	159.6	-167.3	297.5	550.1
	E, 0º, 45º	E17	27.6	-543.0	189.1	-192.5	322.8	596.8
	F, 45º, 67.5º	E18	24.0	-550.4	166.8	-155.3	283.2	523.7
	F, 45º, 45º	E19	24.7	-543.8	134.8	-173.9	290.8	537.6
	F, 45º, 22.5º	E20	25.7	-542.3	158.8	-181.5	298.5	552.0

4.1.5 Electrochemical impedance spectroscopy (EIS) test

- **Under static condition**

Figure 4.7 shows the Nyquist plot of API X70 sample obtained by static EIS test in oilfield solution. The impedance parameters calculated by using an electrical equivalent circuit which is given in Figure 4.8 are tabulated in Table 4.4. The charge transfer resistance (R_{ct}) obtained after analyzing the impedance plot is about 1670 Ω cm^2. Alizadeh and Bordbar studied corrosion properties of X70 steel after 90 days immersion in a mixture of 0.5 M Na_2CO_3, 1 M $NaHCO_3$, and 0.1 M NaCl solutions by static EIS test. They have noticed that the charge transfer resistance (R_{ct}) is about 1067 Ω cm^2 (Alizadeh and Bordbar 2013). Sherif and Almajid also studied the corrosion and passivity behavior of X70 steel in static condition after its immersion for 24 h in 4.0 wt.% NaCl solution and it is found that the charge transfer resistance (R_{ct}) was about 2598 Ω cm^2 (Sherif and Almajid 2015).
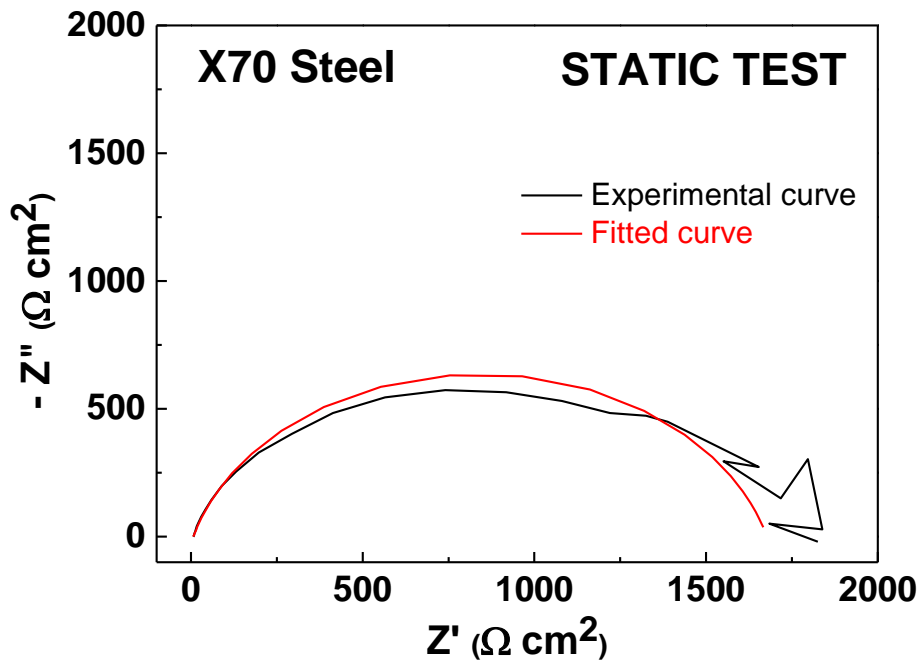
Figure 4.7 Nyquist plot of API X70 sample under static condition test
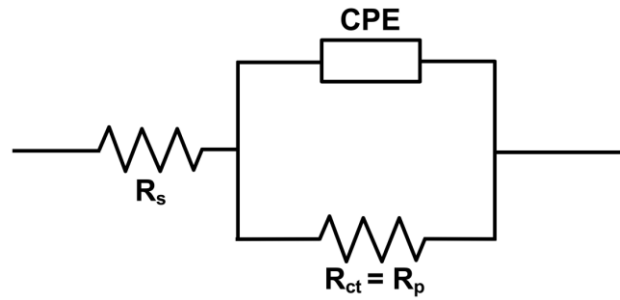
Figure 4.8 Equivalent circuit for EIS fitting for FAC study

Table 4.4 Fitted parameters and charge transfer resistance of static corrosion test

R_s (Ω cm^2)	Q_{CPE} (F. s^(a-1))	a	R_{ct} (Ω cm^2)
7.1	0.0002472	0.8	1670

- **Under flow condition (FAC)**

Figure 4.9(a-e) exhibits Nyquist plots for the electrodes E1-E4 (Figure 4.9a), E5-E9 (Figure 4.9b), E10-E13 (Figure 4.9c), E14-E16 (Figure 4.9d), and E17-E20 (Figure 4.9e) after FAC test in simulated oilfield water. The impedance spectra were analyzed using an electrical equivalent circuit according to Figure 4.8. Impedance kinetics parameters such as solution resistance (R_s), constant phase element (Q_{CPE}), and charge transfer resistance (R_{ct}) are listed in Table 4.5. The semi-circle radii of the capacitive loops responsible for the charge transfer resistances are much smaller for all the electrodes over the Nyquist plot obtained for the static condition (Lopes-Sesenes et al. 2013). Further, the charge transfer resistance (R_{ct}) of the extrados and intrados electrodes were decreased onward the fluid flow path due to an increment in the wall shear stress and flow velocity at all located angles [azimuthal angle (φ) and polar angle (θ)].

Charge transfer resistance (R_{ct}) of the electrodes of column A [E1-E4, azimuthal angle ($\varphi = 135º$)] are observed about 75.2 Ω cm^2 [E1, polar angle ($\theta = 72º$)], 74.2 Ω cm^2 [E2, polar angle ($\theta = 54º$)], 71.6 Ω cm^2 [E3, polar angle ($\theta = 36º$)], and 69.1 Ω cm^2 [E4, polar angle ($\theta = 18º$)]. However, charge transfer resistance (R_{ct}) of the electrodes of column B [E5-E9, azimuthal angle ($\varphi = 180º$)] are found about 76.1 Ω cm^2 [E5, polar angle ($\theta = 75º$)], 74.8 Ω cm^2 [E6, polar angle ($\theta = 60º$)], 74.3 Ω cm^2 [E7, polar angle (θ

= 45º)], 74.0 Ω cm^2 [E8, polar angle (θ = 30º)], and 71.8 Ω cm^2 [E9, polar angle (θ = 15º)]. Similarly, charge transfer resistance (R_{ct}) of the electrodes of column C [E10-E13, azimuthal angle (φ = 225º)] are observed about 83.7 Ω cm^2 [E10, polar angle (θ = 72º)], 75.5 Ω cm^2 [E11, polar angle (θ = 54º)], 75.6 Ω cm^2 [E12, polar angle (θ = 36º)], and 74.0 Ω cm^2 [E13, polar angle (θ = 18º)]. Charge transfer resistance (R_{ct}) of the electrodes of column D [E14-E16, azimuthal angle (φ = 315º)] are noted about 80.0 Ω cm^2 [E14, polar angle (θ = 67.5º)], 75.2 Ω cm^2 [E15, polar angle (θ = 45º)], and 70.5 Ω cm^2 [E16, polar angle (θ = 22.5º)]. Similarly, charge transfer resistance (R_{ct}) of the electrode E17 of column E [azimuthal angle (φ = 0º), polar angle (θ = 45º)] is found about 73.8 Ω cm^2. Similarly, charge transfer resistance (R_{ct}) of the electrodes of column F [E18-E20, azimuthal angle (φ = 45º)] are observed about 75.1 Ω cm^2 [E18, polar angle (θ = 67.5º)], 74.7 Ω cm^2 [E19, polar angle (θ = 45º)], and 73.9 Ω cm^2 [E20, polar angle (θ = 22.5º)].

Figure 4.9 Nyquist plots for the electrodes (a) E1-E4, (b) E5-E9, (c) E10-E13, (d) E14-E16, and (e) E17-E20 of FAC tests in synthetic oil field solution of fluid velocity 3 m s⁻¹

Table 4.5 Fitted parameters and charge transfer resistance for the Nyquist plots of electrodes from the FAC test

Column, Azimuthal Angle (φ), Polar Angle (θ)	Electrode	Shear Stress (Pa)	R_s (Ω cm^2)	Q_{CPE} (F. s^(a-1))	a	R_{ct} (Ω cm^2)
A, 135º, 72º	E1	11.3	9.6	0.0004810	0.6877	75.2
A, 135º, 54º	E2	15.2	9.1	0.0004050	0.7184	74.2
A, 135º, 36º	E3	18.2	11.1	0.0002304	0.7575	71.6
A, 135º, 18º	E4	20.5	11.4	0.0003991	0.7129	69.1
B, 180º, 75º	E5	8.4	10.0	0.0003347	0.7255	76.1
B, 180º, 60º	E6	10.5	7.9	0.0001911	0.7835	74.8
B, 180º, 45º	E7	13.3	10.8	0.0002275	0.7902	74.3
B, 180º, 30º	E8	16.1	11.9	0.0005228	0.6905	74.0
B, 180º, 15º	E9	20.8	12.7	0.0002532	0.7459	71.8
C, 225º, 72º	E10	11.5	8.0	0.0000850	0.8339	83.7
C, 225º, 54º	E11	14.3	9.0	0.0002067	0.7551	75.5
C, 225º, 36º	E12	17.2	10.1	0.0006575	0.6606	75.6
C, 225º, 18º	E13	20.4	12.1	0.0006244	0.6756	74.0
D, 315º, 67.5º	E14	24.8	7.8	0.0000926	0.8101	80.0
D, 315º, 45º	E15	25.2	8.6	0.0001818	0.7609	75.2
D, 315º, 22.5º	E16	25.6	10.4	0.0002376	0.7462	70.5
E, 0º, 45º	E17	27.6	9.5	0.0007521	0.6579	73.8
F, 45º, 67.5º	E18	24.0	8.6	0.0001571	0.7745	75.1
F, 45º, 45º	E19	24.7	8.8	0.0001771	0.7813	74.7
F, 45º, 22.5º	E20	25.7	11.3	0.0003937	0.7030	73.9

Rows A–C grouped under side label: **Extrados (Outer face)**
Rows D–F grouped under side label: **Intrados (Inner face)**

4.1.6 Analyses of corroded samples

- **Scanning electron microscopy (SEM) analysis of corroded samples**

SEM images for electrode number E7, E11, E14, and E17 were taken after FAC tests to examine surface morphologies of electrodes which are shown in Figure 4.10(a-d). It is obviously noticed that the electrodes (E7 and E11) at extrados have lower corrosion and its products over the electrodes (E14 and E17) at intrados and the corrosion current densities were found quite higher at E14 and E17.
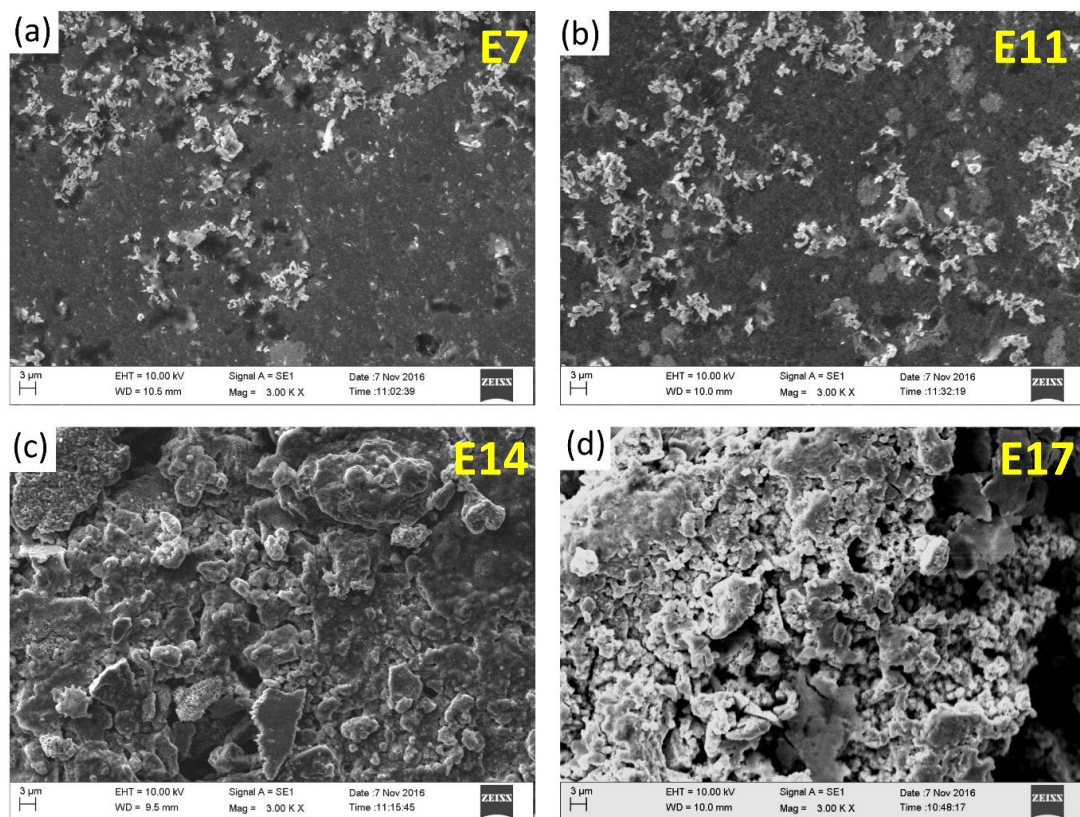
Figure 4.10 SEM micrographs of working electrodes after FAC experiment with flow velocity 3 m s^{-1} (a) E7, (b) E11, (c) E14, and (d) E17

- **Raman spectroscopy analysis of corrosion products**

The Raman spectrum of corrosion products formed on the selected electrode (E17) which has the highest corrosion after the FAC test is shown in Figure 4.11. The measured Raman band frequencies for the developed corrosion products at the specimen are given in Table 4.6. Data indicates that the compositions of corrosion compounds followed by FAC test are as $FeCO_3$ (1080.89 cm^{-1}), α-Fe_2O_3 (291.92 cm^{-1}),

γ-Fe$_2$O$_3$ (710.82 cm^{-1}), goethite α – FeOOH (299.85 cm^{-1}), and akageneite β – FeOOH (390.78, 490.84, 534.92, 605.20 cm^{-1}). It is noticed that the characteristic peak at 1080.89 cm^{-1} of FeCO$_3$ is quite strong as compared to other compounds formed for X70 steel in simulated oilfield solution. These products also inform that the possible corrosion products formed due to the reaction with carbonates and dominated reduction reaction (Guzonas et al. 1998; Kiosidou et al. 2017; Zhang et al. 2013).
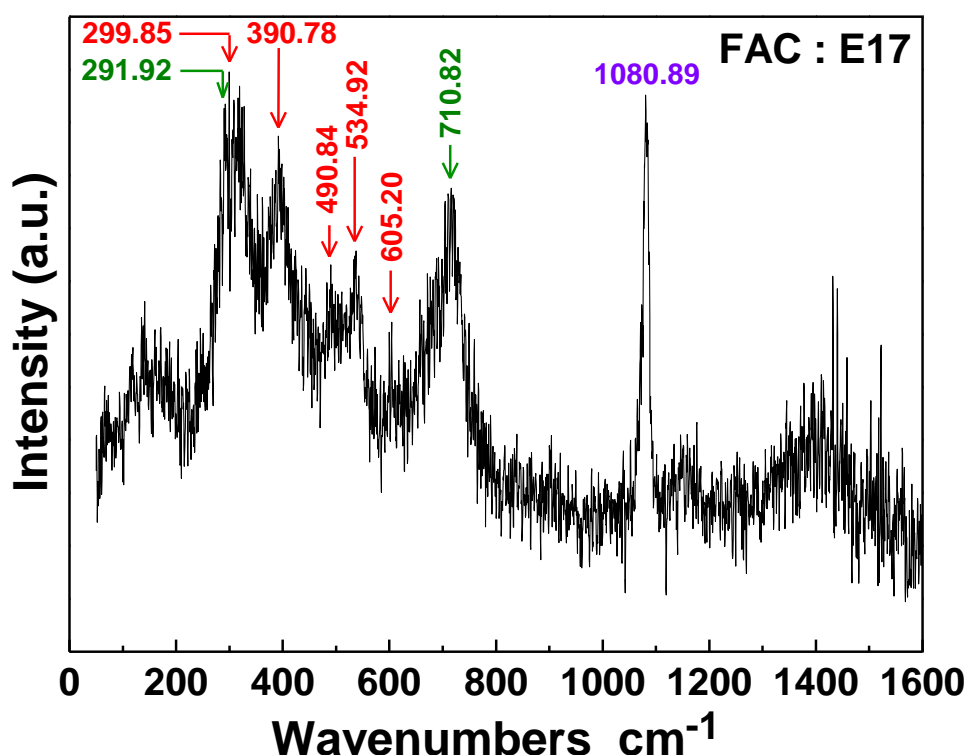
Figure 4.11 Raman spectrum of the electrode E17 followed by FAC test

Table 4.6 Measured Raman band frequencies for corrosion products of a representative electrode (E17) after FAC test (wavelength of 532 nm)

Raman bands (cm^{-1})	Phases Identified	References
1080.89	FeCO$_3$	(Zhang et al. 2013)
291.92	α-Fe$_2$O$_3$	(Zhang et al. 2013)
710.82	γ-Fe$_2$O$_3$	(Guzonas et al. 1998)
299.85	α – FeOOH	(Kiosidou et al. 2017)
390.78, 490.84, 534.92, 605.20	β – FeOOH	(Kiosidou et al. 2017)

70

4.1.7 Discussion

Comparative analysis of static and dynamic (FAC) electrochemical experimental results reveal that the X70 steel undergoes accelerated corrosion under flow condition than the static condition. Potentiodynamic polarisation analyses show that the corrosion rate under flow condition is about 250 times higher than that of static condition. Similarly, Nyquist plots of electrochemical impedance spectroscopy measurements disclose that the charge transfer resistance (R_{ct}) of the X70 steel samples under flow condition is about 22 times lower than that of static condition. During the continuous turbulent flow with high shear stress and velocity, a repeated depassivation (removal of the formed protective passive film) and repassivation (reformation of the protective passive film) occurs on the X70 steel samples. As a result of this process, the rate of highly reactive parent metal dissolution (corrosion) accelerates in the oilfield water environment (Hodgkiess et al. 1999; Wood 2009).

Potentiodynamic polarisation analyses indicate that the electrochemical corrosion activity of X70 steel is varied at various sites of the elbow in the flow condition. The corrosion rates obtained at the intrados and extrados of the elbow are 596.8 mpy (E17 - maximum) and 459.5 mpy (E5 - minimum) respectively. The shear stress is also maximum at E17 and minimum at E5. The shear stresses and corrosion rate were increased onward the fluid flow path. Corrosion rates at intrados electrodes are higher than that at extrados electrodes due to the higher shear stress at intrados (Efird et al. 1993; El-Gammal et al. 2010; Obanijesu 2009; Poulson 1999). It is observed that a 27.44% increment in the corrosion rate of innermost electrode E17 compared to the outermost electrode E7 located at the 90° elbow test section. The flow velocity of simulated oilfield water plays a vital role by providing a fresh electrolyte to the sample surface that has a large capacity to take in the soluble ions thereby increasing the corrosion rate with velocity (Kain 2014).

From the Tafel plots [Figure 4.6(a-e)], it is clear that API X70 steel electrodes are prone to active dissolution while the electrolyte is flowing in the loop system which can be attributed to the electrolyte flow that enhances the diffusion of iron species and increases the electrochemical reactivity (Kain et al. 2011). The electrochemical corrosion of carbon steel in chloride and carbonate-containing solutions are controlled

by possible anodic and cathodic reactions (Sun et al. 2016; Zhang et al. 2011b). The redox reactions of X70 steel in the simulated oilfield water can be expressed by the following equations (4.1-4.3):

Oxidation reaction (anodic dissolution of Fe ion)

$$Fe \rightarrow Fe^{2+} + 2e^- \qquad (E° = -0.440\ V_{SHE}) \qquad (4.1)$$

Reduction reaction (cathodic - oxygen reduction at neutral to alkaline solution)

$$O_2 + 2H_2O + 4e^- \rightarrow 4OH^- \qquad (E° = +0.401\ V_{SHE}) \qquad (4.2)$$

(Overall reaction) $\quad 2Fe + O_2 + 2H_2O \rightarrow 2Fe^{2+} + 4OH^- \qquad (4.3)$
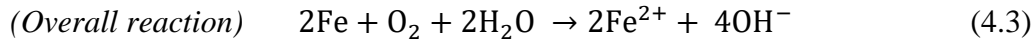
The available Fe^{2+} ion will react with OH^- and dissolved O_2 in the electrolyte after that as given in equations (4.4 and 4.5):

$$Fe^{2+} + 2OH^- \rightarrow Fe(OH)_2 \qquad\qquad (4.4)$$

$$4Fe(OH)_2 + O_2 + 2H_2O \rightarrow 4Fe(OH)_3 \qquad\qquad (4.5)$$
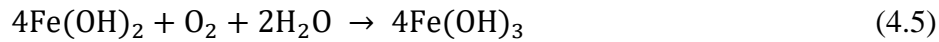
These products are unstable and converted into oxides as expressed in equation (4.6):

$$2Fe(OH)_3 \rightarrow Fe_2O_3 + 3H_2O \qquad\qquad (4.6)$$

However, apart from oxide products, α – FeOOH (goethite) and β – FeOOH (akageneite) are found as the key compositions of corrosion products from the Raman spectrum. Since the cathodic and anodic reactions occur at the meeting location of metal and electrolyte, FeOOH yields at the external surface of the metal. The corrosion mechanism in the presence of an aqueous medium can be expressed as in equation (4.7):

$$Fe(OH)_3 \rightarrow FeOOH + H_2O \qquad\qquad (4.7)$$

The mechanism of electrochemical reactions due to the presence of anion (Cl^-), accelerates the corrosion by promoting anodic dissolution that can be expressed as follows in equations (4.8 and 4.9):

$$Fe + 2Cl^- \rightarrow FeCl_2 + 2e^- \qquad\qquad (4.8)$$

$$4FeCl_2 + 8OH^- + O_2 \rightarrow 4FeOOH + 8Cl^- + 2H_2O \qquad\qquad (4.9)$$
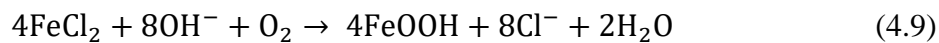
The precipitation of $FeCO_3$ is thermodynamically possible when the concentration of Fe^{2+} and CO_3^{2-} ions exceed the solubility product. Formation of the $FeCO_3$ film at the substrate by one-step reaction with carbonate, or two-steps reactions with bicarbonate, the following mechanisms can be used which are given in equations (4.10-4.13):

$$Fe \rightarrow Fe^{2+} + 2e^- \tag{4.10}$$

$$Fe^{2+} + CO_3^{2-} \rightarrow FeCO_3 \tag{4.11}$$

$$Fe^{2+} + 2HCO_3^- \rightarrow Fe(HCO_3)_2 \tag{4.12}$$

$$Fe(HCO_3)_2 \rightarrow FeCO_3 + CO_2 + H_2O \tag{4.13}$$
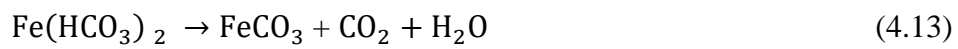
The FAC study reveals that the electrochemical corrosion kinetics parameters fluctuate corresponding to the position of the electrodes within the elbow. Transit of active groups (OH^-, dissolved O_2, Cl^- and CO_3^{2-}) to the electrode surface and also higher of cathodic kinetics would be intensified by the higher shear stress and flow velocity. This process leads to the higher dissolution rate of X70 steel samples located at the intrados of the pipe elbow. Furthermore, at the extrados, with lesser shear stress and fluid flow velocity, resulting in the lesser dissolution rate leads to a depressed cathodic reaction rate on the sample. This change is due to the counter rotating vortices and various scale eddies generated at the pipe elbow. At the region near the extrados, relatively lower fluid velocity and shear stress exist. It leads to the presence of a homogeneous flow field on the extrados (Wang et al. 2016).

Furthermore, Figure 4.9(a-e) shows that the Nyquist plots of electrochemical impedance spectroscopy measurements are defined by a single capacitive loop. The capacitive loop was responsible for the charge transfer process at the metal-electrolyte meeting location. The semicircle radii of the capacitive loops in the impedance spectra were decreased onward fluid flow path. Furthermore, the charge transfer resistance (R_{ct}) was lower on the intrados due to the higher shear stress and velocity compared to the extrados. It is found that less than 1% lower charge transfer resistance (R_{ct}) of innermost electrode E17 as compared to the outermost electrode E7 located at the 90º elbow test section.

Figure 4.12(a-e) shows the variations of shear stress, charge transfer resistance (R_{ct}), and corrosion current density (i_{corr}) of working electrodes onwards the flow path at various azimuthal angles (φ) of the 90° elbow test section after FAC test. It also reveals that when shear stress decreases, corrosion current density also decreases. However, the charge transfer resistances were increased with a reduction in shear stresses. To notice electrodes E8 (column B) and E11 (column C), small variations were also noticed due to the counter rotating vortices and various scale eddies formation by turbulent fluid flow (Wang et al. 2016).
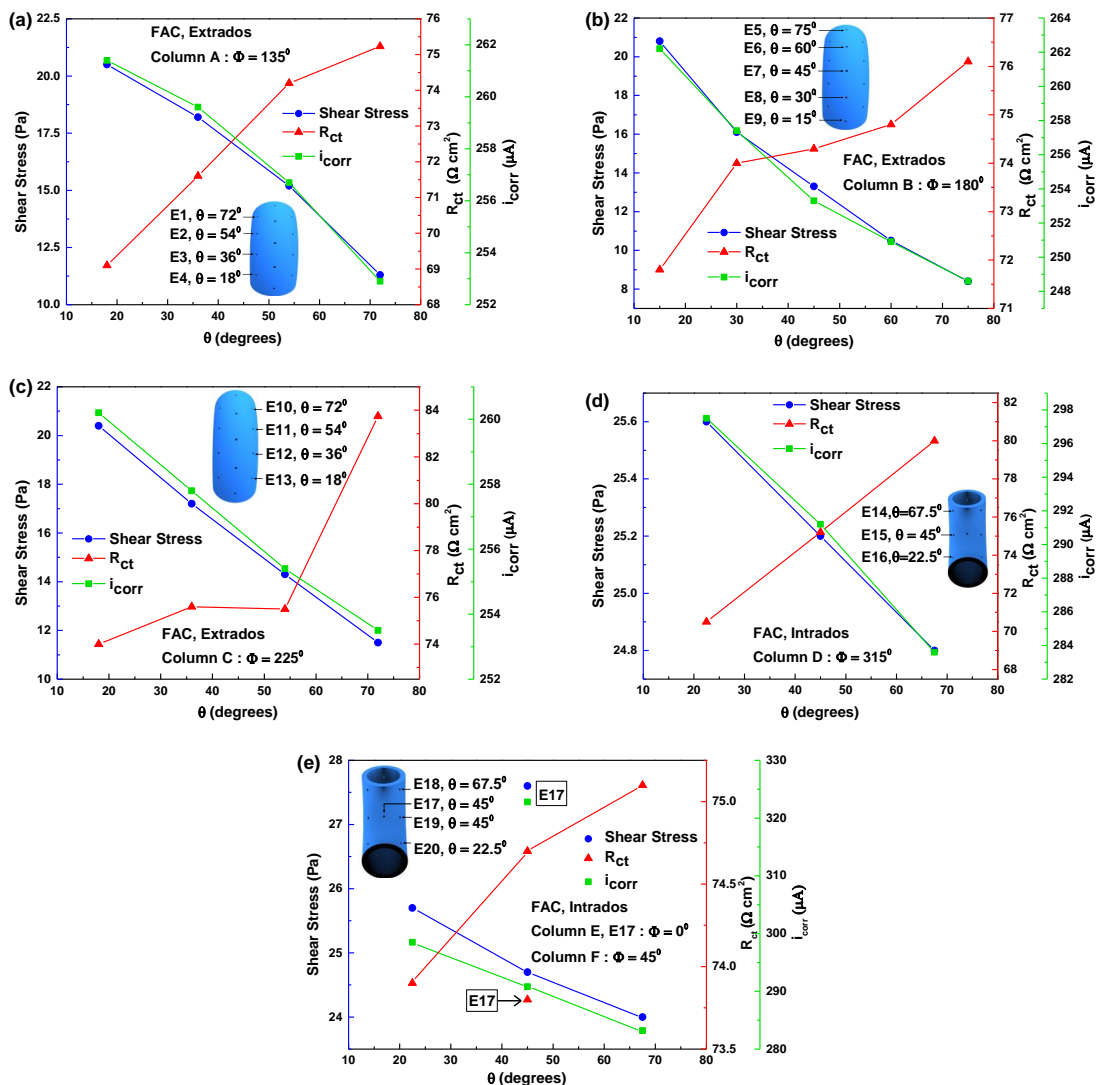
Figure 4.12 Fluctuations of shear stress, charge transfer resistance (Rct), and corrosion current density (i_{corr}) of working electrodes onwards the fluid flow path at

various azimuthal angles φ of the elbow (a) φ = 135°, (b) φ = 180°, (c) φ = 225°, (d)
φ = 315°, and (e) φ = 0°, φ = 45° after FAC experiments

The SEM micrographs [Figure 4.10(a-d)] of the exposed specimens demonstrate that both the intrados (E14 and E17) and extrados (E7 and E11) electrodes have irregular and loose corrosion products. Raman spectroscopy results (Figure 4.11, Table 4.6) reveals that a large proportion of $FeCO_3$ was formed over oxides as a corrosion product. The Raman spectrum also indicates that a small fraction of other compounds formed by FAC test as α-Fe_2O_3, γ-Fe_2O_3, α – FeOOH, and β – FeOOH. Compared to the extrados electrodes the intrados electrodes have more disconnected corrosion compounds and a higher corrosion rate. Among these four electrodes, electrode E17 is having a more loose and porous structured corrosion product because of higher shear stress and fluid flow velocity at the intrados compared to extrados. These irregular and porous corrosion compounds cannot protect the substrate from further corrosion degradation in the used simulated solution.

The computational fluid dynamics (CFD) simulation demonstrates that there are distinct shear stress *(see Table 4.3)* and fluid flow velocities at various parts of the elbow test section as a result of the geometrical diversity. The minimum wall shear stress 8.4 Pa is simulated at extrados for the electrode E5 with a polar angle (75°) and azimuthal angle (180°). The maximum wall shear stress 27.6 Pa is simulated at intrados for the electrode E17 of polar angle (45°) and azimuthal angle (0°). At this inner wall region of the elbow, flow accelerates due to the effect of elbow curvature within the boundary layer and results in a high-velocity gradient, indicating the wall shear stress is significantly higher. The high shear stress resulting from high flow velocity and turbulence decreases the boundary layer thickness causing an increase in corrosion rate thus increasing the FAC rate (El-Gammal et al. 2010; Kain 2014; Kain et al. 2011; Lin and Ferng 2014). The highest rate of corrosion present at the intrados electrode of the 90° pipe elbow where the shear stress and flow velocity is maximum. The corrosion rate is increased onward the fluid flow path and from the extrados to the intrados, with the same variation in shear stress and fluid velocity. This is in agreement with the outcomes of other researchers (Zhang et al. 2013). CFD simulation results and experimental results are demonstrated that fluid flow parameters played a crucial role in the FAC of X70 steel. It is mainly related to the high wall shear stress under high

flow velocity conditions. Because of the geometrical structure and alignment of the elbow, the metal dissolution rate is more at the intrados than at the extrados (Zhang et al. 2013). Therefore the comparative study of electrochemical analyses with CFD simulation demonstrates that the higher corrosion rate is associated with high shear stress and fluid flow velocity at the 90º pipe elbow.

4.1.8 Summary

The effect of hydrodynamic parameters such as flow velocity and shear stress on API X70 steel was studied in the static and dynamic corrosive environment. A loop system was utilized to imitate the flow through a pipe more realistically. Hydrodynamic parameters (obtained from CFD simulation) especially shear stress, and flow velocity of the fluid flow played a vital role in flow accelerated corrosion (FAC), and the major findings are given below.

- FAC of API X70 steel depends on hydrodynamic parameters of the fluid flow such as wall shear stress and flow velocity.

- It is observed that, within the elbow, corrosion rate and corrosion current density at the intrados (inner face) are more as compared to the extrados (outer face). However, onward the flow path corrosion rate is increased.

- The maximum and minimum corrosion rates observed are 596.8 mpy (intrados electrode E17) and 459.5 mpy (extrados electrode E5), respectively.

- High corrosion current density and corrosion rate are due to the turbulent flow with higher shear stress and flow velocity particularly in the intrados of the 90º pipe elbow.

- The experimental results are in agreement with the CFD simulation results.

4.2 Effect of oleic acid hydrazide (OAH) inhibitor on FAC of API X70 steel

Oleic acid hydrazide (OAH), an organic compound, is a promising environment-friendly, green inhibitor which can be used to protect low alloy steels against corrosion (Quaraishi et al. 2000; Quraishi and Ansari 2003). The influence of OAH inhibitor at various concentrations (0.05 g/L, 0.15 g/L, 0.30 g/L) on API X70 steel was studied in the simulated oilfield water in the flow loop system. For the flow accelerated corrosion (FAC) tests, twenty X70 steel samples were placed at various locations of the 90º elbow test section. The electrochemical impedance spectroscopy technique was utilized to analyze the efficiency of the OAH inhibitor. The corroded surface morphologies and corrosion products were analyzed with the help of SEM and Raman spectroscopy techniques. FTIR and XPS analyses were conducted to understand the interaction of inhibitor molecules with the sample surface in simulated solution.

4.2.1 Polarization resistance and inhibition efficiency

Electrochemical impedance spectroscopy (EIS) technique was utilized to find out the polarization resistance and inhibition efficiency of X70 steel at different concentrations of OAH inhibitor (0.05 g/L, 0.15 g/L, 0.30 g/L) in the circulating simulated oilfield water at a flow velocity of 3 m s^{-1}. The impedance spectra were examined using the electrical equivalent circuits given in Figure 4.13(a, b). Here, the impedance parameters, such as R_s, CPE, R_{ct}, R_p, and R_f, are solution resistance, constant phase element, charge transfer resistance, polarization resistance, and film resistance respectively. Figure 4.14(a-f) exhibits Nyquist plots for electrodes E2 (Figure 4.14a), E4 (Figure 4.14b), E7 (Figure 4.14c), E10 (Figure 4.14d), E17 (Figure 4.14e), and E19 (Figure 4.14f). The inhibition efficiency of the OAH inhibitor was computed with the help of polarization resistances using equation 4.14, where R_p and R_p^0 are the polarization resistance in the presence and absence of inhibitor, respectively.

$$\eta\% = \frac{R_p - R_p^0}{R_p} \times 100 \qquad (4.14)$$
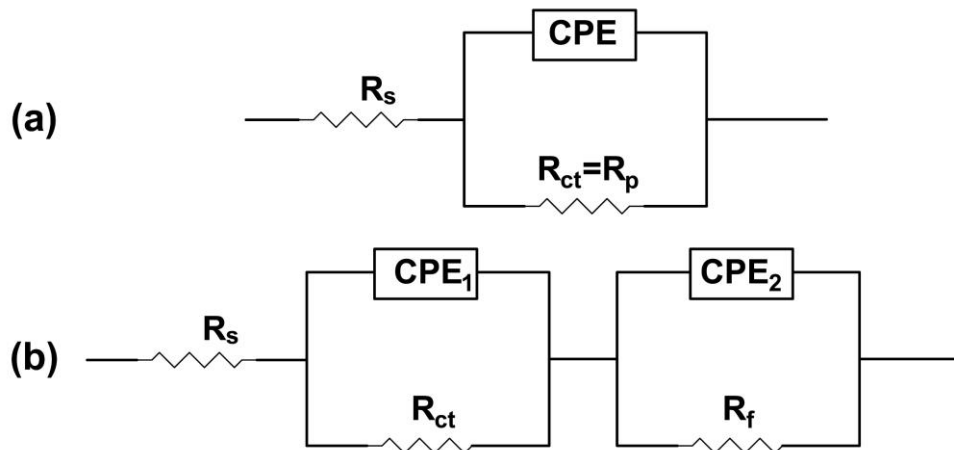
Figure 4.13 Electrochemical equivalent circuits for EIS fitting for the EIS measurements in FAC condition for (a) without inhibitor solution (b) with OAH inhibitor solution

The polarization resistances (R_p) and inhibition efficiencies ($\eta\%$) are tabulated in Table 4.7. It is seen that the polarization resistances and inhibition efficiencies were varying concerning the positions of the electrodes at the elbow test section. The polarization resistances (R_p) in the absence of the inhibitor are significantly less than those in the presence of the inhibitor. The enlargement of capacitive loop radii (is shown in Nyquist plots) and increase of calculated R_p values when the concentration of the inhibitor increases are attributed to the adsorbed inhibitor molecule, which directly influences the resistance of the metal dissolution reactions (Du et al. 2009; Neville and Wang 2009; Zeng et al. 2015).
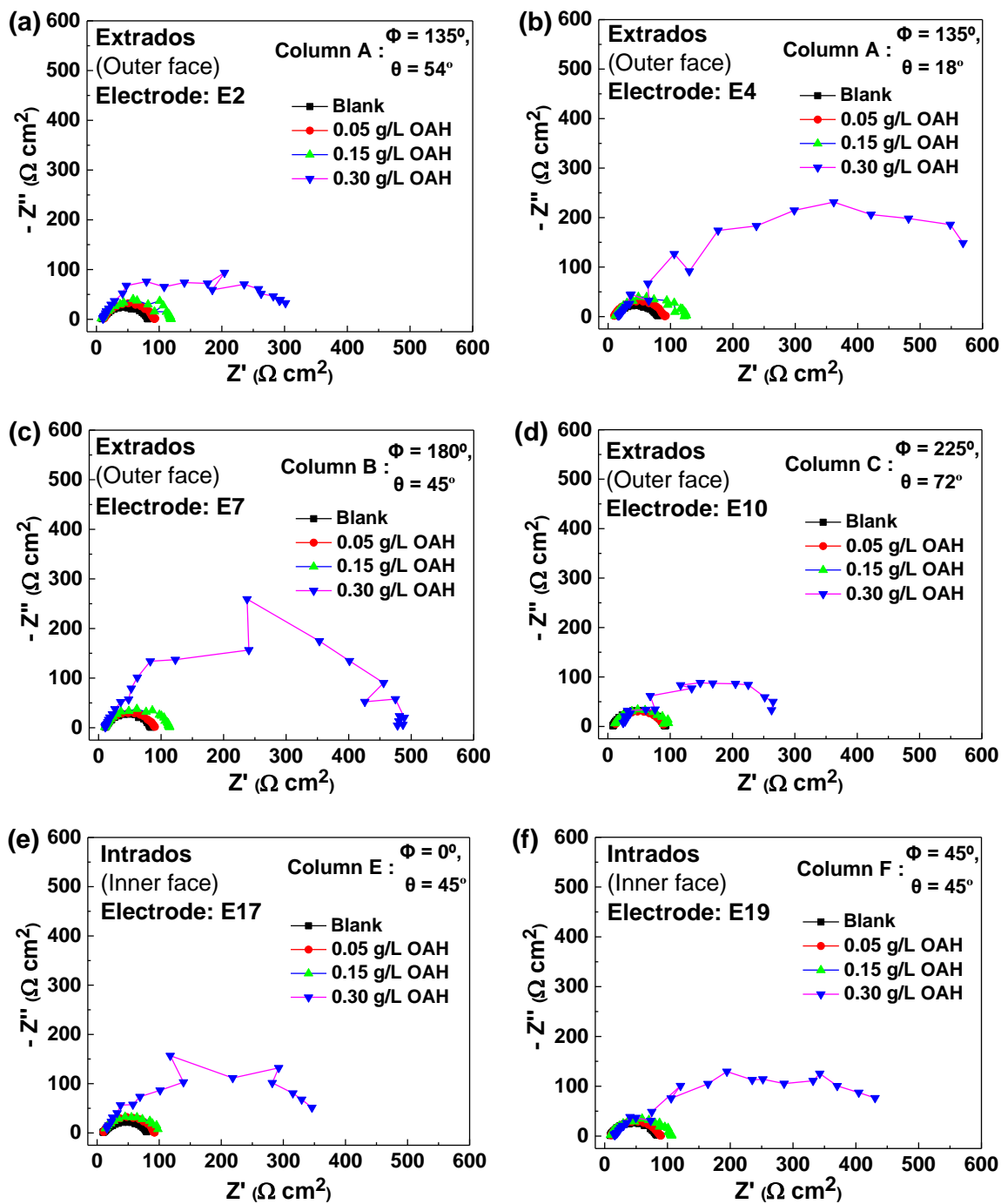
Figure 4.14 Nyquist plots for the electrodes (a) E2, (b) E4, (c) E7, (d) E10, (e) E17, and (f) E19 with and without OAH inhibitor FAC test

Table 4.7 Polarization resistances (R_p) and Inhibition efficiencies (η%) obtained from impedance (FAC) study with OAH inhibitor

Column, Azimuthal Angle (φ), Polar Angle (θ)	Electrode	R_p (Ω cm²)				η%		
		0	0.05	0.15	0.30	0.05	0.15	0.30
		g/L (OAH Inhibitor)				g/L (OAH Inhibitor)		
Extrados (Outer face)								
A, 135°, 72°	E1	75.2	92.4	131.3	311.0	18.6	42.7	75.8
A, 135°, 54°	E2	74.2	92.0	125.1	321.9	19.3	40.7	76.9
A, 135°, 36°	E3	71.6	92.0	118.2	377.7	22.2	39.4	81.0
A, 135°, 18°	E4	69.1	90.3	109.5	560.8	23.5	36.9	87.7
B, 180°, 75°	E5	76.1	93.7	116.3	343.7	18.8	34.6	77.9
B, 180°, 60°	E6	74.8	90.9	114.7	399.1	17.7	34.8	81.3
B, 180°, 45°	E7	74.3	90.0	111.0	411.8	17.4	33.1	82.0
B, 180°, 30°	E8	74.0	89.9	109.8	386.0	17.7	32.6	80.8
B, 180°, 15°	E9	71.8	88.1	99.0	317.3	18.5	27.5	77.4
C, 225°, 72°	E10	83.7	92.0	111.3	290.2	9.0	24.8	71.2
C, 225°, 54°	E11	75.5	91.7	107.2	377.6	17.7	29.6	80.0
C, 225°, 36°	E12	75.6	90.3	103.6	497.2	16.3	27.0	84.8
C, 225°, 18°	E13	74.0	89.7	98.5	429.1	17.5	24.9	82.8
Intrados (Inner face)								
D, 315°, 67.5°	E14	80.0	91.9	114.5	295.9	12.9	30.1	73.0
D, 315°, 45°	E15	75.2	90.7	109.7	315.6	17.1	31.4	76.2
D, 315°, 22.5°	E16	70.5	88.5	105.6	475.8	20.3	33.2	85.2
E, 0°, 45°	E17	73.8	91.8	103.0	381.1	19.6	28.3	80.6
F, 45°, 67.5°	E18	75.1	89.3	113.9	428.9	15.9	34.1	82.5
F, 45°, 45°	E19	74.7	88.3	110.9	534.9	18.6	42.7	75.8
F, 45°, 22.5°	E20	73.9	88.3	106.8	308.8	19.3	40.7	76.9

4.2.2 Analyses of corroded samples

- **Scanning electron microscopy (SEM) analysis of corroded samples**

Figure 4.15(a, b) displays the SEM surface morphologies of API X70 electrodes after corrosion tests under flow condition. In the absence of the inhibitor (Figure 4.15a), more porous corrosion compounds were noticed on the electrode surface. However, the corrosion products formed during FAC test with the presence of inhibitor (Figure 4.15b) have found good protection against corrosion of substrate as compared to the corrosion products formed without inhibitor. Furthermore, the electrodes were covered by some corrosion products in both blank and inhibited solutions, due to the effect of hydrodynamic parameters such as velocity and shear stress.
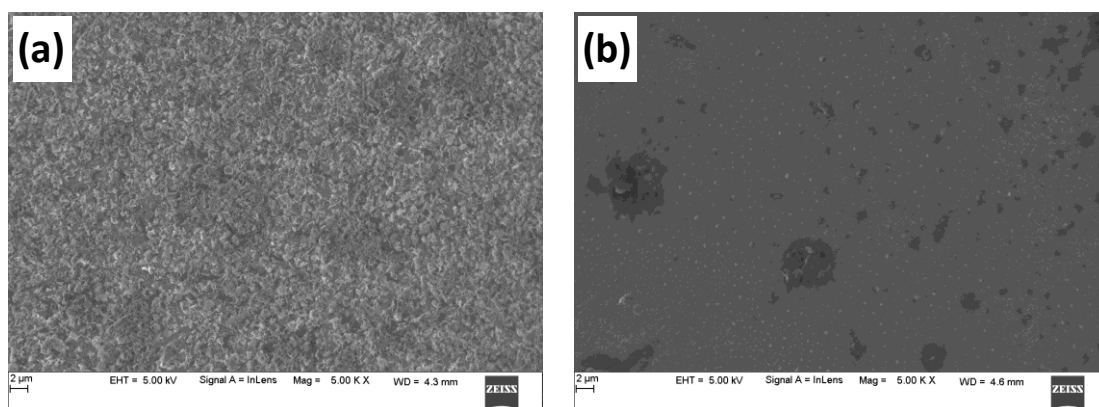
Figure 4.15 SEM micrographs of electrode E17 after FAC tests (a) without inhibitor, and (b) with 0.30 g/L OAH inhibitor

- **Raman spectroscopy analysis of corrosion products**

Figure 4.16(a-c) shows the Raman spectra of samples after the FAC test with various concentrations (0.05 g/L, 0.15 g/L, 0.30 g/L) of OAH inhibitor. Table 4.8 represents the measured Raman band frequencies and corrosion products formed on the surface of electrode E17. It is indicating that the compositions of corrosion compounds obtained after the FAC test in the presence of OAH inhibitor are α-Fe_2O_3 (hematite), γ-Fe_2O_3 (maghemite), γ-FeOOH (lepidocrocite), and β – FeOOH (akageneite). Furthermore, the main constituent of the corrosion product is Fe_2O_3. From Raman spectra, it is observed that a small fraction of corrosion products were formed after FAC tests in the presence of the OAH inhibitor as compared to the absence of inhibitor. It is also interesting to

find that the major constituent $FeCO_3$ compound in the absence of inhibitor got changed with only oxides.
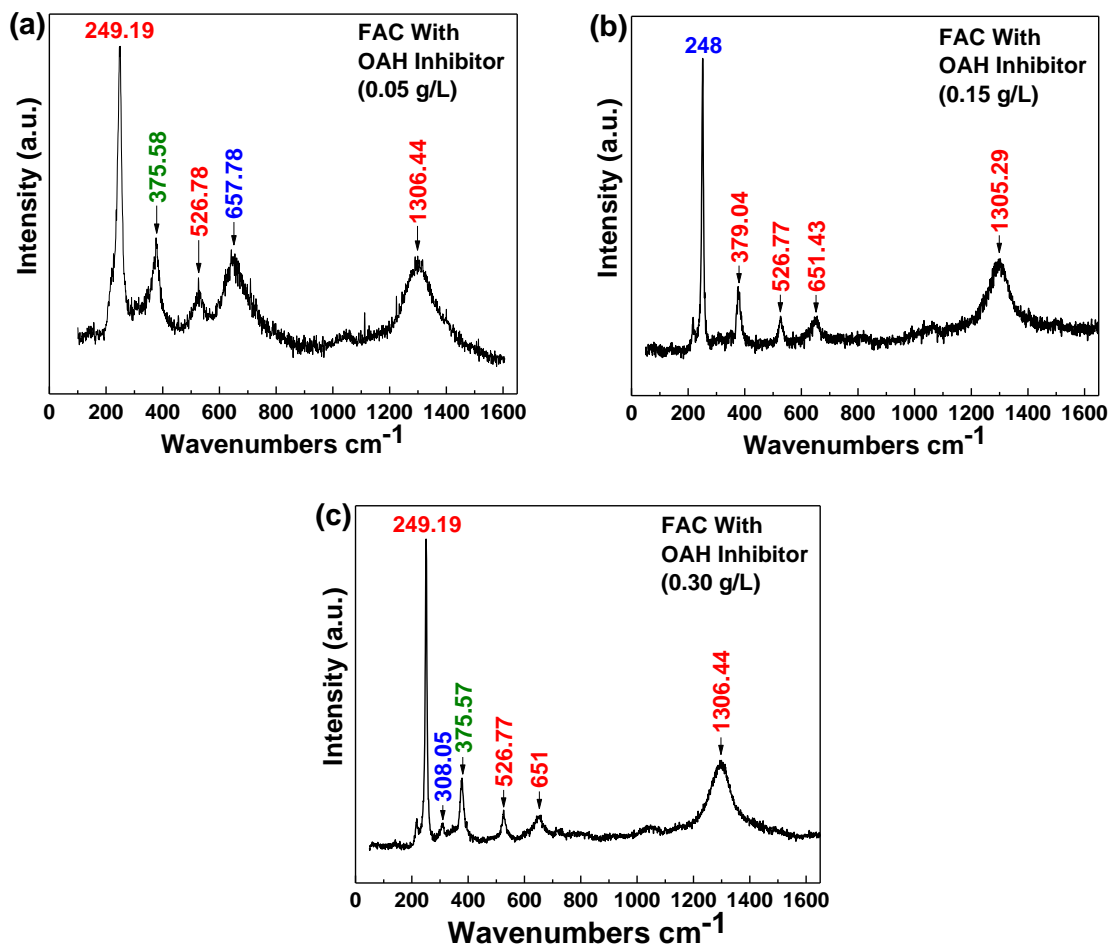
Figure 4.16 Raman spectra of the electrode - E17 after FAC test at 3 m s^{-1} velocity in OAH inhibited solution (a) 0.05 g/L, (b) 0.15 g/L, (c) 0.30 g/L

Table 4.8 Measured Raman band frequencies for corrosion products of the electrode - E17 after FAC test with OAH inhibitor (wavelength - 532 nm)

OAH Inhibitor (g/L)	Raman bands (cm^{-1})	Phases Identified	References
	249.19, 526.78, 1306.44	γ-FeOOH	(Kiosidou et al. 2017)
0.05	657.78	α-Fe$_2$O$_3$	(Guzonas et al. 1998)
	375.58	γ-Fe$_2$O$_3$	(Guzonas et al. 1998)
0.15	379.04, 526.77, 651.43, 1305.29	γ-FeOOH	(Kiosidou et al. 2017)
	248	β-FeOOH	(Guzonas et al. 1998)
	249.19, 526.77, 651, 1306.44	γ-FeOOH	(Kiosidou et al. 2017)
0.30	375.57	γ-Fe$_2$O$_3$	(Guzonas et al. 1998)
	308.05	β-FeOOH	(Kiosidou et al. 2017)

- **FTIR-ATR analysis for inhibitor study**

Fourier transform infrared spectroscopy – attenuated total reflectance (FTIR–ATR) spectra were recorded in the range 4000–500 cm^{-1} to investigate the possible interaction of the OAH inhibitor molecule with the X70 steel surface. FTIR characterization of the OAH was carried out to determine the functional groups that exist in it, while that of the corrosion compounds is to confirm that the inhibition takes place due to the connection between the specimen and the OAH inhibitor. Figure 4.17 shows the FTIR spectra of pure OAH and corrosion compounds obtained after the FAC test with 0.30 g/L OAH inhibitor. The assignment of vibration type and functional groups are presented in Table 4.9. In the spectrum of pure OAH, the peaks at 2922.16 cm^{-1} and 2852.72 cm^{-1} are corresponding to the stretching vibration of the $C-H$ bond. The peaks at 3318.90 cm^{-1} and 1627.92 cm^{-1} are corresponding to the stretching and bending vibration of the $N-H$ bond, respectively. The peaks at 1462.04 cm^{-1}, 1372.57 cm^{-1}, and 723.3 cm^{-1} are corresponding to the $C-H$ bending vibration. The presence of one strong peak at 1737.83 cm^{-1} is corresponding to the $C=O$ stretching vibration (Bruice 2014; Mistry 2009; Zhang et al. 2011a). FTIR of the pure OAH inhibitor showed the presence of oxygen and nitrogen atoms in functional groups $(N-H)$ and $(C=O)$.

The general characteristics of typical corrosion inhibitors are met by the oxygen and nitrogen atoms present in the OAH inhibitor (Alaneme et al. 2016).
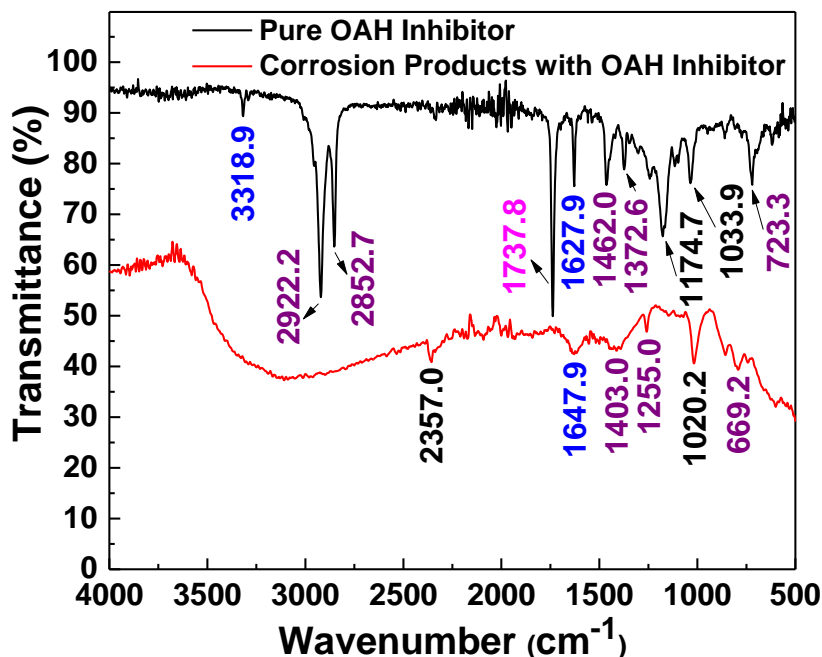
Figure 4.17 FTIR spectra of corrosion products on electrode 17 after FAC test with 0.30 g/L OAH inhibitor and pure OAH Inhibitor

In the FTIR spectrum of the corrosion product of API X70 steel after FAC test, it was found that the $C - H$ bending at 1462.04 cm^{-1}, 1372.57 cm^{-1}, and 723.3 cm^{-1} were shifted to 1402.96 cm^{-1}, 1254.97 cm^{-1}, and 669.18 cm^{-1}, the $N - H$ bending of 1627.92 cm^{-1} is also shifted to 1647.88 cm^{-1}. These shifts in the FTIR spectrum of corrosion products of inhibited X70 steel samples compared to the pure OAH inhibitor is directly attributed to the interaction of inhibitor molecules with steel substrate which resulted in inhibition. The following frequencies of vibration were disappeared in the FTIR spectrum of corrosion product of API X70 steel after the FAC test: $C - H$ stretching vibration at 2922.16 cm^{-1} and 2852.72 cm^{-1}, the $N - H$ stretching vibration at 3318.90 cm^{-1} and the $C = O$ stretching vibration at 1737.83 cm^{-1}. This result shows that the OAH inhibitor was adsorbed on the metal surface to form (Fe-Inh)$^{2+}$ complex (Alaneme et al. 2016; Ameh et al. 2017).

Table 4.9 FTIR band frequencies and the functional group assigned for pure OAH and corrosion products of electrodes after FAC test with OAH inhibitor (0.30 g/L)

Wavenumber (cm⁻¹) [Pure OAH Inhibitor]	Wavenumber (cm⁻¹) [Corrosion products with OAH Inhibitor]	Functional Group	Vibration Mode	References
2922.2	-	$C-H$	Stretching	
2852.7	-	$C-H$	Stretching	
1737.8	-	$C=O$	Stretching	
3318.9	-	$N-H$	Stretching	(Bruice 2014; Mistry 2009; Zhang et al. 2011a)
1627.9	1647.9	$N-H$	Bending	
1462.0	1403.0	$C-H$	Bending	
1372.6	1255.0	$C-H$	Bending	
723.3	669.2	$C-H$	Bending	

- **X-ray photoelectron spectroscopy (XPS) analysis for inhibitor study**

XPS survey spectrum of the surface of electrode E17 after the FAC test with 0.30 g/L OAH inhibitor is shown in Figure 4.18. It exhibits evidence of the elements such as C, O, Fe, Ca, N, Na, Mg, and Mn. The nitrogen (N) in the corrosion product clearly confirms the presence of fatty-acid derivative inhibitor film on the exposed electrode surface. Figure 4.19(a-d) shows the high-resolution XPS spectra with the binding energy of elements such as C, N, O, and Fe. The information about the ionic state of elements and compounds formation was obtained by peak fitting. The binding energies and peak assignments are tabulated in Table 4.10. To examine the XPS plots, indicating a clear the presence of OAH inhibitor on the corroded sample.
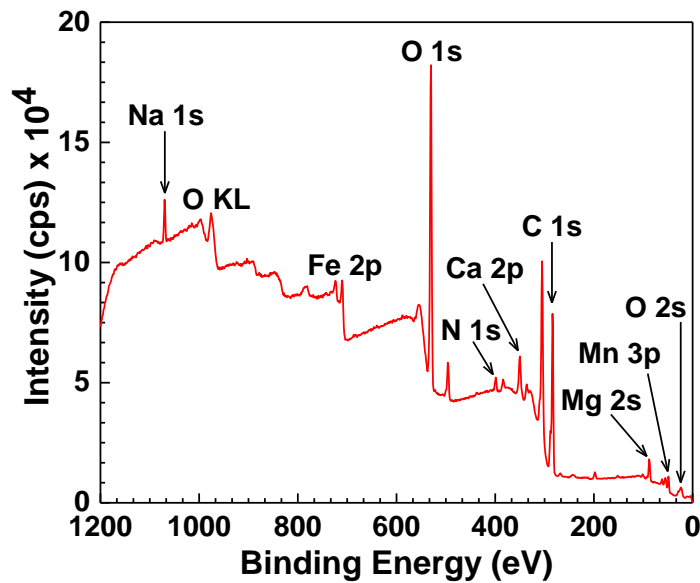
Figure 4.18 XPS survey spectrum for the surface products on electrode E17 after FAC test with 0.30 g/L OAH
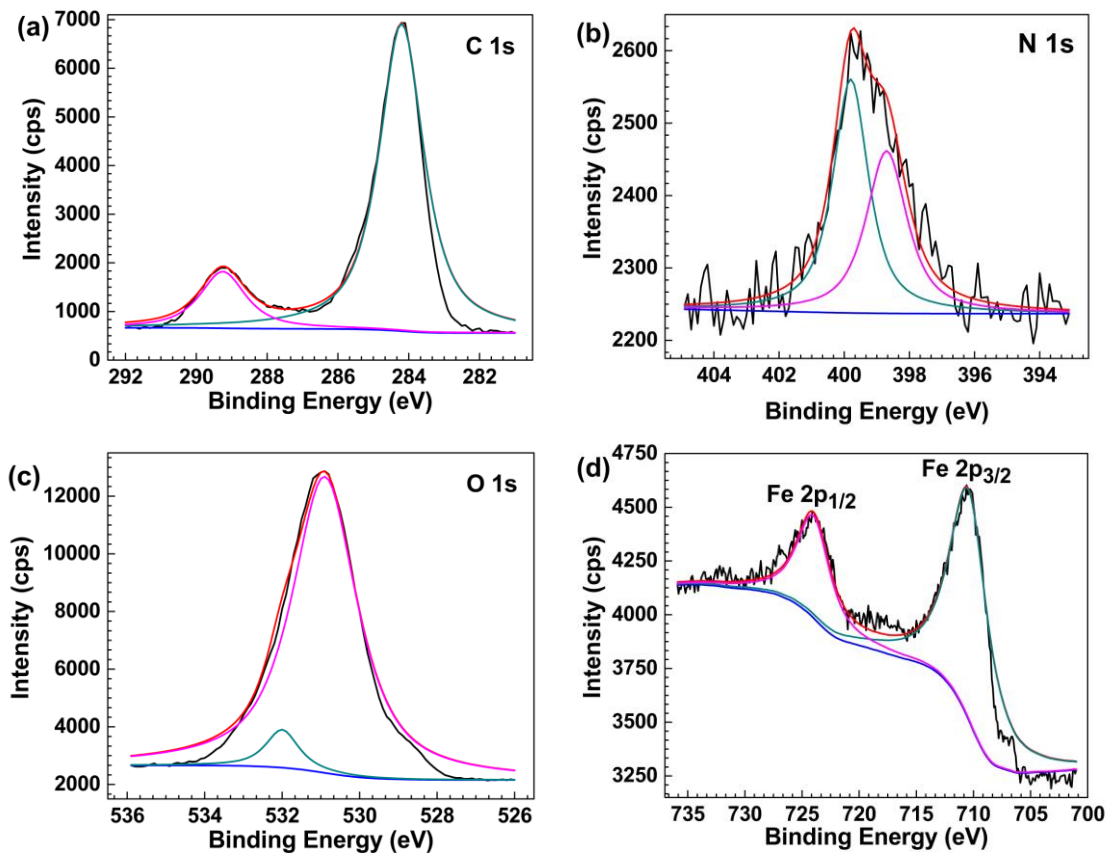
Figure 4.19 High resolution XPS spectra of electrode 17 after FAC test with 0.30 g/L OAH inhibitor: (a) C 1s, (b) N 1s, (c) O 1s, and (d) Fe $2p_{3/2}$ and Fe $2p_{1/2}$

Table 4.10 XPS spectral analysis for the surface products formed on API 5L X70 steel after FAC test in the presence of 0.30 g/L OAH inhibitor

Elements	Valence state	Binding Energy (eV)	Possible assignment for peaks	References
C	1s	284.2	Adventitious/ $C-H$, $C-N$	(Zeng et al. 2015)
		289.1	$C=O$	(Liu et al. 2015)
N	1s	398.7	$C-N$	(Zeng et al. 2015)
		399.8	NH, NH_2	(Zeng et al. 2015)
O	1s	530.6	Fe_2O_3, FeOOH	(Guo et al. 2016; Zhao and Chen 2012)
		531.0	Fe_2O_3, FeOOH	(Guo et al. 2016; Zhao and Chen 2012)
		532.3	Organic O	(Liu et al. 2015; Usman et al. 2017)
Fe	2p$_{3/2}$	711.2	Fe_2O_3, FeOOH	(Guo et al. 2016; Zhou et al. 2017)
	2p$_{1/2}$	724.3	Fe_2O_3, FeOOH	(Guo et al. 2016; Nam et al. 2014)

4.2.3 Discussion

The polarization resistances (R_p) of FAC study with OAH inhibitor indicate that it protects the X70 steel at 0.30 g/L. However, the distribution of inhibition efficiencies (Figure 4.20) measured by the EIS method reveals that inhibition efficiencies at 0.05 g/L, 0.15 g/L, and 0.30 g/L OAH vary corresponding to the position of the electrodes within the elbow test section under FAC condition. This is due to variations in hydrodynamic parameters such as wall shear stress and velocity at the various locations of the elbow test section. Also, the secondary flow and flow separation effect, which directly leads to the generation of counter rotating vortices, and various scale eddies at the elbow will control the flow pattern and promote the mass transfer process of anions near the pipe wall (El-Gammal et al. 2010; Wang et al. 2016; Zeng et al. 2016b). The CFD simulation results discussed in the previous section also indicated that the shear stress and velocity are different at various locations of the elbow test section. The inhibition efficiencies of OAH for FAC tests are increasing from low (0.05 g/L) to high (0.30 g/L) concentration. When the inhibitor concentration is more, the surface

coverage or adsorption of inhibitor molecules on the active sites of the electrode increases, and then more active sites are blocked, as shown in Figure 4.21(a-c). Therefore, inhibition efficiency increases from lower to higher concentrations of OAH (Zeng et al. 2017).
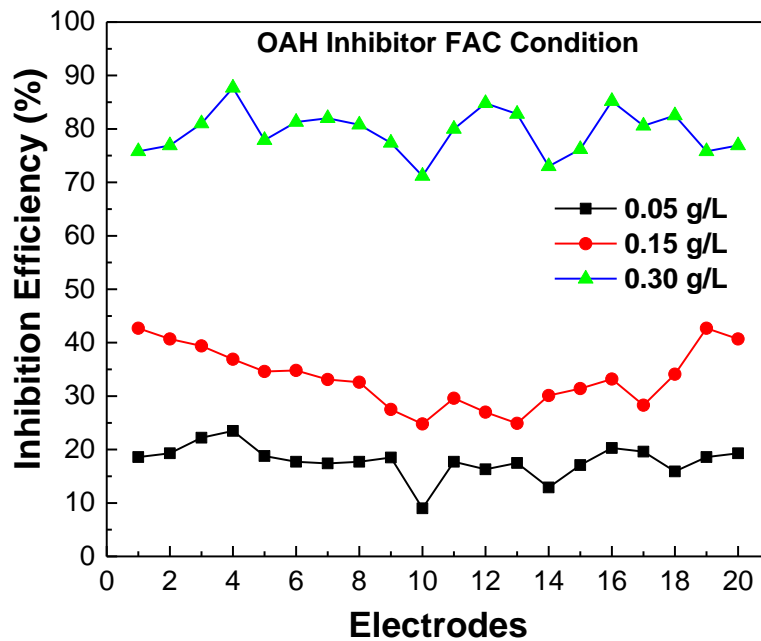
Figure 4.20 Distribution of inhibition efficiencies of OAH inhibitor in FAC condition for all twenty electrodes
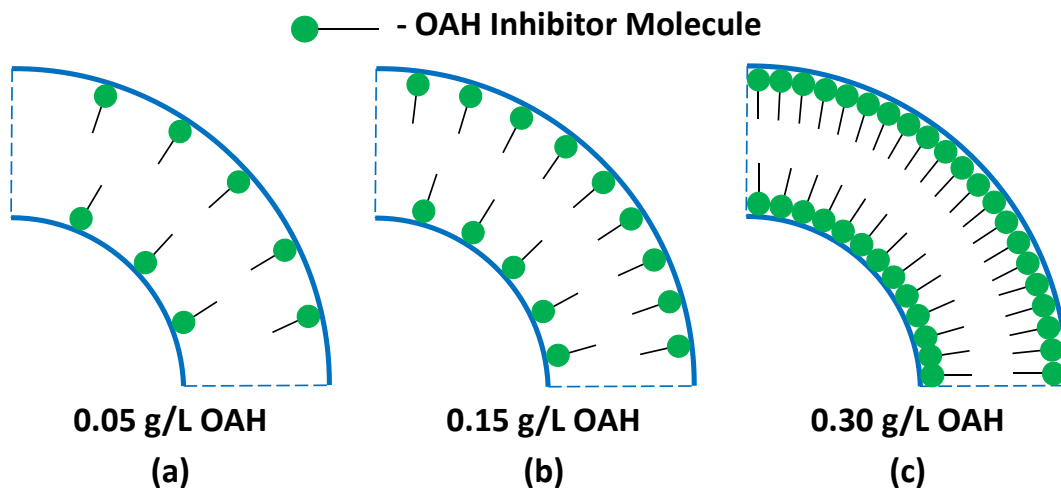
Figure 4.21 Schematic of adsorption (OAH inhibitor molecules) on elbow test section at various concentrations (a) 0.05 g/L (b) 0.15 g/L, and (c) 0.30 g/L

Nyquist plots [Figure 4.14(a-f)] from the electrochemical impedance spectroscopy measurements are defined by a capacitive loop in the absence and presence of the OAH inhibitor in FAC conditions. The capacitive loop was responsible for the charge transfer process at the electrode-electrolyte interface by the reaction. The semicircle radii of the capacitive loops in the impedance spectra were increased by the addition of the OAH inhibitor in the flow condition. Polarization resistances (R_p) increased with the increase of concentration of OAH inhibitor, which indicates protection of X70 steel. R_p values of the electrodes with inhibitor-containing electrolyte were higher than that of without it. It indicates that the OAH inhibitor was adsorbed on the specimen surface and is quite efficient for chosen alloy and environment significantly at 0.30 g/L concentration (Liu et al. 2009; Neville and Wang 2009).

It is accepted that the organic compounds mitigate the corrosion by the adsorption process at the metal-electrolyte interface (L. Riggs Jr 1973). Organic compounds act as mixed-type inhibitors, which provide a barrier to dissolution at the anode and a barrier to oxygen reduction at cathodic sites (Sastri 2011). A possible inhibition mechanism exhibited by the organic OAH molecule is the adsorption process on the metal surface. It acts as an obstacle for the degradation of the X70 steel in the electrolyte by providing a strong barrier to electrochemical corrosion reactions. It is generally accepted that the first step in the adsorption of an organic inhibitor on a metal surface usually involves the replacement of one or more water molecules adsorbed at the metal surface as given in equation 4.15 (Ashassi-Sorkhabi and Asghari 2008).

$$Inh_{(sol)} + nH_2O_{(ads)} \leftrightarrow Inh_{(ads)} + nH_2O_{(sol)} \qquad (4.15)$$
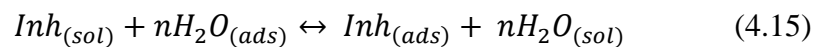
The inhibitor may then combine with freshly generated Fe^{2+} ions on the steel surface, forming metal-inhibitor complexes as given in equations 4.16 and 4.17 (Oguzie et al. 2007):

$$Fe \rightarrow Fe^{2+} + 2e \qquad (4.16)$$

$$Fe^{2+} + Inh_{(ads)} \rightarrow [Fe - Inh]^{2+}_{(ads)} \qquad (4.17)$$
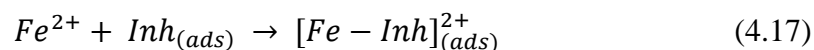
The OAH inhibitor used in this study consists of hydrazide, and it forms metal-inhibitor complexes due to Fe–N interactions. Mostly, hydrazide products adsorb onto the metal surfaces due to the formation of lone pairs of electrons, which are already

present in nitrogen and oxygen atoms (polar groups) through the π-electrons present in these molecules as illustrated in Figure 4.22 (Quaraishi et al. 2000). The subsequent complex (Fe-Inh)$^{2+}$, depending on its relative solubility, can either inhibit or catalyze further metal dissolution. At low concentrations, the quantity of OAH in the solution is deficient in forming a complex with the metal ions so that the resulting adsorbed intermediate will be dissolved in the solution. But at higher concentrations, the availability of OAH molecules for complex formation is more, which then diminishes the solubility of the surface layer, leading to a better inhibiting effect (Ashassi-Sorkhabi and Asghari 2008). However, hydrodynamic parameters of the turbulent fluid flow can also influence the inhibition of steel corrosion. The existence of more inhibitor molecules at the metal surface and better inhibition performance is ensured by the flow of fluid. However, the mass transfer process of the metal ions (Fe^{2+}) to the bulk of the solution is enhanced by the hydrodynamic effect of the flow. Hence, the formation of (Fe-Inh)$^{2+}$ complex or protective inhibitor film on the metal surface is retarded by fluid hydrodynamics. The high shear stress, parallel to the pipe wall and turbulence caused by the high flow velocity retards the adsorption process of (Fe-Inh)$^{2+}$ complex and damages the protective inhibitor film that previously has adsorbed on the metal surface. These processes lead to changes in inhibition efficiency at various locations of the pipe elbow and act as a negative effect on inhibition efficiency (Ahmed 2012; Ashassi-Sorkhabi and Asghari 2008; Lopes-Sesenes et al. 2013).
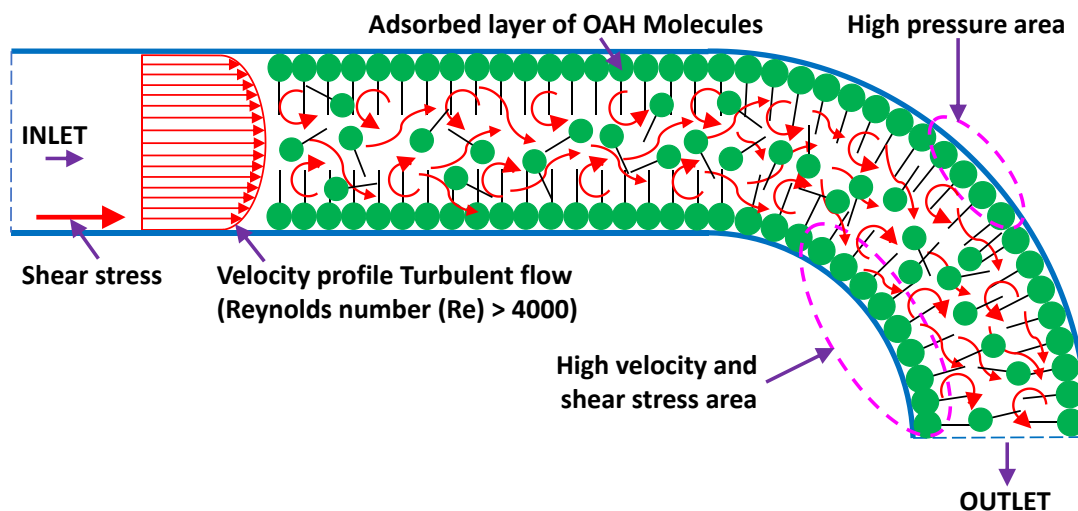
Figure 4.22 Schematic of the interaction of OAH inhibitor molecules at the internal wall of the pipe and elbow under turbulent flow condition

The FTIR spectrum (Figure 4.17) of corrosion products of inhibited FAC sample shows that there is a small shift as compared to the pure OAH inhibitor. This is also attributed to the interaction of inhibitor molecules with the sample. The SEM morphologies [Figure 4.15(a, b)] indicate fewer corrosion products are formed at high concentration (0.30 g/L) OAH inhibitor. This also implies that; OAH inhibitor protects the electrodes from severe FAC damage. XPS spectra (Figures 4.18 and 4.19) also reveal that the OAH is forming an inhibitor film on the surface of the API X70 steel sample under FAC condition.

4.2.4 Summary

The inhibition effect of a green inhibitor, a fatty acid derivative, oleic acid hydrazide (OAH) was studied in the dynamic corrosive environment. A loop system was utilized to imitate the flow through a pipe more realistically. The major findings of this study are given below.

- Studied green corrosion inhibitor-oleic acid hydrazide (OAH) is good in the protection of the API X70 steel with higher efficiency in the dynamic corrosive environment at 0.30 g/L concentration. The maximum inhibitor efficiency is found at 87.7% for 0.30 g/L concentration. This organic inhibitor forms metal-inhibitor complexes by adsorption behavior of the organic adsorbate on the sample surface.

- The inhibition efficiencies of the API X70 samples at the elbow test section is varying concerning the locations of the electrode. This is due to the drastic changes in flow patterns resulting from the hydrodynamic parameters such as turbulence, velocity, and shear stress, as well as the flow separation, and secondary flow effect, which will lead to the generation of counter rotating vortices, and various scale eddies at the elbow.

- Compared to 0.30 g/L, the inhibition efficiency of OAH for FAC is relatively low at 0.05 and 0.15 g/L. The maximum inhibition efficiencies observed for 0.05 g/L, and 0.15 g/L OAH concentrations are 23.5%, and 42.7% respectively. This is due to the hydrodynamic effect of flow, such as high wall shear stress and velocity during the FAC test, which prevents the adsorption of the inhibitor and damages the adsorbed inhibitor film at a lower concentration.

- The hydrodynamic parameters control the flow pattern, alter the mass transfer rate of OAH inhibitor molecules and metal ions (Fe^{2+}) at various locations of the elbow test section, and influence the inhibition effect of the OAH inhibitor under flow condition.

4.3   Effect of laser surface melting (LSM) on FAC of API X70 steel

The effect of laser surface melting - LSM (laser powers 2, 2.5, and 3 kW) on flow accelerated corrosion (FAC) of API X70 steel was studied in the synthetic oil field water. Seven electrodes at extrados (E1, E5, E7, and E9) and intrados (E14, E16, and E17) were selected at the 90º elbow test section of the flow loop system for testing. Static corrosion tests were also performed to compare the flow condition effect on LSM steel. Microstructural and microhardness tests were performed to analyze the surface metallurgical changes such as elemental segregation, surface defects due to the LSM process on API X70 steel.

4.3.1   Corrosion behavior of laser surface melted (LSM) API X70 steel

- **Under static condition**

Corrosion behavior of laser surface melted (LSM) X70 steel samples were analyzed with the help of the Tafel extrapolation method in the synthetic oil field water in static condition and plots are shown in Figure 4.23. The calculated corrosion rates from the plots for the laser powers 2, 2.5, and 3 kW under the static condition are 1.8, 1.4, and 1.9 mpy respectively. The LSM sample with laser power 2.5 kW shows better corrosion resistance as compared to other treated samples.
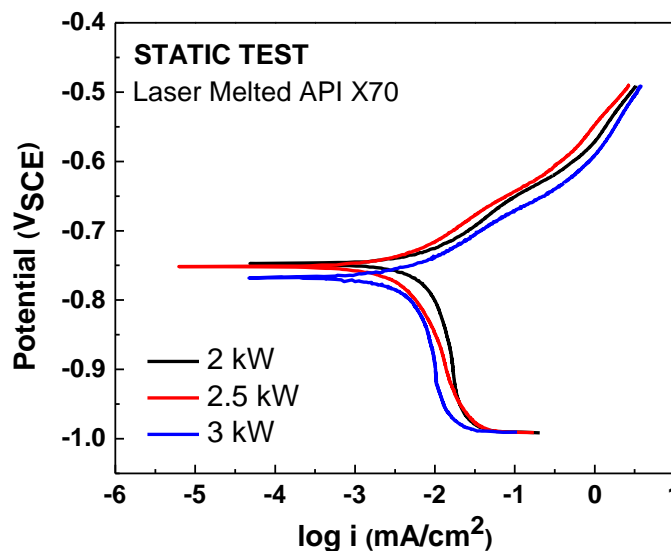
Figure 4.23 Tafel plots of laser surface melted (laser powers 2, 2.5, and 3 kW) X70 samples under static condition

- **Under flow condition (FAC)**

FAC tests of laser-treated (laser powers 2, 2.5, and 3 kW) X70 steel of seven electrodes at extrados and intrados positions were carried out using the Tafel extrapolation method in the synthetic oil field water in the loop system. Tafel plots of the electrodes E1, E5, E7, and E9 (extrados) and E14, E16, and E17 (intrados) for the laser powers 2, 2.5, and 3 kW are shown in Figures 4.24(a), 4.24(b) and 4.24(c) respectively. It is noticed from plots that the samples were susceptible to higher corrosion under flow condition. Corrosion rates obtained from the Tafel plots are tabulated in Table 4.11. From that, it is very much clear that, corrosion rates of laser-treated samples are more at FAC condition than at static condition due to the presence of hydrodynamic parameters by the fluid flow (Jiang et al. 2005; Lopes-Sesenes et al. 2013; Vera et al. 2015).

Among the laser melted samples, 2.5 kW laser power electrodes exhibited relatively lesser corrosion rates or better protective behavior over other power treated samples. Corrosion rates of the extrados electrodes of 2.5 kW laser power are noted about 8.5 mpy [E1, polar angle (θ = 72º)], 8.6 mpy [E5, polar angle (θ = 75º)], 12.1 mpy [E7, polar angle (θ = 45º)], and 18.5 mpy [E9, polar angle (θ = 15º)]. Furthermore, corrosion rates of the intrados electrodes of 2.5 kW laser power are noted about 12.3 mpy [E14, polar angle (θ = 67.5º)], 13.7 mpy [E16, polar angle (θ = 22.5º)], and 24.6 mpy [E17, polar angle (θ = 45º)]. It clearly indicates the corrosion rates of the electrodes decrease from intrados to extrados for selected electrodes (El-Gammal et al. 2010; Poulson 1999). However, the corrosion rates are highest in electrode E17 at a polar angle (45º) and a fixed azimuthal angle (0º) in column E and lowest in electrode E1 at a polar angle (72º) and a fixed azimuthal angle (135º) in column A. Furthermore, the corrosion rates of the untreated (UT) X70 samples are in the range of 450-600 mpy under the same FAC condition (*see section 4.1.4*). Therefore, it is inferred that the laser surface melting results in a significant reduction in corrosion rates of X70 steel samples over UT. The shear stress values obtained from CFD simulation (*see section 4.1.3*) corresponding to each electrode are also tabulated in Table 4.11. The corrosion rate is directly proportional to the wall shear stress.

Figure 4.24 Tafel plots of laser surface melted X70 samples tested under FAC condition for the laser powers (a) 2 kW, (b) 2.5 kW, (c) and 3 kW

Table 4.11 Fitted parameters and corrosion rates for the Tafel plots of laser surface melted (laser powers 2, 2.5, and 3 kW) API X70 samples under FAC condition

	Azimuthal Angle (φ)	Polar Angle (θ)	Electrodes	Shear Stress (Pa)	Corrosion Rate (mpy)		
					2	2.5	3
					kW		
Extrados (Outer face)	135° (Column A)	72°	E1	11.3	18.2	8.5	15.7
	180° (Column B)	75°	E5	8.4	19.7	8.6	17.3
		45°	E7	13.3	29.5	12.1	19.5
		15°	E9	20.8	33.9	18.5	45.3
Intrados (Inner face)	315° (Column D)	67.5°	E14	24.8	30.3	12.3	23.9
		22.5°	E16	25.6	32.3	13.7	39.8
	0° (Column E)	45°	E17	27.6	35.2	24.6	50.3

4.3.2 Electrochemical impedance spectroscopy (EIS) test

- **Under static condition**

Passivation behavior of laser surface melted (laser powers 2, 2.5, and 3 kW) X70 steel samples were analyzed by electrochemical impedance spectroscopy (EIS) method in static condition. Figure 4.25 shows the Nyquist plots of laser melted X70 samples obtained by static EIS test. The charge transfer resistances for the laser powers 2, 2.5, and 3 kW obtained after analyzing the impedance spectra using an electrical equivalent circuit given in Figure 4.26 were 2462, 2532, and 2356 Ω cm^2 respectively. From this, it is clear that the 2.5 kW laser power sample shows better corrosion resistance as compared to 2 and 3 kW.
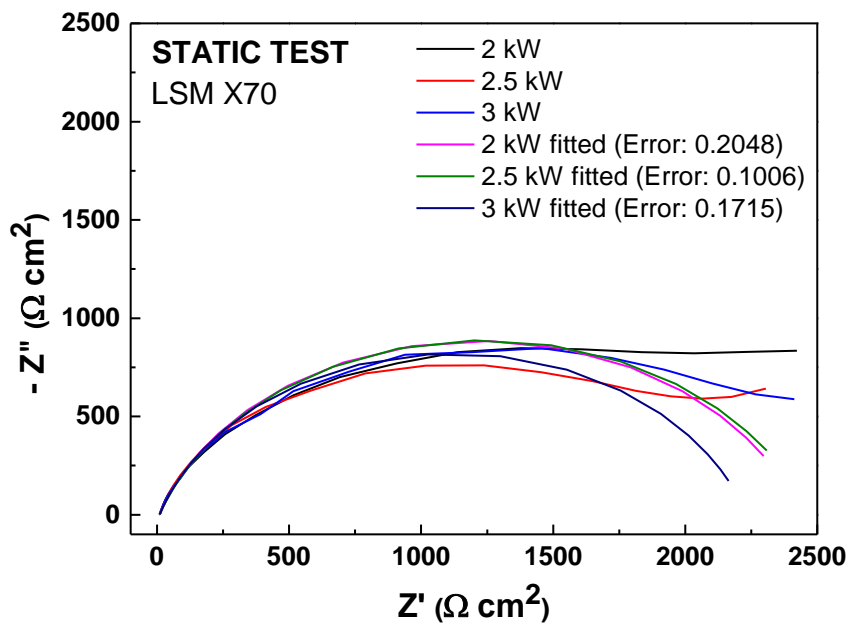
Figure 4.25 Nyquist plots of laser surface melted (laser powers 2, 2.5, and 3 kW) API X70 samples under static condition
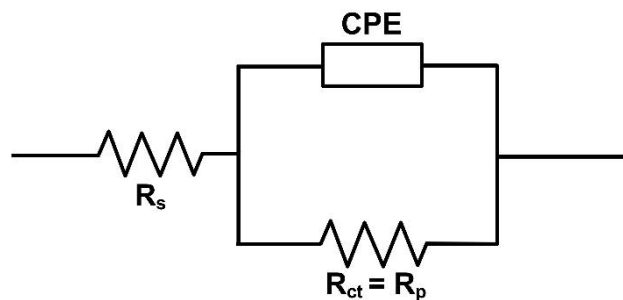
Figure 4.26 Equivalent circuit used for EIS plot fitting

96

- **Under flow condition (FAC)**

FAC tests of laser-melted (laser powers 2, 2.5, and 3 kW) X70 steel of various electrodes at extrados and intrados of the elbow were carried out using the electrochemical impedance spectroscopy (EIS) method in the synthetic oil field water in the loop system. Nyquist plots of the electrodes E1, E5, E7, and E9 (extrados) and E14, E16, and E17 (intrados) for the laser powers 2, 2.5, and 3 kW are shown in Figures 4.27(a), 4.27(b), and 4.27(c) respectively. The charge transfer resistance of each sample obtained after analyzing the impedance spectra using the electrical equivalent circuit given in Figure 4.26 is tabulated in Table 4.12. It is seen that compared to static condition the semi-circle radius of the capacitive loop which is responsible for the charge transfer resistance is much smaller (Lopes-Sesenes et al. 2013). It indicates that higher metal dissolution occurred during FAC tests compared to the static corrosion tests.

Among the laser melted samples, 2.5 kW laser power electrodes exhibited relatively higher charge transfer resistances or better protective behavior. Charge transfer resistances of the extrados electrodes of 2.5 kW laser power are noted about 1594 Ω cm^2 [E1, polar angle ($\theta = 72^\circ$)], 1467 Ω cm^2 [E5, polar angle ($\theta = 75^\circ$)], 1191 Ω cm^2 [E7, polar angle ($\theta = 45^\circ$)], and 891 Ω cm^2 [E9, polar angle ($\theta = 15^\circ$)]. Furthermore, charge transfer resistances of the intrados electrodes of 2.5 kW laser power are noted about 1061 Ω cm^2 [E14, polar angle ($\theta = 67.5^\circ$)], 1010 Ω cm^2 [E16, polar angle ($\theta = 22.5^\circ$)], and 844 Ω cm^2 [E17, polar angle ($\theta = 45^\circ$)]. The charge transfer resistances of the electrodes decrease from extrados to intrados (El-Gammal et al. 2010; Poulson 1999). The charge transfer resistances are highest in electrode E1 at a polar angle (72º) and a fixed azimuthal angle (0º) in column A and lowest in electrode E17 at a polar angle (45º) and a fixed azimuthal angle (135º) in column E. The charge transfer resistances of the untreated (UT) X70 samples are in the range of 70-90 Ω cm^2 under the same FAC condition (*see section 4.1.5*).

Therefore, it is clear that all the LSM samples show better corrosion resistance compared to the UT samples. The shear stress values obtained from CFD simulation (*see section 4.1.3*) corresponding to each electrode are also tabulated in Table 4.12. The

charge transfer resistances for the electrodes are fluctuating depending upon the wall shear stress values within the elbow test section.
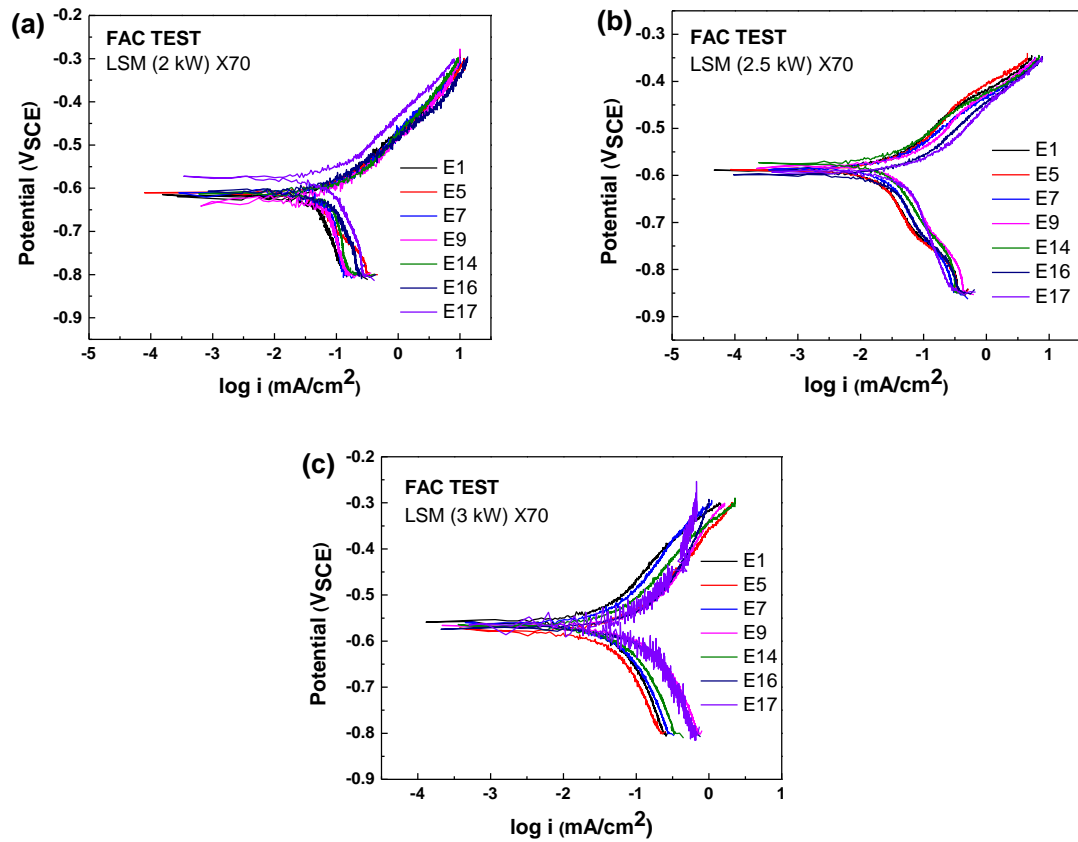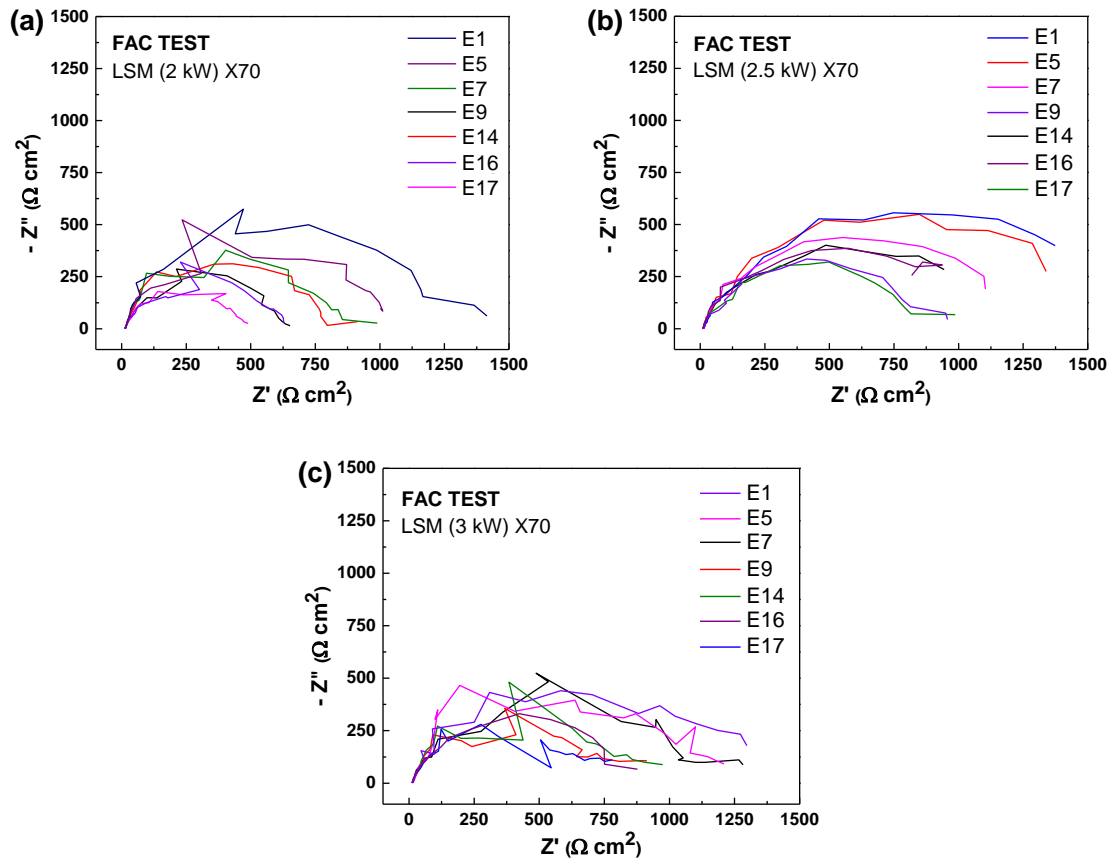

Figure 4.27 Nyquist plots of laser surface melted X70 samples tested under FAC condition for the laser powers (a) 2 kW, (b) 2.5 kW, (c), and 3 kW

Table 4.12 Fitted parameters and charge transfer resistance for the Nyquist plots of laser surface melted (laser power: 2 kW) API X70 samples under FAC condition

	Azimuthal Angle (φ)	Polar Angle (θ)	Electrodes	Shear Stress (Pa)	R_{ct} (Ω cm^2)		
					2	2.5	3
					kW		
Extrados (Outer face)	135° (Column A)	72°	E1	11.3	1300	1594	1264
	180° (Column B)	75°	E5	8.4	1019	1467	1143
		45°	E7	13.3	843	1191	1143
		15°	E9	20.8	629	891	781
Intrados (Inner face)	315° (Column D)	67.5°	E14	24.8	797	1061	864
		22.5°	E16	25.6	623	1010	842
	0° (Column E)	45°	E17	27.6	467	844	699

4.3.3 Material characterizations

- **Microhardness of untreated (UT) and laser surface melted (LSM) samples**

The microhardness measurements of UT and LSM (laser powers 2, 2.5, and 3 kW) X70 samples were performed with the help of a Vickers hardness testing machine by applying a 0.2 kg load for 15 s. The cross-sectional microstructure with hardness test indents and corresponding micro-hardness profile of the 2.5 kW LSM sample is depicted in Figure 4.28(a, b). The microhardness values were obtained as: 220 HV 0.2 - *UT* < 312 HV 0.2 - *3 kW* < 318 HV 0.2 - *2 kW* < 330 HV 0.2 - *2.5 kW*. It clearly illustrates hardness improvement from 260 HV to 330 HV in the laser-treated zone as against 220 HV to 240 HV in the substrate. These microhardness values of the LSM treated samples are mainly due to the formation of the martensite phase (Agarwal et al. 2014; Kayali and Anaturk 2013). This similarity in the microhardness values of the LSM samples and martensite phase suggests that the ferrite and perlite (untreated condition) transformed into martensite during the rapid melting and solidification process associated with the laser surface melting (Luo et al. 2010).

(a)   **(b)**
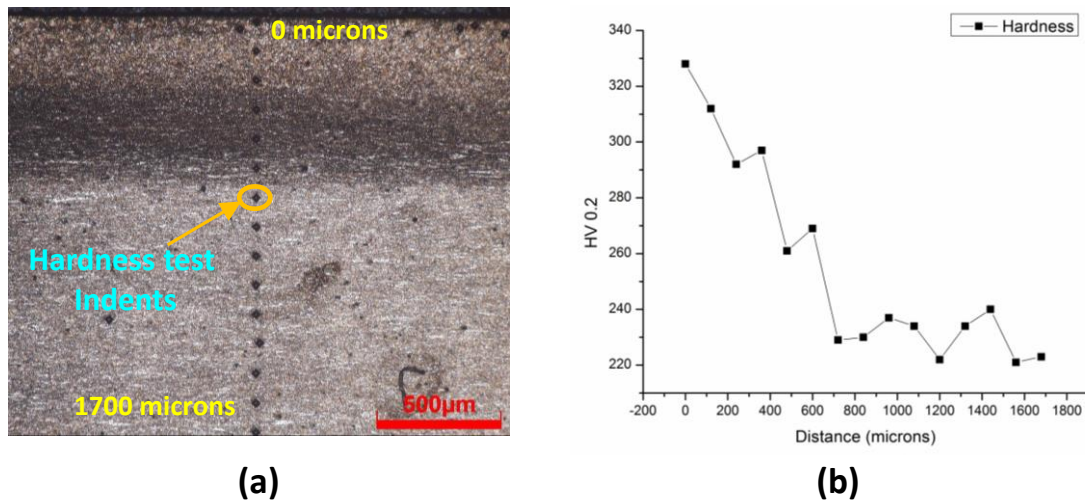
Figure 4.28 Cross-sectional (a) microstructure with hardness test indents and (b) corresponding micro-hardness distribution profile of the 2.5 kW LSM sample

- **Microstructural analysis of UT and LSM samples**

As microstructure in contact determines the hardness and tribological performance of steel, Scanning Electron Microscopy - SEM (surface) and optical microscopy - OM (cross-sectional) images of UT and LSM X70 steel, were compared and assessed for their properties. Surface SEM images of UT and LSM (2.5 kW and 3 kW) samples with magnifications of 2000X and 5000X are given in Figures 4.29(a-c) and 4.30(a-c), respectively. Figure 4.31(a-c) depicts the cross-sectional (optical) microstructures of UT and LSM samples with a magnification of 100X. The laser-treated zone thickness of 2.5 kW and 3 kW LSM samples are observed at about 472 and 748 μm, respectively.

As the LSM process of steel involves fast localized melting and solidification on the surface as well as subsurface, a unique and refined microstructure is formed. To see optical and SEM micrographs, a distinguishable microstructure was obtained for X70 steel, after LSM treatment. A vast variation in terms of dendritic formation, grain size, and morphological features is observed on LSM treated samples due to higher nucleation density and low growth rate. A fine-grain dendritic microstructure can be seen in the laser-treated area as against typical pearlitic-ferritic structure in the bare alloy (substrate) or unaffected base metal, which is the best agreement with reported studies of laser hardened and melted steels (Vora and Dahotre 2013; Zhao et al. 2016).

To see SEM micrographs from Figures 4.29(a-c) and 4.30(a-c), it can be inferred that, the ferrite-pearlite structure of untreated (UT) steel got transformed to displacive transformation products, which is primarily martensite, with a small fraction of Widmanstätten ferrite and bainite (Avner 1997; Callister Jr. and Rethwisch 2014; Yilbas et al. 2013; Zhao et al. 2016). According to Bhadeshia et al. (2017), these displacive transformations consists of Widmanstätten ferrite, bainite, and martensite involve the cooperative atomic movements and displays lath, plate, and wedgelike microstructures and supported by Martino et al. (2014) (Bhadeshia and Honeycombe 2017; Di Martino and Thewlis 2014). However, the rapid cooling process associated with the LSM process of steels promotes the transformation of austenite into martensite, a diffusionless transformation (Vilar 2012; Vora and Dahotre 2013). Furthermore, careful observation of LSM microstructures did not show cracks or pores, indicating accommodation of stresses due to optimum processing parameters and conditions utilized for processing and low-carbon content steel chemistry (Mudali and Dayal 1992; Zhao et al. 2016).

(a) UT
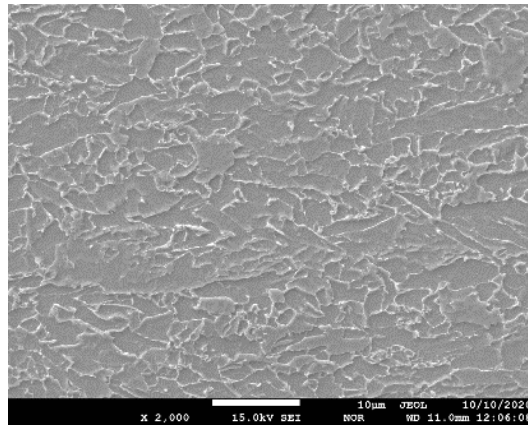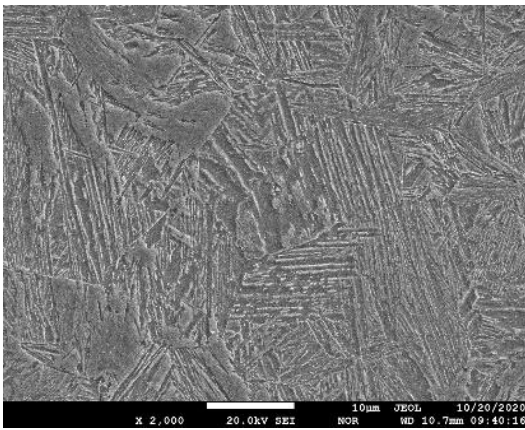
(b) 2.5 kW
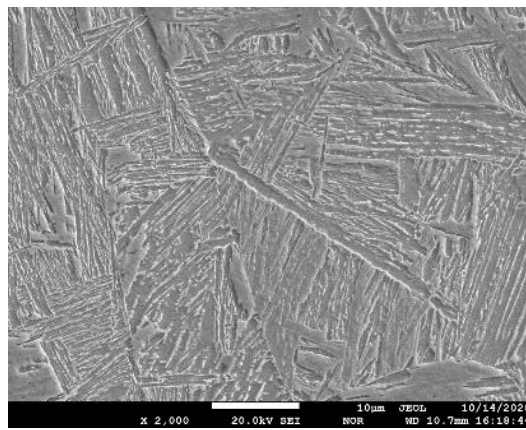
(c) 3 kW

Figure 4.29 Surface: SEM images (2000X) of X70 steel (a) Untreated - UT; and Laser surface melted - LSM (b) 2.5 kW, (c) 3 kW

(a) UT
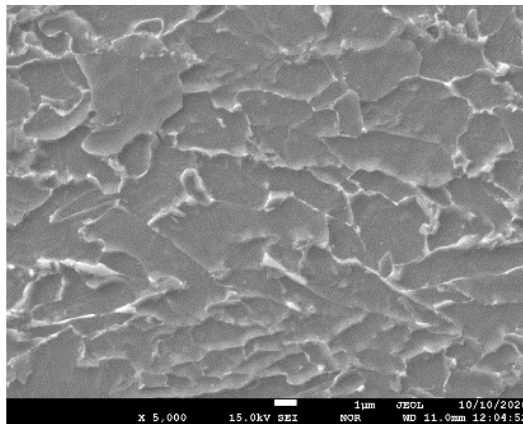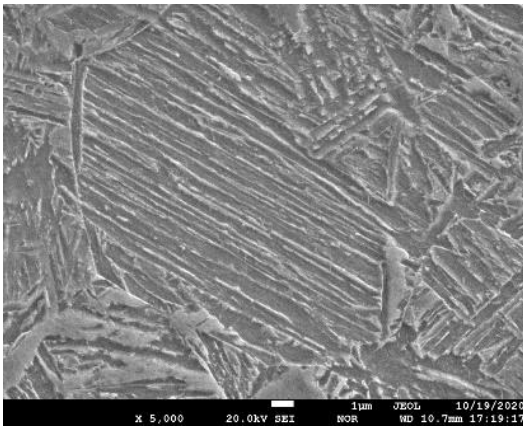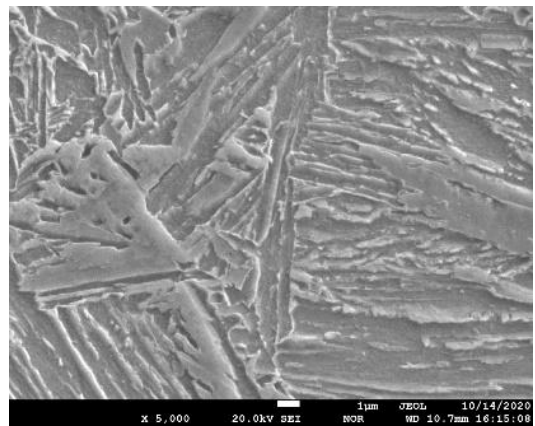
(b) 2.5 kW

(c) 3 kW

Figure 4.30 Surface: SEM images (5000X) of X70 steel (a) Untreated - UT; and Laser surface melted - LSM (b) 2.5 kW, (c) 3 kW

(a) UT
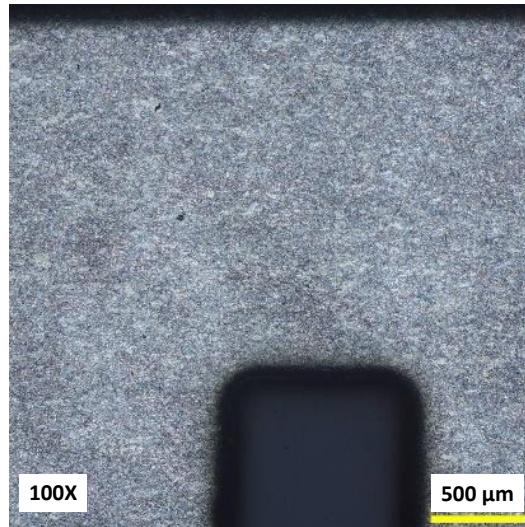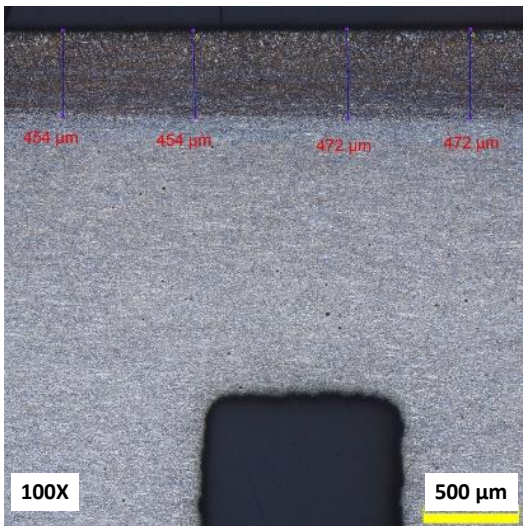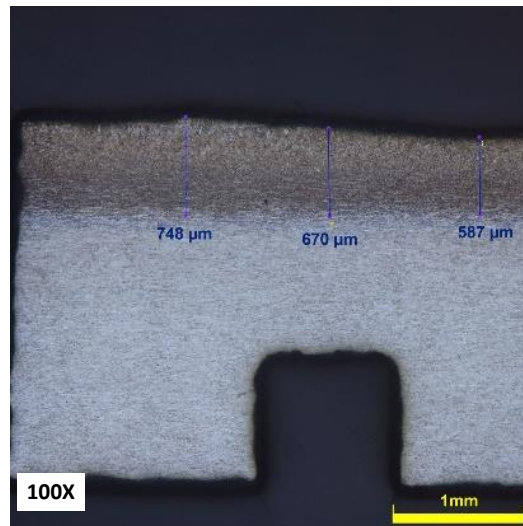
(b) 2.5 kW

(c) 3 kW

Figure 4.31 Cross-section: optical micrographs (100X) of X70 steel (a) Untreated - UT; and Laser surface melted - LSM (b) 2.5 kW, (c) 3 kW

- **Elemental analysis of UT and LSM samples**

The energy-dispersive spectroscopy (EDS) technique was used for the elemental analysis. The EDS results of the UT and LSM (laser power 2.5 kW) X70 samples are given in Figure 4.32(a, b). It is interesting to see that two additional elements, titanium and nickel, were segregated on the LSM sample due to the melting and solidifying process. In addition to that, the elemental weight % of copper and manganese were increased after the LSM process. A slight decrease in the weight % of chromium and niobium was also observed. These grain-boundary elemental segregations are quite beneficial for corrosion resistance, which assist in the formation of passive film on the surface of steel (AlMangour et al. 2019; Alves et al. 2001). The rapid heating process entailed in LSM prevents the decomposition of metallic carbides such as NbC and TiC, and further stops the growth of austenitic grains in the melted region and also improves the strength of steel drastically (Zhao et al. 2016).

(a) Untreated API X70
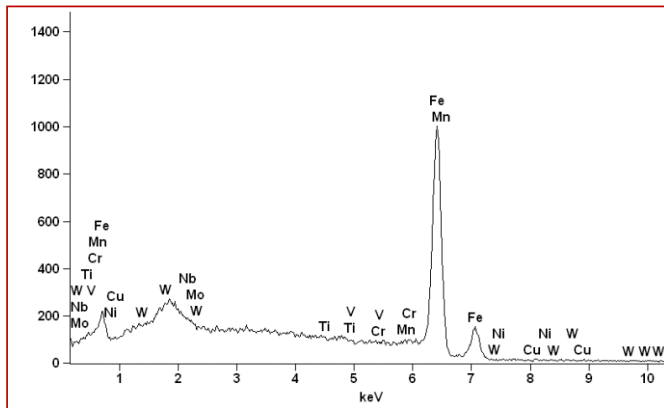
Element	Weight %
Cr K	0.15
Mn K	1.55
Nb L	0.93
Cu K	0.24
Fe K	97.13

(b) LSM (2.5 kW) API X70
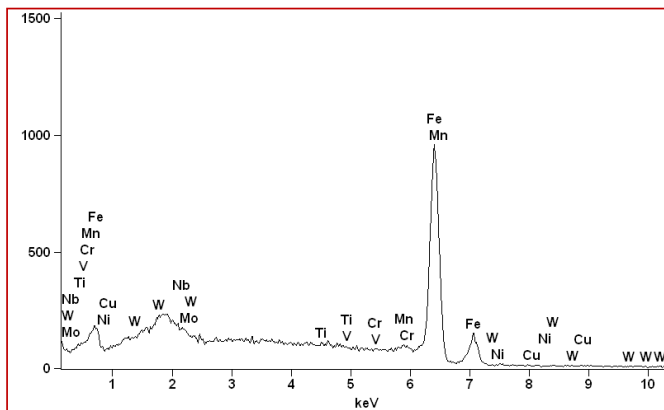
Element	Weight %
Cr K	0.10
Mn K	2.08
Nb L	0.81
Cu K	0.38
Ti K	0.19
Ni K	0.16
Fe K	96.27

Figure 4.32 EDS spectra, and chemical compositions of API X70 steel samples (a) untreated, and (b) laser surface melted (laser power - 2.5 kW)

- **Phase analysis of UT and LSM samples**

In order to understand the phase transformation and refinement of grain size, the microstructural analysis was performed with the X-ray diffraction (XRD) technique and compared for UT and LSM (laser power 2.5 kW) X70 steel samples. XRD patterns and crystallographic structure parameters obtained are depicted in Figure 4.33 and Table 4.13. Miller indices (hkl) of lattice planes of the unit cells are tabulated along with their d-spacing (the spacing between planes) according to Bragg's law (Bindu and Thomas 2014; Zhang and Guyot 1999). A careful observation of diffraction patterns of UT and LSM layers indicating that there is a meager lower angle shift in diffraction angle (2ϴ) along with clear peak broadening in the LSM sample, indicating a relative expansion in average lattice parameter as compared to the untreated steel. This could be attributed

to the induced micro-strain (calculated according to Wilson's formula) and crystallite-size (calculated according to Scherrer's equation) reduction effects in martensite cells of LSM (Holzwarth and Gibson 2011; Klug and Alexander 1974; Miranda and Sasaki 2018; Rai et al. 2016).
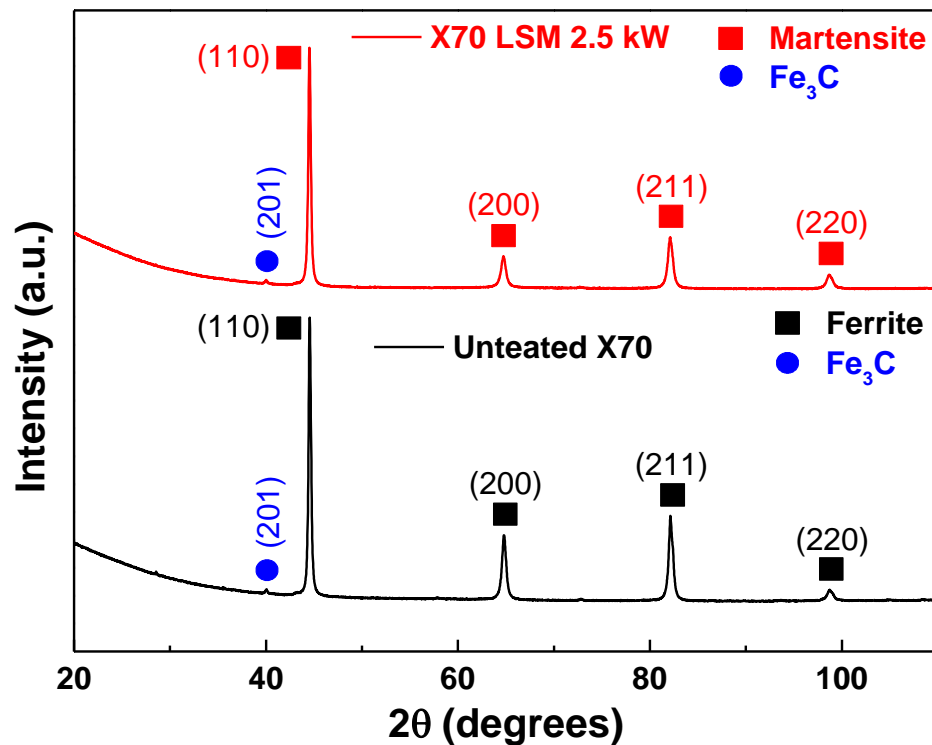
Figure 4.33 XRD patterns of the untreated and LSM (2.5 kW) X70 steel

The full width at half maximum (FWHM) is obtained from the best fitting of XRD data and it varies inversely with possible crystallite size of grains at a given diffraction angle. The increased microstrain values (Table 4.13), accompanying peak broadening of the LSM sample, which is often produced by high dislocations and lattice distortions. These results are indicating movements of the unit cell about its normal position and changes in unit cell dimensions (Hargreaves 2016). Dislocation density, measured according to crystallite size, was also observed to be about 22% higher in LSM than UT steel.

Hence, it is clear that the reason for increment in peak width, intensity, and shift in peak position (2Ө) of laser melted sample is due to the significant reduction in crystallite size and increment in microstrain and dislocation density. Thus variation in crystallographic structure parameters further confirmed a martensite transformation in

the laser melted layer of X70 steel (Sauvage et al. 2003). Thus, LSM treatment that resulted in grain refinement and martensite transformation of the X70 steel surface could alter the erosion-corrosion behavior (Vilar 2012; Zhao et al. 2016).

Table 4.13 Parameters obtained from XRD patterns of untreated and LSM - X70 steel

	Untreated			
2ϴ (°)	**44.56**	**64.80**	**82.17**	**98.77**
FWHM β (°)	0.2784	0.4791	0.5008	0.7531
Crystallite Size L (nm)	32.24	20.53	22.00	16.94
d spacing (nm)	0.2033	0.1439	0.1173	0.1015
Rel. Int. (%)	100	23.20	30.43	3.87
hkl	110	200	211	220
Dislocation density $(\delta) \times 10^{-3}$ (nm^{-2})	0.9621	2.3726	2.0665	3.4859
Microstrain $(\mathcal{E}) \times 10^{-3}$	2.9640	3.2936	2.5062	2.8180
	LSM 2.5 kW			
2ϴ (°)	**44.54**	**64.74**	**82.13**	**98.72**
FWHM β (°)	0.2854	0.5800	0.5937	0.7445
Crystallite Size L (nm)	31.44	16.95	18.55	17.12
d spacing (nm)	0.2034	0.1440	0.1174	0.1016
Rel. Int. (%)	100	12.99	21.35	5.89
hkl	110	200	211	220
Dislocation density $(\delta) \times 10^{-3}$ (nm^{-2})	1.0118	3.4799	2.9059	3.4101
Microstrain $(\mathcal{E}) \times 10^{-3}$	3.0413	3.9921	2.9732	2.7883

- **Microstructural and phase analysis with EBSD technique**

Electron Backscatter Diffraction (EBSD) tool is utilized in this study to analyze the clarity of microstructure and the phases of UT and LSM samples. EBSD, joined with scanning electron microscopy (SEM), is a powerful research technique for studying structural properties co-relationship. EBSD has flexibility concerning magnification level and resolution and utilizes highly sophisticated postprocessing algorithms to define crystallographic orientations, microstructural features, and phase identification (Gussev and Leonard 2019).

The image quality (IQ) map is represented in grayscale, and it offers a depiction of the actual microstructure as in conventional scanning or optical microscopy (Zhilyaev et al. 2003). The IQ map characterizes not only the actual microstructure, but also the grain boundaries, voids, and even microcracks (Kim and Szpunar 2009). Figure 4.34(a-c) depicts the image quality (IQ) maps obtained for untreated (UT), and laser surface melted (2.5 and 3 kW) X70 steel samples. The UT sample reveals the ferritic structure, whereas the LSM samples disclose a typical lath martensite structure with grain boundaries which usually form in low carbon steel under rapid cooling from the austenite region. These images further did not exhibit any type of cracks and pores for treated samples of selected laser powers. It is only possible due to the accommodation of stresses by employing optimum processing parameters for operation and low carbon steel (Mudali and Dayal 1992; Zhao et al. 2016).

Inverse pole figure (IPF) maps of selected regions of UT and LSM (for laser powers 2.5 and 3 kW) X70 steel samples are presented in Figure 4.35(a-d). The IPF map instructs grain structure and grain orientation that constitutes the steel is occasionally called a map of crystal orientations with IPF coloring (Gussev and Leonard 2019; Lavigne et al. 2017). The color-coding system in the IPF map is beneficial to distinguish every grain and its preferred orientation. The IPF coloring corresponds to the crystallographic orientation normal to the observed plane, as indicated by the stereographic triangles shown in Figure 4.35d. For example, the grains oriented along {001}, {110} and {111} parallel to the normal direction are indicated in red, green, and blue, respectively (Kitahara et al. 2006; Masoumi et al. 2017).

From the IPF maps of UT and LSM samples, it can be confirmed that the UT sample shows a stronger texture and better-preferred orientation as compared to the LSM counterparts, possibly due to the controlled manufacturing technique (Thermomechanical Treatment) of API X70 steel (Villalobos et al. 2018). The reason for a comparatively weaker and random texture of laser-treated layers is the rapid solidification which forces the high nucleation density and inhibition of nucleation growth that leads to the formation of very fine grains without any preferred orientation (Vora and Dahotre 2013).

The morphology and crystallographic features are shown by the IPF map of untreated (UT) X70 steel sample [Figure 4.35(a, d)] implies, which primarily consists of ferrite (bcc) and a small amount of martensite (hcp). Mohtadi-Bonab et al. explained similar microstructure and phases for API 5L X70 line pipe steel and also confirmed the presence of a small amount of martensite, a major fraction of ferrite along with pearlite (Mohtadi-Bonab et al. 2017). Shin et al. also reported that the thermomechanical treated X70 steel leads to the formation of various phases, including martensite (Shin et al. 2007). Similar observations and results were presented by Dunne et al. also (Dunne et al. 2016). The IPF maps of LSM samples shown in Figure 4.35(b-d), clearly represent the detailed morphology and crystallographic features of the mixed martensite structure (bcc and hcp), primarily of lath martensite. The hcp martensite is formed due to the presence of manganese (1.488 wt.% > 1 wt.%) in the X70 steel (Nishiyama 1978).

The EBSD phase maps of untreated (UT) X70 steel samples are depicted in Figure 4.36a. From that, it is seen that the X70 steel consists of ferritic (95.6%) and martensitic (4.3%) phases, as expected, with the IPF and IQ maps. The phase maps of laser surface melted (2.5 and 3 kW), X70 steel samples are shown in Figure 4.36(b, c). The 2.5 kW LSM sample shows the presence of ferritic (87.8%) and martensitic (12.1%) phases. The phases displayed by the 3 kW LSM sample are slightly higher in ferritic (92.4%) content and slightly lower in martensitic (7.5%) content over the 2.5 kW treated sample. It is well known that the phase identification with the EBSD technique is working based on the crystallographic structure parameters. Based on this approach, presently the bcc martensite formed is recorded as bcc ferrite (basically

without interstitials, very low carbon content). However, the rapid cooling and solidification associated with the LSM process of X70 steel (Fe-Mn-C alloy) with ultra-low carbon content (0.05 wt.% < 0.25 wt.%) and manganese (1.488 wt.% > 1 wt.%) results in the transformation of fcc austenite to the bcc as well as hcp martensite by cooperative atomic movements (Nishiyama 1978; Sauvage et al. 2003; Zai et al. 2020; Zhang et al. 2016). Martensitic transformation of steel could be confirmed with the help of micro-hardness and transformed microstructures. In the present study of LSM samples, higher micro-hardness over untreated steel is in good agreement with the martensitic transformation. Hence, it can be concluded that, as a result of rapid melting and cooling, the ferrite-pearlite structure of untreated (UT) steel got transformed to displacive transformation products such as martensite, Widmanstätten ferrite, and bainite by the cooperative atomic movements and displays lath, plate, and wedgelike microstructures in LSM samples (Bhadeshia and Honeycombe 2017; Di Martino and Thewlis 2014).

The grain size diameter and grain size liner intercept obtained through EBSD scans for untreated, and LSM (2.5 and 3 kW) samples are well depicted in Figures 4.37(a-c) and 4.38(a-c), respectively. It is clearly found grain refinement in LSM samples. LSM samples 2.5 kW treatment contains more refined grains than 3 kW treatment. The reason for the presence of a greater number of fine grains on the LSM samples than the UT counterpart is the melting and self-quenching. This quenching process associated with the LSM process promotes the nucleation density and reduces the grain growth and thus the grains are refined (Vora and Dahotre 2013). In steels, a reduction in grain size can reduce the susceptibility to corrosion. In Fe-based alloys, as a result of increased rates of diffusion in fine-grained microstructures, passive film stability improves thus the corrosion resistance (Ralston and Birbilis 2010). Wang and Li (2003) studied the electrochemical properties of the nano-crystalline surface of the steel, and showed, that compared to samples with coarser grain size, fine-grained structures exhibited more rapid repassivation kinetics, which is an indication of stable films (Wang and Li 2003).
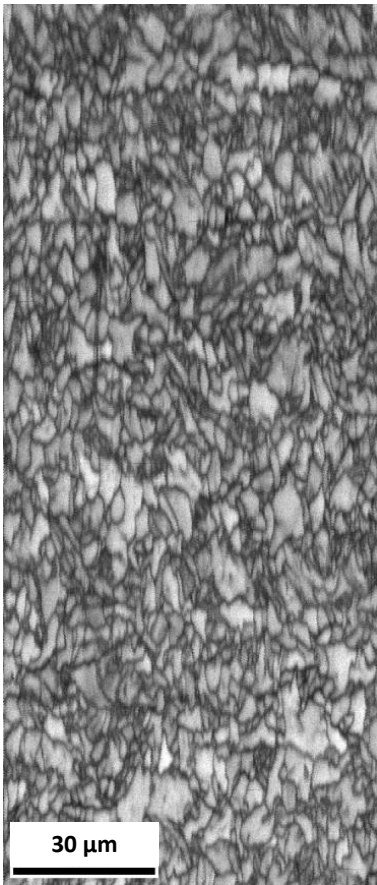
(a) *Untreated (UT)*   **(b)** *LSM : 2.5 kW*   **(c)** *LSM : 3.0 kW*

RD - Rolling Direction

TD - Transverse Direction
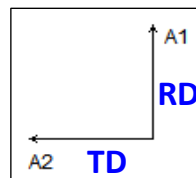
Figure 4.34 Image Quality (IQ) maps obtained for (a) Untreated (UT), (b) LSM: 2.5 kW, and (c) LSM: 3 kW, X70 samples

(a) *Untreated (UT)*   **(b)** *LSM : 2.5 kW*   **(c)** *LSM : 3.0 kW*
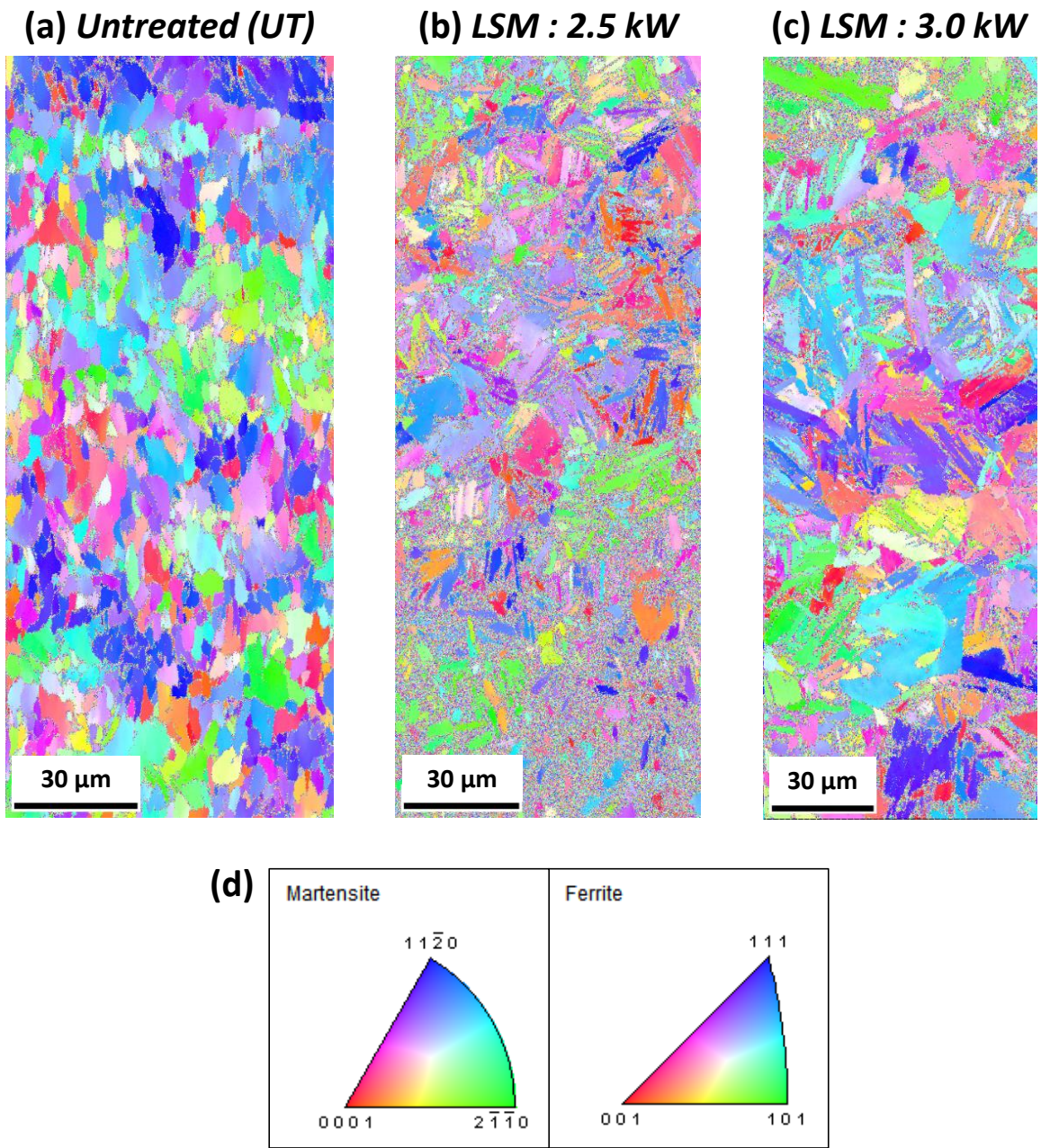
Figure 4.35 Inverse Pole Figure (IPF) maps obtained for (a) Untreated, (b) LSM: 2.5 kW, and (c) LSM: 3 kW, X70 samples, and (d) Stereographic triangles (IPF key is same for all maps)

(a) *Untreated (UT)*   **(b) *LSM : 2.5 kW***   **(c) *LSM : 3.0 kW***

Figure 4.36 Phase maps obtained for (a) Untreated, (b) LSM: 2.5 kW, and (c) LSM: 3 kW, X70 samples
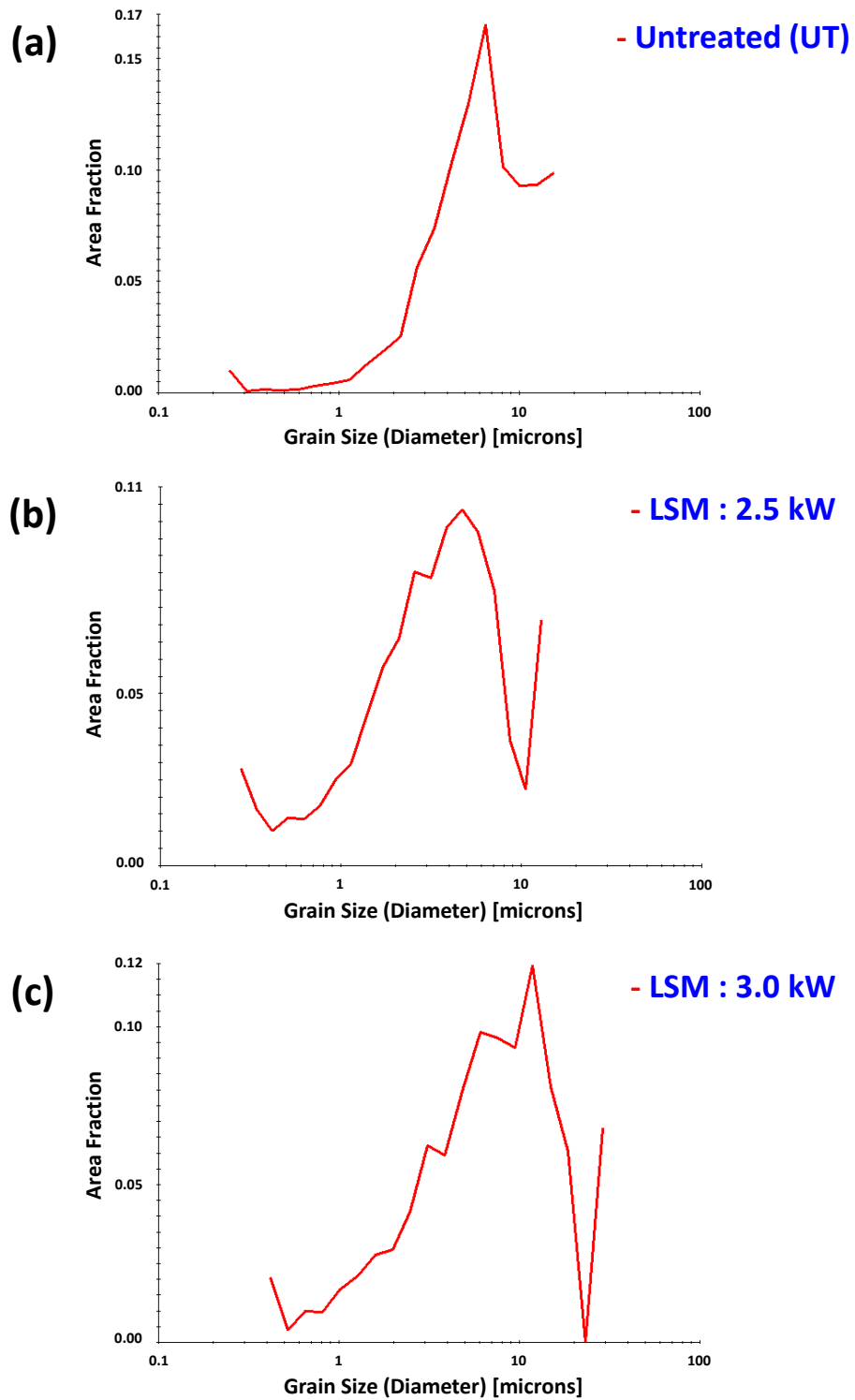
Figure 4.37 Grain size (Diameter) obtained for (a) Untreated, (b) LSM: 2.5 kW, and (c) LSM: 3 kW, X70 samples
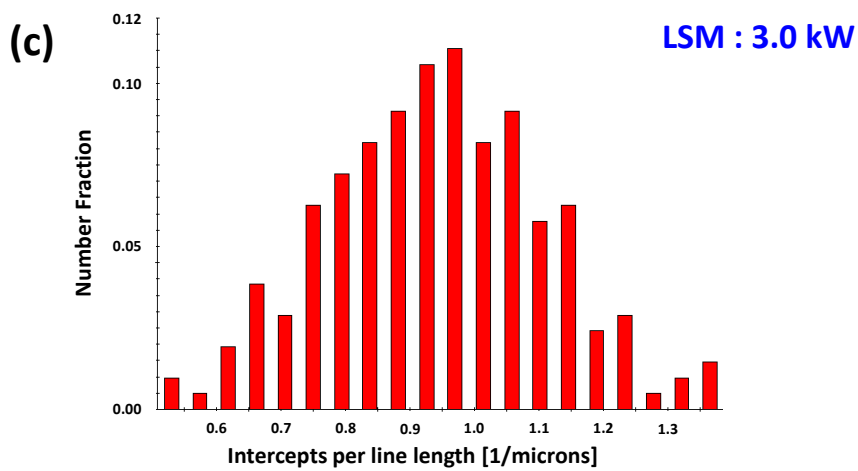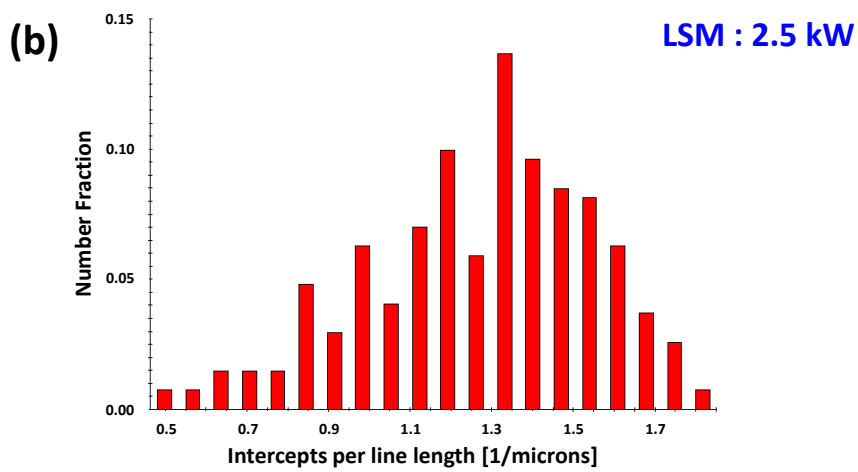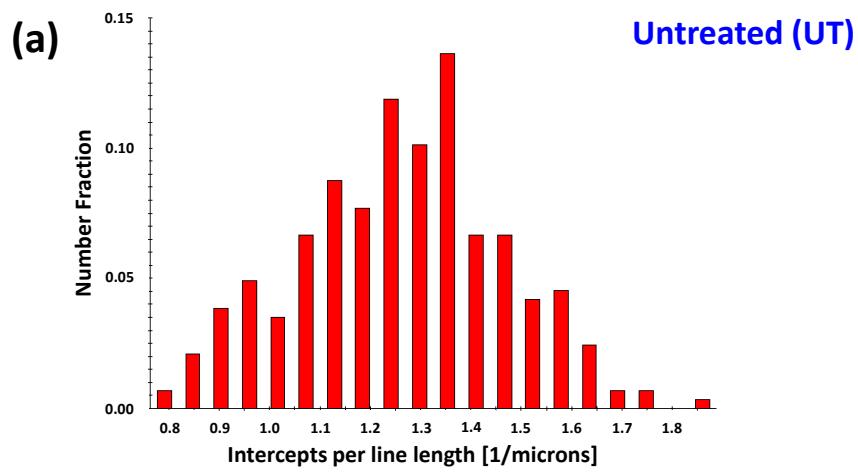
Figure 4.38 Grain size (Liner intercept) obtained for (a) Untreated, (b) LSM: 2.5 kW, and (c) LSM: 3 kW, X70 samples

4.3.4 *Analyses of corroded samples*

- **Scanning electron microscopy (SEM) analysis of corroded samples**

Figure 4.39(a-c) displays the surface morphologies of laser surface melted X70 samples as observed in SEM after FAC tests of only one electrode. All the given images represent the electrode E17 of different laser power sources of 2, 2.5, and 3 kW. Electrode E17 have exhibited the highest corrosion rate in all the laser power conditions. Comparatively more corrosion compounds were noticed on the surface of 3 kW electrode-E17 (Figure 4.39c), which has exhibited the highest corrosion rate. Whereas on the surface of 2.5 kW electrode-E17, relatively lesser corrosion compounds were formed. The corrosion resistance of 2.5 kW laser power electrodes is also better than 2 and 3 kW laser power electrodes. However, the corrosion products formed during the FAC test of LSM samples have better protection for the corrosion of substrate compared to the corrosion products formed on untreated samples under the same FAC condition (*see section 4.1.6*). Furthermore, all the electrodes were covered by little corrosion products.
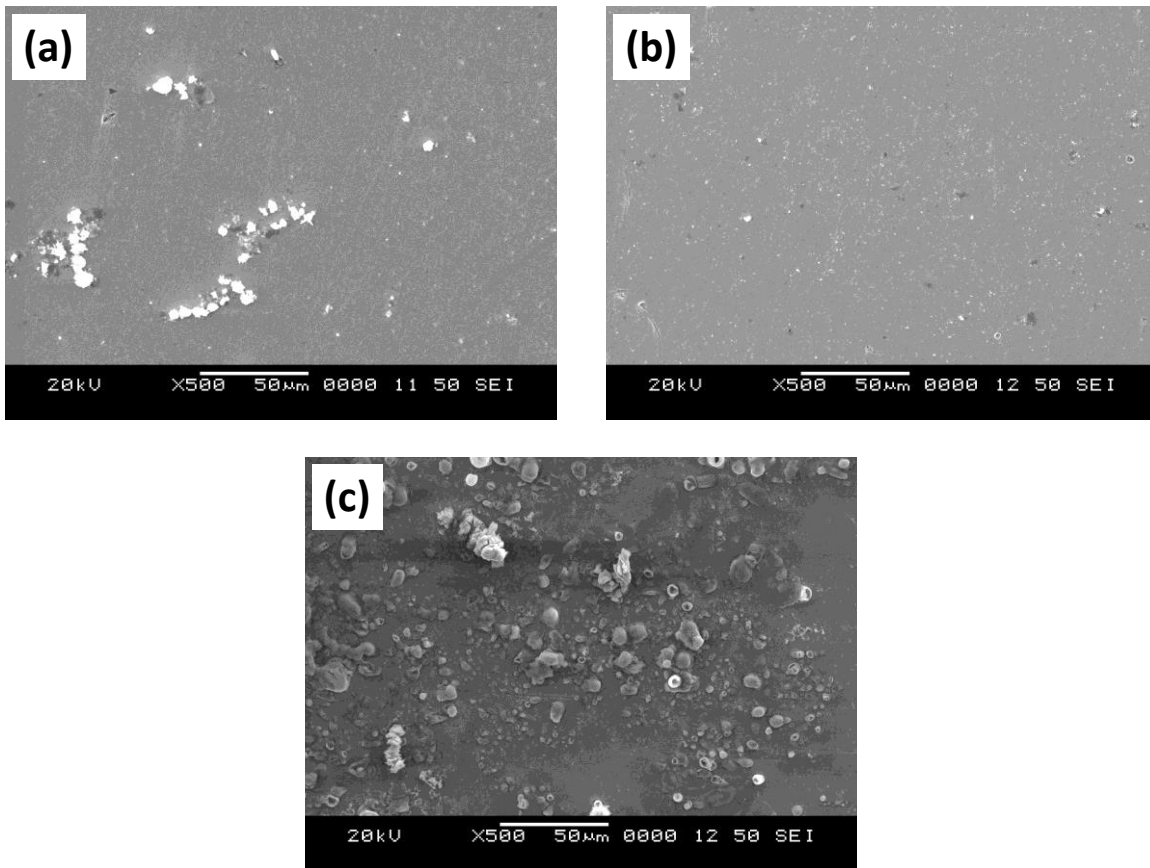
***Figure 4.39 SEM morphologies of laser surface melted (LSM) X70 samples
(electrode E17) after FAC experiments (a) 2 kW, (b) 2.5 kW, (c) 3 kW***

- **Raman spectroscopy analysis of corrosion products**

Figure 4.40 demonstrates the Raman spectrum of corrosion products formed on the representative electrode (E17) of 2.5 kW laser power, after the FAC test. Table 4.14 shows the measured Raman band frequencies for the corrosion products. The compositions of corrosion compounds formed by FAC were hematite α-Fe_2O_3 (227 cm^{-1}), maghemite γ-Fe_2O_3 (284 cm^{-1}), goethite α-FeOOH (387 cm^{-1}), wüstite FeO (595 cm^{-1}), and lepidocrocite γ-FeOOH (1307 cm^{-1}) (Guzonas et al. 1998; Hanesch 2009; Kiosidou et al. 2017; Thibeau et al. 1978). It is also clear that the characteristic peak at 227 cm^{-1} of α-Fe_2O_3 was strong.

118
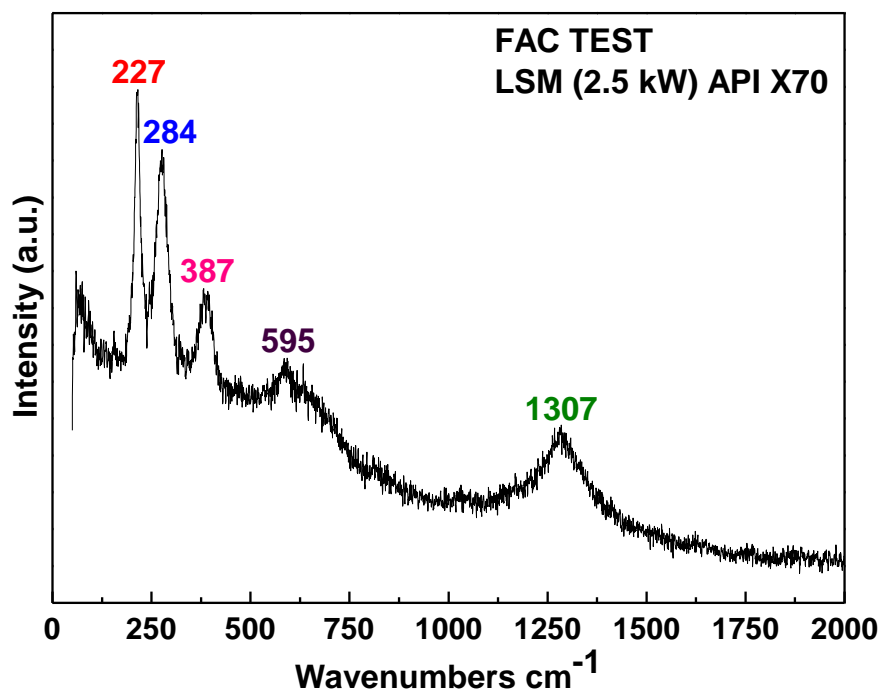
Figure 4.40 Raman spectrum of electrode E17 of 2.5 kW laser power followed by FAC

Table 4.14 Measured Raman band frequencies for corrosion products of a representative electrode (E17) of 2.5 kW laser power after FAC test (wavelength - 532 nm)

Raman bands (cm^{-1})	Phases Identified	References
227	α - Fe_2O_3	(Thibeau et al. 1978)
284	γ - Fe_2O_3	(Guzonas et al. 1998)
387	α - FeOOH	(Guzonas et al. 1998)
595	FeO	(Hanesch 2009)
1307	γ - FeOOH	(Kiosidou et al. 2017)

4.3.5   Discussion

Corrosion rates of laser surface melted (LSM) API X70 steel for selected electrodes are obtained by conducting potentiodynamic polarisation tests in simulated oilfield water. FAC study of untreated and LSM results suggest that the LSM samples resists the corrosion better than the untreated samples. It can be seen in Tafel plots that all the samples were susceptible to active dissolution under flow condition and anodic Tafel plots of the entire electrodes showed a higher corrosion current trend (Lopes-Sesenes et al. 2013). It is also noticed that the corrosion rates are more at FAC condition than at static condition. This is due to the effect of hydrodynamic parameters of the turbulent fluid flow (Jiang et al. 2005; Lopes-Sesenes et al. 2013; Vera et al. 2015).

FAC study of untreated and LSM samples suggests that the charge transfer resistances or polarization resistances are significantly higher for LSM samples as compared to UT. However, to see semicircle radius of the capacitive loop which is responsible for the charge transfer resistance (R_{ct}) is smaller in FAC conditions as compared to static (Lopes-Sesenes et al. 2013). It is indicating that higher metallic dissolutions were taken place during flow condition as compared to the static corrosion tests. This change is mainly due to the removal of the protective passive layer by the fluid flow.

The key factor for the improvement in corrosion resistance of X70 samples is microstructural surface modification. Corrosion is predominantly galvanic in nature, which depends on the inhomogeneous microstructural features of the metallic surfaces. The microstructural examination is exhibited not only the ferrite phase is transformed into the martensite with reduced crystallite size (grain refinement) but also structural defects (such as micropores, microcracks, and inclusions) were completely eliminated by the rapid heating and solidification process associated with the LSM process of X70 steel with low carbon content (Mudali and Dayal 1992; Zhao et al. 2016). It can enhance corrosion resistance by eradicating the chances of micro galvanic cell formation. Interestingly, the grain-boundary elemental segregation that occurred during the LSM process is also beneficial for the corrosion resistance, which can support the protective passive film formation on the steel surface (AlMangour et al. 2019; Alves et al. 2001). From the microhardness test results, it is clear that the laser melted sample has a higher

hardness value as compared to the untreated sample which matches the hardness value of the martensite phase (Agarwal et al. 2014; Kayali and Anaturk 2013). Hence, the high corrosion resistance of laser melted X70 steel is credited due to the homogeneous, refined, and single-phase (martensite) microstructure. In contrast to that, the composite, and heterogeneous (Ferrite and Pearlite) microstructure with lesser surface hardness resulted in relatively low corrosion resistance of untreated X70 steel (Lu and Luo 2015; Ralston and Birbilis 2010; Ravikumar and Kumaran 2018; Tang et al. 2004a; b; Zhao et al. 2016).

The corrosion rate and charge transfer resistance of the samples tested under FAC condition depend on the hydrodynamic parameter, wall shear stress. At the extrados (outer face) the wall shear stress and flow velocity are less compared to intrados (inner face) of the elbow test section. Because of that, the electrodes placed at intrados underwent more degradation compared to extrados electrodes. Therefore, it infers that the FAC experimental results are validating the CFD simulation results. Furthermore, the SEM images of corroded samples indicate that relatively lesser corrosion products are formed on the LSM samples. Among the LSM samples, comparatively lesser corrosion products were formed on the 2.5 kW laser power treated sample. The corrosion compounds formed on the representative sample E17 of 2.5 kW laser power were also identified using Raman spectroscopy analysis.

Figure 4.41 shows a comparison chart of polarization resistances (R_p or R_{ct}) values obtained from flow accelerated corrosion (FAC) studies. It is found that the use of OAH inhibitor (0.30 g/L) and surface engineering by laser surface melting (2.5 kW laser power) are very effective methods to improve the FAC resistance in the oilfield water solution. LSM resulted in significant improvement in FAC resistance of X70 steel.
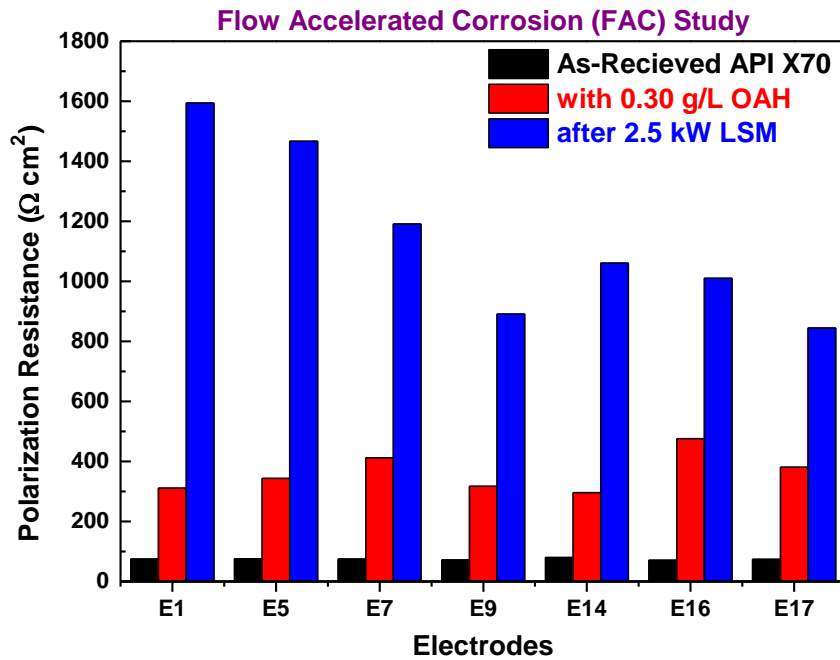
Figure 4.41 Comparison of polarization resistances (Rp) obtained from FAC tests

4.3.6 Summary

The effect of laser surface melting - LSM (laser powers 2, 2.5, and 3 kW) on API X70 steel was studied in static and dynamic corrosive environments. A circulating flow loop system was utilized to imitate the flow through a pipe more realistically. The major findings of this study are given below.

- The static and dynamic (FAC) corrosion resistance of the X70 steel was significantly improved by the laser surface melting (LSM) process. The corrosion rate of the LSM samples under flow condition is in the range of 10-50 mpy, whereas for untreated steel it is 450-600 mpy.

- A slight variation in corrosion resistance of different laser power samples (2, 2.5, and 3 kW) is found. However, the 2.5 kW laser power sample exhibited better passivation and protective behavior than other treated steels.

- Surface metallurgy alteration of the X70 steel due to the rapid heating and solidification that occurred during the LSM process is the prime reason for the improvisation of corrosion properties.

- Rapid melting and solidification processes associated with the LSM resulted in the formation of a homogeneous, refined, martensite microstructure on the X70 steel. This microstructural change led to the high FAC resistance of the LSM samples.

- The protective passive layer formation and FAC resistance improvement of the LSM samples benefited from the grain-boundary microalloying elemental segregation and grain refinement that occurred during rapid melting and solidification.

- FAC is varied for different samples positioned at various locations. Particularly, severe FAC occurred on the samples located at the intrados (inner face) side of the elbow test section. This is mainly due to the higher wall shear stress and flow velocity at the intrados of the pipe elbow.

- Corroded sample surfaces were analyzed with the help of SEM and Raman spectroscopy methods. SEM analysis suggests that lesser corrosion products were formed on the 2.5 kW laser power electrode compared to other LSM and UT samples.

- LSM treated X70 steel exhibited higher corrosion resistance than untreated and inhibitor-used conditions.

4.4 Slurry erosion-corrosion (EC) study of API X70 steel for UT and LSM

The presence of sand particles in the oilfield water leads to the erosion-corrosion (EC) of pipelines. It is a serious threat to pipeline integrity and sustainability. The synergetic effect of electrochemical reaction and mechanical erosion on UT and LSM X70 steel is needed to be studied. The effect of laser surface melting – LSM (laser powers 2, 2.5, and 3 kW) on erosion-corrosion resistance of X70 steel was analyzed with the circulating flow loop system. The electrolyte used in this study was the simulated oilfield water with the presence of sand particles (average size of 400-500 µm and sand loading of 1.5 wt.%) which was circulating with a flow velocity of 3 m s^{-1}. These tests were carried out for both the untreated and laser surface melted X70 steel samples, which were assembled at the 90º elbow test section. Seven samples were selected and located at extrados (E1, E5, E7, and E9) and intrados (E14, E16, and E17) of the 90º elbow test section. Both electrochemical and weight loss measurements were conducted for assessing erosion-corrosion behavior of UT and LSM X70 steel. Computational fluid dynamic (CFD) simulations were also performed to understand the synergetic effect of corrosion and wear in the presence of corrosive fluid and erodents under flow condition. Corrosion products and surface topographies were analyzed after the EC test with the help of advanced characterization tools such as Raman spectroscopy, atomic force microscopy (AFM), and optical profilometry.

4.4.1 Weight loss measurement

Erosion-Corrosion (EC) rates were obtained from the weight loss measurements at the end of 14 h of EC test in the loop system under oilfield water and sand particles are circulated. Table 4.15 shows the EC rates of untreated and laser surface melted at the laser powers of 2, 2.5, and 3 kW for X70 samples which are located at various angles (azimuthal angle φ and polar angle θ) of the elbow test section. To examine the results, it is observed that the laser melted steel samples are more resistant to erosion-corrosion as compared to untreated samples. However, 2.5 kW treated electrodes show higher erosion-corrosion resistance over 2 and 3 kW. The EC rates of extrados (outer face) electrodes such as E1, E5, E7, and E9 are more compared to intrados (inner face) electrodes such as E14, E16, and E17. EC rates of these electrodes are increasing along the flow direction (from $\theta = 90°$ to $\theta = 0°$). Further, it is noticed that the extrados

electrode E9 ($\varphi = 180°$, $\theta = 15°$) is exhibited the highest EC rate for all the tests, whereas the lowest is found for intrados electrode E17 ($\varphi = 0°$, $\theta = 45°$). Extrados electrode E9 can be seen that is located at the downstream side of the elbow test section, and the EC rate is 550 µg/ (cm^2.h), whereas the innermost electrode E17 shows the EC rate of 413 µg/ (cm^2.h). This variation in EC rates within the elbow test section could be due to the fluctuations in the hydrodynamic parameters and differences in erodent particle concentration at various locations which is reported by Zeng et al. (2014) for the steel X65 (Zeng et al. 2014).

Table 4.15 Erosion-Corrosion (EC) rates [µg/ (cm^2.h)] of untreated and laser surface melted (laser powers 2 kW, 2.5 kW, 3 kW) API X70 samples

Azimuthal Angle (φ)	Polar Angle (θ)	Electrodes	Erosion-Corrosion (EC) rate, µg/ (cm^2.h)			
				Laser Surface Melted		
			Untreated	2	2.5	3
				kW		
Extrados (Outer face) 135° (Column A)	72°	E1	641	488	479	493
180° (Column B)	75°	E5	652	504	502	507
	45°	E7	671	529	520	532
	15°	E9	723	566	550	586
Intrados (Inner face) 315° (Column D)	67.5°	E14	613	443	432	452
	22.5°	E16	627	466	461	475
0° (Column E)	45°	E17	595	425	413	438

4.4.2 Corrosion study under the influences of solution and sand particles

Tafel extrapolation tests were conducted to obtain the corrosion rates of untreated and laser surface melted X70 samples during the EC test. Figure 4.42(a-d) shows the Tafel plots of untreated and laser surface melted (2, 2.5, and 3 kW laser powers) X70 steel. The corrosion rates obtained from the Tafel plots are listed in Table 4.16. Untreated X70 samples were significantly prone to active metal dissolution, which led to higher corrosion rates as compared to treated (LSM) samples. This slow metal degradation rate of laser melted samples is directly controlled by microstructural transformation.

The variations in corrosion rates of the electrodes (samples) placed at different angular locations (azimuthal angle-φ, polar angle-θ) of the elbow test section are also noticed under the influence of sand particles. Corrosion resistances are lower at extrados electrodes (E1, E5, E7, E9) as compared to intrados electrodes (E14, E16, E17). The corrosion resistance of these electrodes is decreasing onward the fluid flow path (from θ = 90° to θ = 0°). The lowest corrosion resistance was found for extrados electrode E9 (φ = 180°, θ = 15°) which is located at the downstream side of the elbow whereas the highest resistance for innermost electrode E17 (φ = 0°, θ = 45°) during all the experiments. This dissimilarity in corrosion within the elbow test section is due to the variations in turbulent flow regime (Zeng et al. 2016b).

Furthermore, the laser melted samples of 2.5 kW (laser power) compared to 2 kW, and 3 kW samples show the lowest corrosion rates at each electrode location. The extrados electrode E9 of 2.5 kW laser power exhibits the highest corrosion rate of 18.9 mpy, whereas the innermost electrode E17 of it shows the lowest corrosion rate of 5.7 mpy. To see Figure 4.42a shows no change in plots. However, plots in 4.42b significantly varied anodic and cathodic curves due to surface inhomogeneity, and further 2.5 kW is a quite optimum power supply for surface modification.
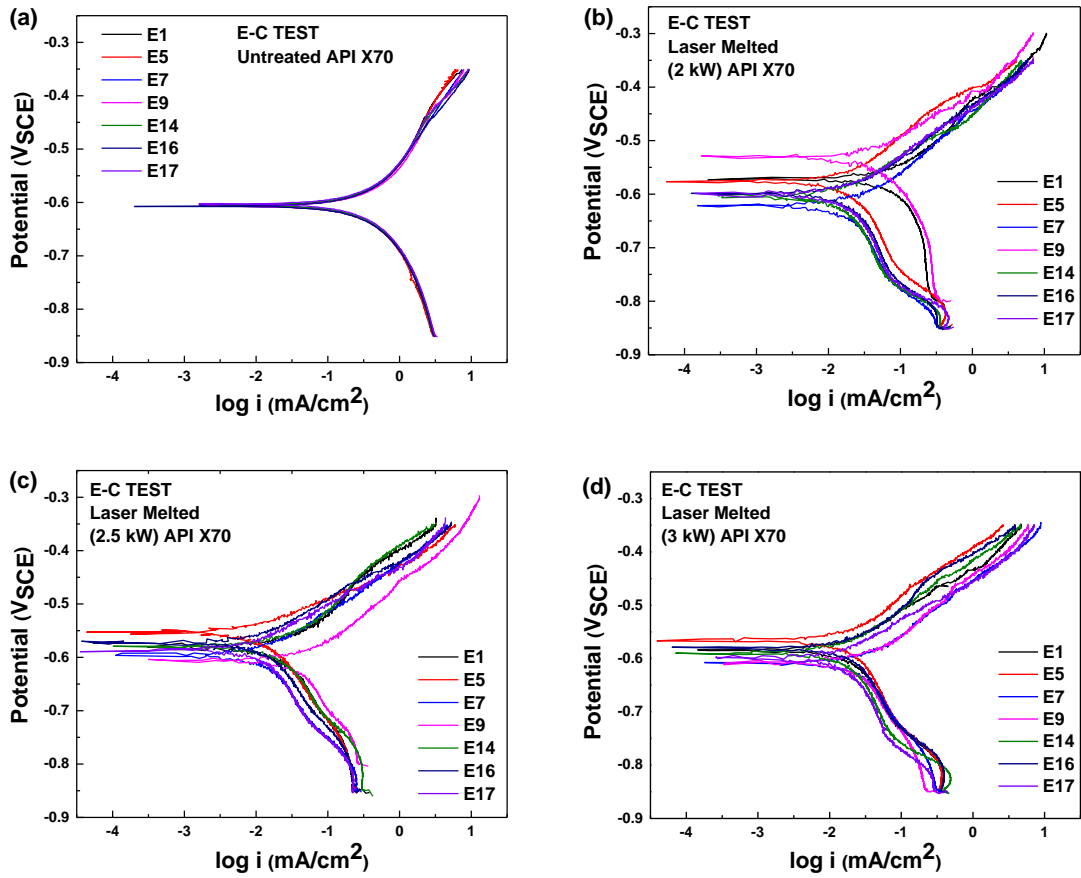
Figure 4.42 Tafel plots of EC tests of untreated and laser surface melted X70 steel samples (a) Untreated; for the laser powers (b) 2 kW, (c) 2.5 kW, (d) 3 kW

Table 4.16 Corrosion rates (mpy) of untreated and laser surface melted (laser powers 2 kW, 2.5 kW, 3 kW) API X70 samples

	Azimuthal Angle (φ)	Polar Angle (θ)	Electrodes	Corrosion Rate (mpy)			
					Laser Surface Melted		
				Untreated	2	2.5	3
						kW	
Extrados (Outer face)	135° (Column A)	72°	E1	230.0	8.6	8.0	9.6
	180° (Column B)	75°	E5	239.9	10.0	9.8	10.2
		45°	E7	248.8	14.9	13.2	15.7
		15°	E9	260.0	19.2	18.9	19.6
Intrados (Inner face)	315° (Column D)	67.5°	E14	209.4	7.1	6.2	7.6
		22.5°	E16	218.9	7.7	7.0	8.2
	0° (Column E)	45°	E17	201.8	6.7	5.7	6.1

4.4.3 Electrochemical impedance spectroscopy (EIS) test

The electrochemical impedance spectroscopy (EIS) technique was used to find out the passivation behavior of alloy during EC tests. Figure 4.43(a-d) displays the Nyquist plots of untreated and laser surface melted (2, 2.5, and 3 kW laser powers) X70 steel electrodes. The equivalent circuit shown in Figure 4.44 was used for fitting the experimental EIS data and calculation of its parameters. Here, the impedance parameters, R_s, CPE, and R_{ct} (= R_p) are solution resistance, constant phase element, charge transfer resistance, and polarization resistance, respectively. The charge transfer resistance (R_{ct}) values of each electrode are given in Table 4.17. Laser melted samples show higher charge transfer resistance (R_{ct}) compared to untreated steel. It clearly shows from the Nyquist plots that the capacitive loops are related to the interfacial charge transfer process at the electrode. Larger capacitive loop radii of Nyquist plots of the laser melted steel samples, and correspondingly higher R_{ct} values are the indication of a slow metal dissolution reaction rate (Du et al. 2009; Neville and Wang 2009; Zeng et al. 2015). It can be also seen the R_{ct} values are changing with the position of the electrode within the elbow test section. The R_{ct} values of extrados electrodes are less

compared to intrados electrodes and along the flow direction (from $\theta = 90°$ to $\theta = 0°$) it is decreasing. For all the tests, it is found that extrados electrode E9 ($\varphi = 180°$, $\theta = 15°$) have the lowest R_{ct} values whereas the highest is noticed for intrados electrode E17 ($\varphi = 0°$, $\theta = 45°$). Hydrodynamic behavior of multiphase flow might have led to the variation of charge transfer resistances within the elbow (Zhang et al. 2013). Among all the laser-treated X70 steel samples, 2.5 kW laser power electrodes show the highest R_{ct} values at each electrode location of the elbow test section. The extrados electrode E9 (laser power 2.5 kW) is exhibited the charge transfer resistance of 244.4 Ω cm^2, whereas the intrados electrode E17 of it shows the charge transfer resistance of 1333 Ω cm^2.
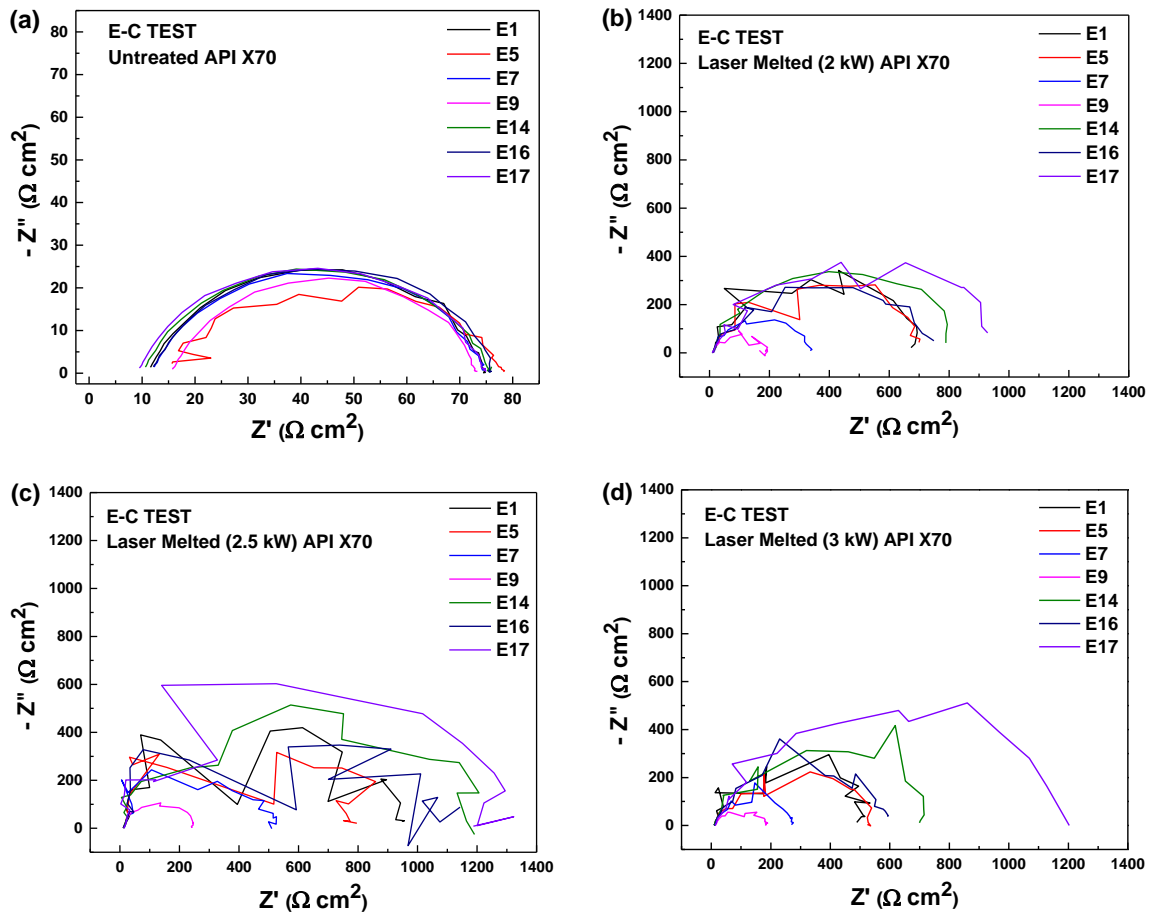
Figure 4.43 Nyquist plots of EC tests of untreated and laser surface melted X70 steel samples (a) Untreated; for the laser powers (b) 2 kW, (c) 2.5 kW, (d) 3 kW
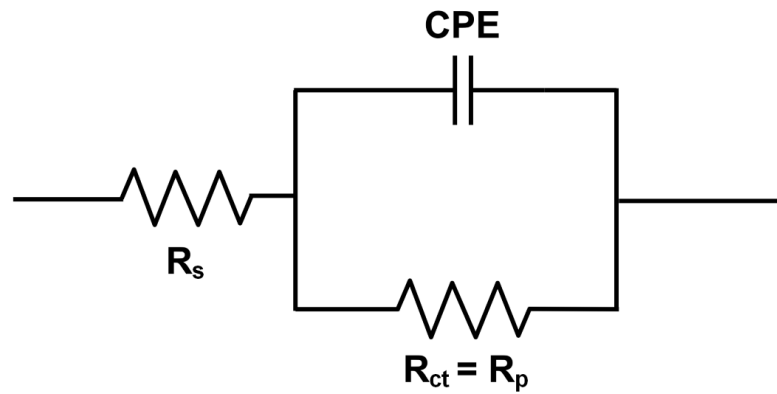
Figure 4.44 Equivalent circuit used for EIS plot fitting for EC tests

Table 4.17 Charge transfer resistances [R_{ct} (Ω cm^2)] of untreated and laser surface melted (laser powers 2 kW, 2.5 kW, 3 kW) X70 samples

	Azimuthal Angle (φ)	Polar Angle (θ)	Electrodes	Charge Transfer Resistance - R_{ct} (Ω cm^2)			
				Untreated	Laser Surface Melted		
					2	2.5	3
					kW		
Extrados (Outer face)	135° (Column A)	72°	E1	63.8	733.3	923.4	527.6
	180° (Column B)	75°	E5	63.3	723.0	793.5	526.6
		45°	E7	63.0	336.4	517.7	273.3
		15°	E9	57.8	173.6	244.4	171.4
Intrados (Inner face)	315° (Column D)	67.5°	E14	65.6	856.9	1183	751.5
		22.5°	E16	64.7	744.6	1012	595
	0° (Column E)	45°	E17	65.8	1013	1333	1279

4.4.4 Surface morphology of electrodes after EC test

Figure 4.45(a-d) shows the SEM surface morphologies of untreated and laser surface melted (2, 2.5, and 3 kW laser powers) X70 steel electrodes E9 (maximum EC rate) after 14 h of EC tests in the circulating loop system. Grooves and cutting marks appeared on the untreated surface by the movement of corrosive fluid with erodents (sand particles). However, laser-treated electrode surfaces show relatively fewer grooves and valleys over the untreated sample. It is only possible due to high-strength and hardened martensitic, fine grain microstructure which provides protection against erosion and corrosion by lessening the newer surface exposure. Also, it can be inferred that the 2.5 kW laser power electrode has relatively lower cutting marks. SEM analysis suggests that the laser surface melting could protect the steel surfaces from severe erosion-corrosion and material removal due to wear phenomena.
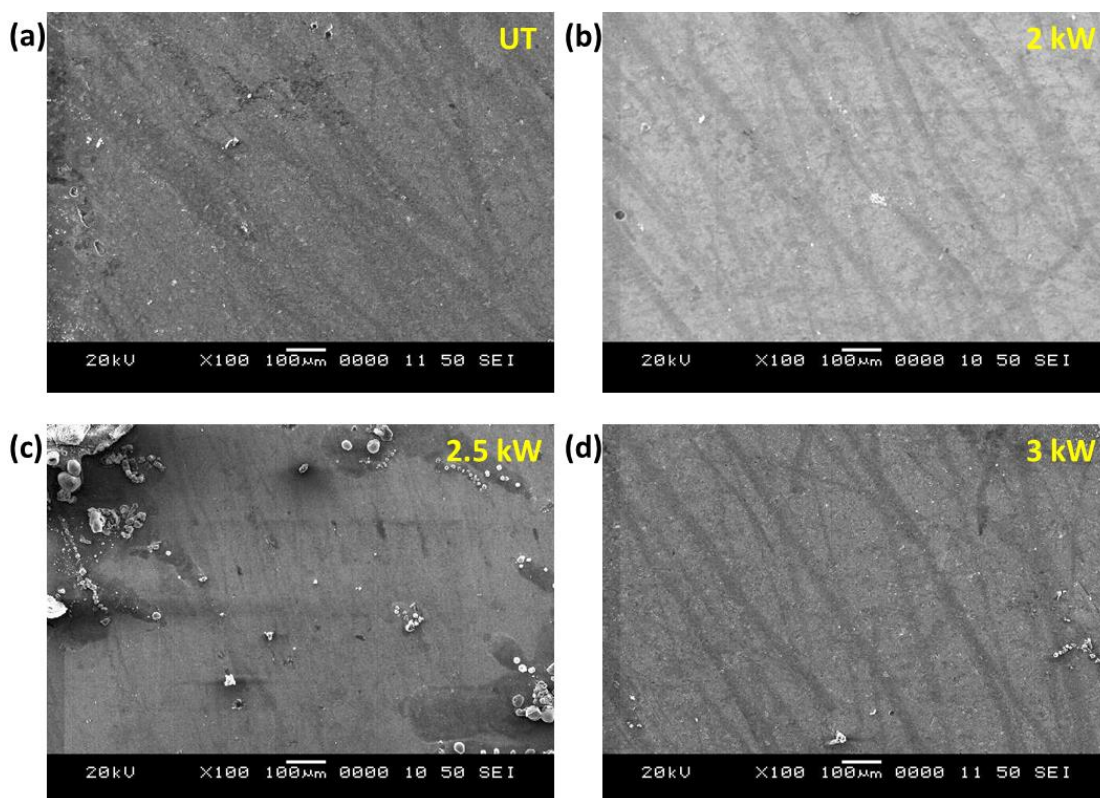
Figure 4.45 SEM morphologies of X70 samples (electrode E9) after EC tests (a) Untreated; for the laser powers (b) 2 kW, (c) 2.5 kW, (d) 3 kW

Figure 4.46 illustrates the Raman spectrum of corrosion products formed on laser-treated (2.5 kW laser power) X70 electrode E9 after the EC test. Table 4.18 shows the Raman band frequencies and phases identified for corrosion products formed on the sample surface after the EC test. It is seen that a sharp peak at the wavenumber of 248.29 cm^{-1}, confirms the presence of γ-FeOOH (lepidocrocite). Characteristic peaks at wavenumbers of 525.47 cm^{-1} and 1307.19 cm^{-1} are also due to the existence of γ-FeOOH. Other corrosion compounds formed on this sample surface were goethite - α-FeOOH (550.63 cm^{-1}), maghemite - γ-Fe$_2$O$_3$ (376 cm^{-1}), and hematite - α-Fe$_2$O$_3$ (655.34 cm^{-1}) (Guzonas et al. 1998; Kiosidou et al. 2017).

133
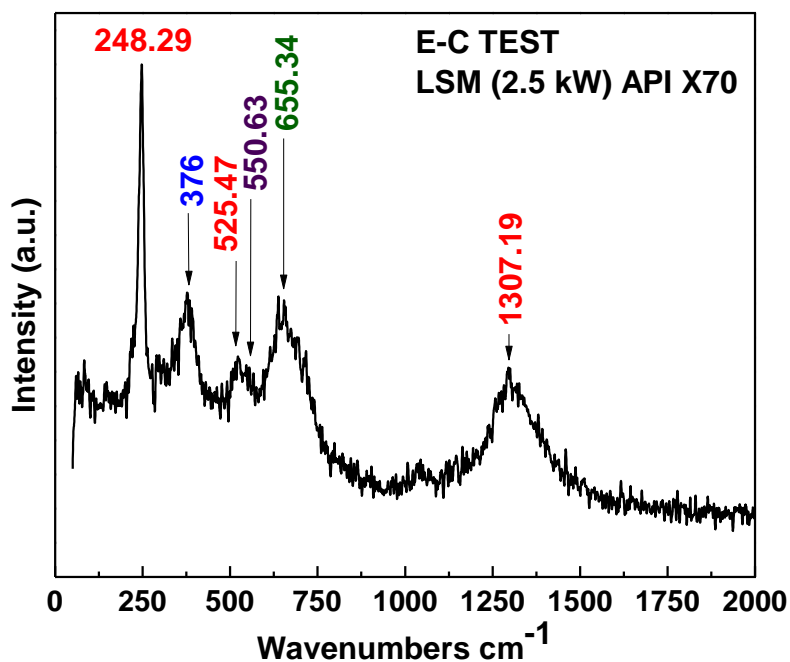
Figure 4.46 Raman spectrum of corrosion products formed on laser-treated (2.5 kW laser power) X70 sample (electrode E9) after EC test

Table 4.18 Raman band frequencies and phases identified for corrosion products formed on LSM (2.5 kW laser power) X70 sample (electrode E9) after EC test (wavelength of 532 nm)

Raman bands (cm^{-1})	Phases Identified	References
248.29, 525.47, 1307.19	γ-FeOOH	(Guzonas et al. 1998; Kiosidou et al. 2017)
550.63	α-FeOOH	
376	γ-Fe$_2$O$_3$	
655.34	α-Fe$_2$O$_3$	

4.4.5 Surface topography after the EC test

Figure 4.47(a-d) shows the 3D surface topographies of untreated and laser surface melted (2, 2.5, and 3 kW laser powers) X70 steel electrodes E9 (maximum EC rate) observed by Atomic force microscopy (AFM) after 14 h of EC tests. It is found that the untreated sample (Figure 4.47a), has more wavy surfaces than the laser-treated surfaces [Figure 4.47(b-d)] after the EC test. The untreated sample has got a rough surface with the presence of significant ridges and valleys in the range of 600 – 200 nm as against smoother worn surface of laser melted sample with relatively low crests and troughs. This smoother surface of the LSM samples further suggests that, during the EC test, relatively less material loss coupled with low metallic dissolution could have occurred due to the enhanced strength of the laser-melted surface. The 2.5 kW laser power electrode (Figure 4.47c) has a smoother surface compared to all other surfaces after EC tests. However, the impact of the synergetic effect of erosion and corrosion of erodent particles is quite low such that wear of fragile corrosion products could only contribute to wear and thus material removal occurred only to a nano-metric level of depth.
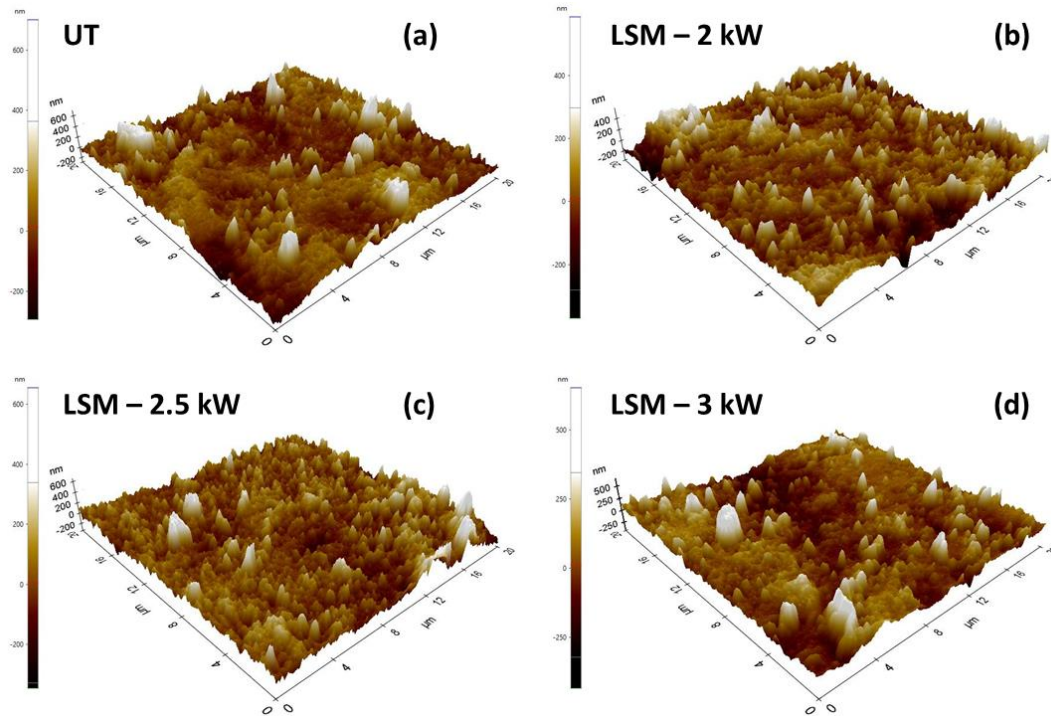
Figure 4.47 Atomic Force Microscopy (AFM); 3D surface topographies of X70 sample (E9) after EC tests (a) Untreated, for laser powers (b) 2 kW, (c) 2.5 kW, (d) 3 kW

Optical profilometry scans were performed to obtain 3D surface topographies and surface roughness parameters of the samples after 14 h of EC tests in synthetic oil field water with the presence of sand particles. The arithmetic mean height (Ra) and root-mean-square height (Rq) are the most significant surface roughness parameters (Dong et al. 1994; Grzesik et al. 2015; Pagani et al. 2017; Qi et al. 2015; Waikar and Guo 2008). The root-mean-square height provides information about the standard deviation of the height distribution, while arithmetic mean height is the mean surface roughness of the examined 3D surface topography (Elemuren et al. 2019).

Figure 4.48(a-d) displays the 3D surface topographies of worn electrode surfaces E5, E7, E9, and E17 of laser surface melted (2.5 kW laser power) X70 steel after EC tests. Roughness average (Ra) and root mean square (RMS) roughness (Rq) values are given in Table 4.19. It can be said that extrados electrodes (E5, E7, E9) are having deeper ridges and valleys than smoother intrados electrode (innermost) E17. Furthermore, among the extrados electrodes, more ridges and gullies (rougher surface) are present on the surface of electrode E9 ($\theta = 15°$, $\varphi = 180°$) which is located at the

136

downstream side of the elbow (Ra = 0.195 µm) and relatively smoother surface is for electrode E5 (θ = 75°, φ = 180°) which is located at the upstream side of the elbow (Ra = 0.156 µm). Electrode E9 has exhibited the highest EC rate also. Comparatively less ridges and valleys are formed on the intrados electrode E17 (θ = 45°, φ = 0°) (Ra = 0.142 µm) where the EC rate is also lowest.
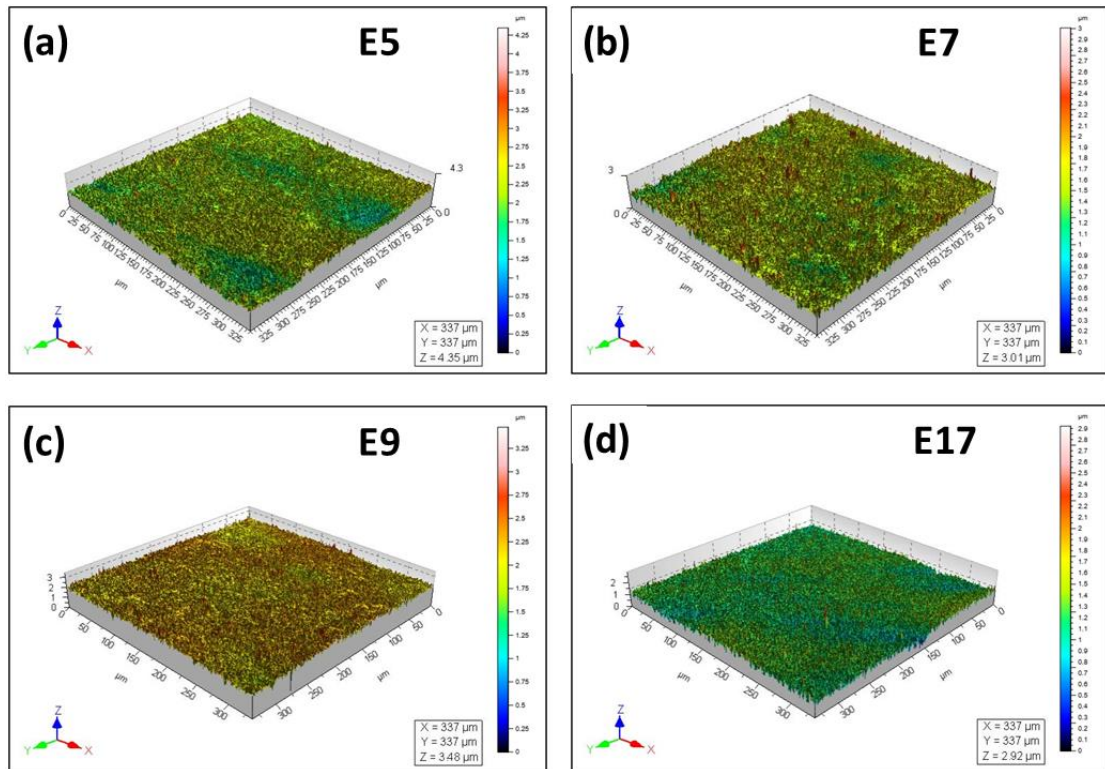
Figure 4.48 Surface topographies of LSM - X70 samples (2.5 kW laser power) after EC tests (a) E5 (b) E7, (c) E9, (d) E17, observed with an optical profilometer

Table 4.19 surface roughness parameters of the samples E5, E7, E9, and E17 of laser surface melted X70 steel (2.5 kW laser power) after 14 h EC test

Electrodes	Roughness Average Ra (µm)	Root Mean Square (RMS) roughness Rq (µm)
E5	0.156	0.217
E7	0.183	0.251
E9	0.195	0.279
E17	0.142	0.191

4.4.6 Computational fluid dynamics (CFD) simulation

From the experiments, it is understood that the EC rates of the samples fluctuate concerning the position of the electrodes within the elbow test section. CFD simulations are also performed to find out the causes of the differences in the EC behavior. Figure 4.49(a-d) illustrates the results of CFD simulations in the form of the contours of erosion rate, contours of sand concentration in cross-section, and secondary flow (vectors) in cross-section. From that, it is seen that the elbow wall is affected by different flow regimes and sand concentrations at various locations. Compared to intrados (inner face), the extrados (outer face) shows more erosion rate (Figure 4.49b). Remarkably, the erosion rate is gradually increasing along the fluid flow path (from $\theta = 90°$ to $\theta = 0°$). The downstream side (exit side, from $\theta = 45°$ to $\theta = 0°$) of the extrados exhibits the highest erosion rate. Moreover, there is an inertia effect of the fluid flow at the downstream side.

Figure 4.49c shows the cross-sectional views of sand concentrations along the flow path ($\theta = 90°$, $\theta = 45°$, and $\theta = 0°$). Sand concentration is more at the extrados side and a major contributor to enhance the erosion rate. Figure 4.49d displays the cross-sectional view of secondary flow developed at the elbow curvature, which will superimpose on its primary flow at the straight pipe section (Kim et al. 2014). This secondary flow is a general characteristic of fluid flow at the elbow (Zeng et al. 2014). A disproportion between centrifugal force and radial pressure gradient at the elbow leads to the generation of the secondary flow and flow separation effect. In this study, the curvature ratio, which is the ratio between the radius of curvature ($Rc = 83$ mm) and hydraulic diameter ($D = 48$ mm) of the elbow, is 1.73. Since the curvature ratio (Rc/D) is greater than 1.5, a swirling (twin-eddy) secondary flow is generated. This secondary flow containing a pair of counterrotating vortices modifies the velocity profile of primary axial flow and shifts its position from the center of curvature of the elbow to the outer core of the elbow (Dutta et al. 2016; Hellström et al. 2011; Shalaby 2018b; Weske 1948).

(a)

(b)

(c)

90°   45°   0°

(d)

90°   45°   0°
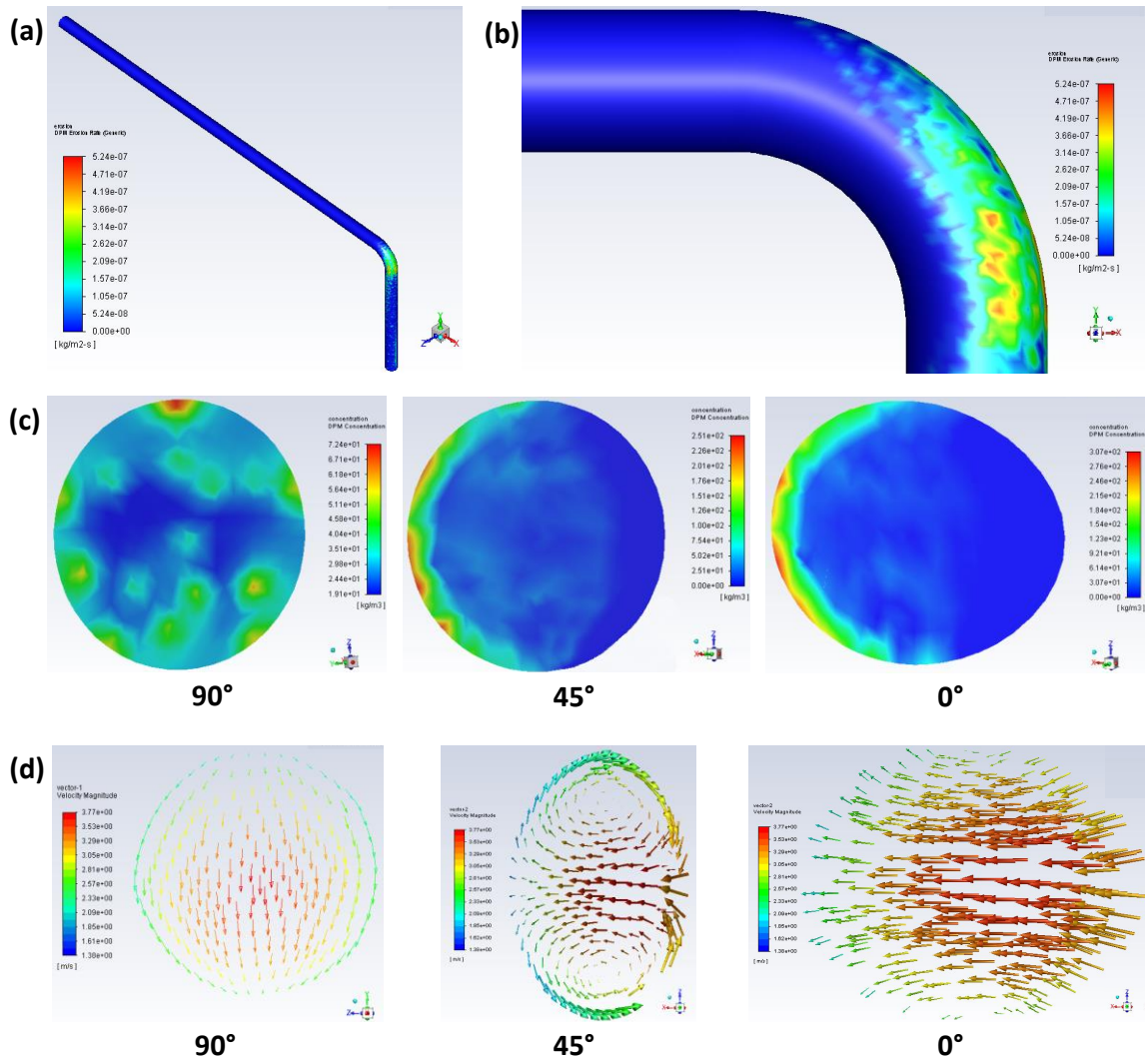
Figure 4.49 Computational Fluid Dynamics (CFD) simulation in 90° elbow test section (a) contours of erosion rate in 3D geometry, (b) contours of erosion rate, (c) contours of sand concentration in cross-section, (d) secondary flow (vectors) in cross-section

4.4.7 Discussion

For pipelines carrying oilfield water with sand particles, erosion-corrosion (EC) is a severe threat due to the combined effect of mechanical erosion and electrochemical corrosion processes. It can bring about more significant damage than the sum of the loss resulted from each process separately. EC led material degradation depends on several parameters, which act simultaneously. It can be either due to erosion-enhanced corrosion or corrosion-motivated erosion (Khayatan et al. 2018; Zeng et al. 2014; Zhao et al. 2016).

The EC rates (assessed from weight loss measurements) indicate that the laser melted steel (LSM) samples are more resistant to erosion-corrosion compared to untreated samples. The larger capacitive loop radii of Nyquist plots and higher R_{ct} values of the laser melted X70 steel are the indications of significant improvement in erosion-corrosion resistance in the simulated oilfield environment. Corrosion rates obtained by using Tafel plots of laser surface melted steel are quite lower over untreated due to refined martensitic microstructure, which is a key factor to stop or reduce EC or improvement of resistance against corrosion and erosion.

From Tafel plots, it is clear that the X70 steel electrodes undergo active dissolution under the oilfield slurry erosion-corrosion condition. Fluid flow intensifies the electrochemical reactivity by increasing the diffusion of iron species at the metal electrolyte interface (Kain 2014; Kain et al. 2011). The flow corrosion rate is directly related to the mass transfer process in the pipeline (Poulson 1999). As corrosion is principally an electrochemical process, the redox reactions occurring in the studied conditions include the anodic dissolution (Fe $\rightarrow$ Fe^{2+} + 2e$^-$) and cathodic reduction of oxygen (O$_2$ + 2H$_2$O + 4e$^-$ $\rightarrow$ 4OH$^-$) at the steel surface, as shown in Figure 4.50(a, b) (Sun et al. 2016; Zhang et al. 2011b). The metal ions may either enter the electrolyte as solvated metal ions or may remain on the surface to form a new solid phase as a short-time thin passivating film. This thin passivating oxide layer adheres to the steel surface and protects the steel from further corrosion by forming a protective barrier (of high impedance) to charge transfer (and thus corrosion) between the active steel surface and the corrosive fluid. This process of improvisation in corrosion resistance of the metal is also called pseudo passivation. The possible anodic and

cathodic reactions involved in the fore mentioned process can be described by the following equations (4.19-4.21).

$$Fe \rightarrow Fe^{2+} + 2e^{-} \tag{4.19}$$

$$O_2 + 2H_2O + 4e^{-} \rightarrow 4OH^{-} \tag{4.20}$$

$$2Fe + O_2 + 2H_2O \rightarrow 2Fe^{2+} + 4OH^{-} \tag{4.21}$$
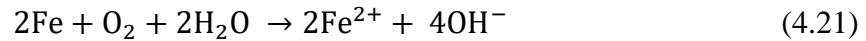
Fe^{2+} will react with OH^{-} and dissolved O_2 in the solution after that as specified in equations 4.22 and 4.23. Furthermore, γ-FeOOH (lepidocrocite), α-FeOOH (goethite), γ-Fe$_2$O$_3$ (maghemite), and α-Fe$_2$O$_3$ (hematite), which were detected as the significant corrosion products (film) from the Raman spectrum, yields from $Fe(OH)_3$, as detailed in equations 4.24 and 4.25.

$$Fe^{2+} + 2OH^{-} \rightarrow Fe(OH)_2 \tag{4.22}$$

$$4Fe(OH)_2 + O_2 + 2H_2O \rightarrow 4Fe(OH)_3 \tag{4.23}$$

$$2Fe(OH)_3 \rightarrow Fe_2O_3 + 3H_2O \tag{4.24}$$

$$Fe(OH)_3 \rightarrow FeOOH + H_2O \tag{4.25}$$
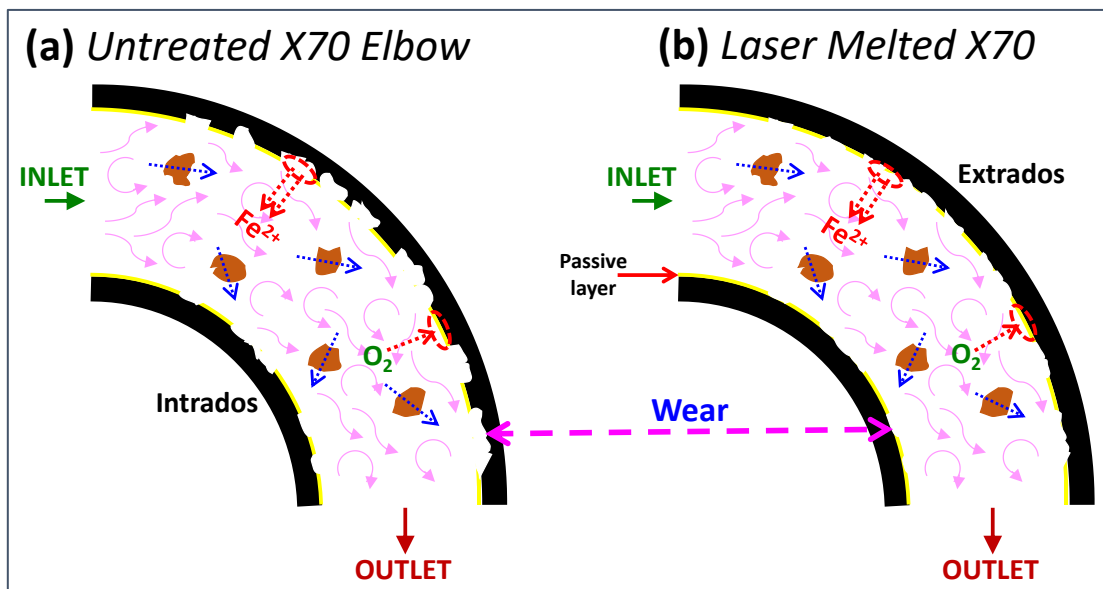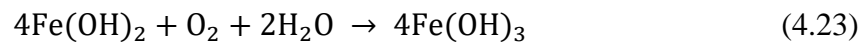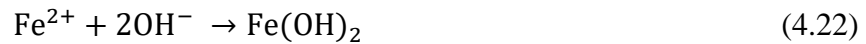
Figure 4.50 Erosion-corrosion mechanism of steel elbow enhanced by wear that depassivates the steel surface (a) EC at untreated elbow, (b) EC at LSM elbow

Slurry erosion-corrosion results in the removal of the protective passive film (depassivation) and the underlying bulk material from the sample surface by mechanical wear (particle erosion) as shown in Figure 4.50(a, b). Charge transfer process and the parent metal dissolution increase due to this mechanical removal and/or rupture of the passive layer and the succeeding exposure of the highly reactive parent material. As a result, local micro-galvanic cells between eroded (depassivated) and un-eroded (passive) locations might develop and promote easy material removal by mass transfer (Hodgkiess et al. 1999; Wood 2009). Improvement in surface hardness by laser surface melting (LSM) of steel reduces wear phenomena and so the erosion-corrosion phenomenon. Compared to the untreated steel surface, the LSM steel surface underwent less erosion by sand particles. Furthermore, the EDS study suggests that more alloying elements were segregated at the grain boundaries of the LSM sample surface, which will enhance the passive layer formation and therefore the corrosion resistance (AlMangour et al. 2019; Alves et al. 2001).

Major reasons for the performance in erosion-corrosion resistance of the laser surface melted X70 samples could be attributed to mainly microstructural changes with refinement and also improvement in surface hardness. Corrosion is predominantly galvanic, which depends on the microstructural features of the metallic surface. From the microstructural and hardness distribution analyses, it is clear that the ferrite phase is transformed into hard martensite with reduced crystallite size (grain refinement) due to the laser surface melting process. The reason for the grain refinement in the LSM sample is the rapid solidification and high cooling rate which increases the nucleation density with the reduction in growth rate, which leads to the formation of a greater number of fine grains (Vora and Dahotre 2013). In steels, reduction in grain size can reduce the susceptibility to corrosion due to the increased rates of diffusion in fine-grained microstructures, and improvement in passive film stability (Ralston and Birbilis 2010). Wang and Li (2003) studied the electrochemical properties of the nano-crystalline surface of the steel, and showed, that compared to samples with coarser grain size, fine-grained structures exhibited more rapid repassivation kinetics and formed more stable films (Wang and Li 2003). Structural defects such as micropores, microcracks, and inclusions were significantly eliminated

by the rapid heating and solidification associated with the laser surface melting and also low carbon content (Mudali and Dayal 1992; Zhao et al. 2016). From the microhardness test results, it is clear that the laser melted sample has a higher hardness value compared to the untreated sample which matches the hardness value of the martensite phase (Agarwal et al. 2014; Kayali and Anaturk 2013). The erosion-corrosion resistance and surface hardness can be organized in increasing order as: 220 HV – *(untreated)* < 312 HV – *(3 kW)* < 318 HV – *(2 kW)* < 330 HV – *(2.5 kW)*. Coupled with the above factor, hardness improvement due to martensitic transformation will further enhance the wear resistance of laser melted surface than softer untreated counterpart (Agarwal et al. 2014; Kayali and Anaturk 2013). Thus, erosion-corrosion resistance of laser melted X70 steel got transformed by a homogeneous, refined, and single-phase (Martensite) microstructure with enhanced surface hardness. In contrast, the presence of composite and heterogeneous (Ferrite and Pearlite) microstructure with less hardness in the untreated surface of X70 steel resulted in relatively low erosion-corrosion resistance (Lu and Luo 2015; Ralston and Birbilis 2010; Ravikumar and Kumaran 2018; Tang et al. 2004a; b; Zhao et al. 2016).

Figure 4.51 shows the comparison charts of EC rate, corrosion rate, and polarization resistance or charge transfer resistance obtained from EC tests of untreated and LSM (2.5 kW laser power) X70 steel samples. It is found that the difference in EC rates of untreated and LSM samples are less compared to the differences in corrosion rate and polarization resistance. It suggests that the influence of the sand particles on surface material removal or wear of X70 steel is not much significant. This is mainly because of the less sand concentration (1.5 wt.% sand loading) and relatively lower flow velocity (3 m s^{-1}) selected for this study. But at the same time, a huge improvement in corrosion properties is observed because of the surface metallurgical alteration which resulted in the formation of protective passive film formation. When the erodent particle's velocity and the flow rate are low, the associated impact of erodent particles would be mild (evident from the ridge-height and valley-depths). Thus, the EC rate could apparently follow the path of corrosion trailed by erosion of corroded products.
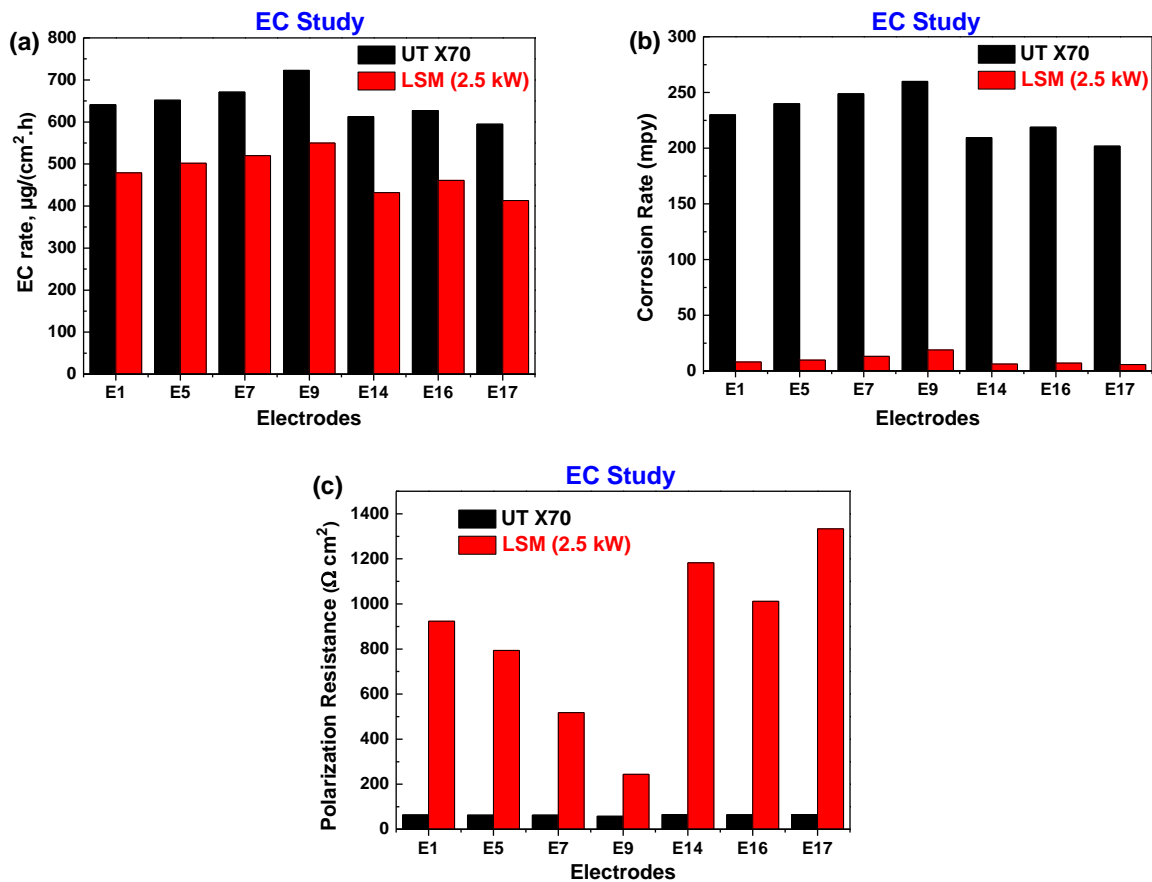
Figure 4.51 Comparison of (a) EC rate, (b) corrosion rate, and (c) polarization resistance after EC tests on untreated and LSM (2.5 kW) X70 steel

The variations in erosion-corrosion rate, charge transfer resistance (Rct), and the corrosion rate of the untreated and laser-treated X70 steel electrodes could also be associated with angular locations of the elbow test section as evident from Tables 4.15, 4.16, and 4.17. Within the elbow test section, these values were fluctuating concerning the positions of the electrodes. The extrados electrodes (E1, E5, E7, E9) were always prone to severe degradation or erosion-corrosion compared to intrados electrodes (E14, E16, E17) in all the tests conducted (Zeng et al. 2020). Furthermore, the erosion-corrosion of the electrodes were increasing along the direction of fluid flow (from $\theta = 90°$ to $\theta = 0°$). The extrados electrode E9 ($\varphi = 180°$, $\theta = 15°$) positioned at the downstream side of the elbow exhibited the highest erosion-corrosion, whereas the least is observed in the innermost electrode E17 ($\theta = 45°$, $\varphi = 0°$) for all the tests.

The results obtained from CFD simulations [Figure 4.49(a-d)] are in good agreement with the experimental results. From the contours of erosion rate, contours of sand concentration in cross-section, and secondary flow (vectors) in cross-section, it is clear that these flow properties are varying within the elbow test section. The erosion rate is more at the extrados (outer face) than at the intrados (inner face), and it is progressively increasing along the fluid flow path (from $\theta = 90°$ to $\theta = 0°$). The sand concentration (Figures 4.49c and 4.52a) was also more at the extrados, which could be one of the principal causes for the higher erosion-corrosion rate of the extrados electrodes. The cross-sectional view of secondary flow developed at the elbow curvature is presented in Figures 4.49d and 4.52b. Due to the secondary flow effect, a pair of counter-rotating vortices drive the slurry to the extrados, and then to the intrados, which leads to the higher erosion rates of extrados electrodes (Kim et al. 2014). Furthermore, the secondary flow is most energetic on the downstream side of the elbow (from $\theta = 45°$ to $\theta = 0°$). Therefore, from the CFD simulations, it is well understood that the differences in the EC behavior within the elbow are because of the differences in flow regimes and sand concentrations at various locations (Zeng et al. 2014, 2016a; Zhang et al. 2013).
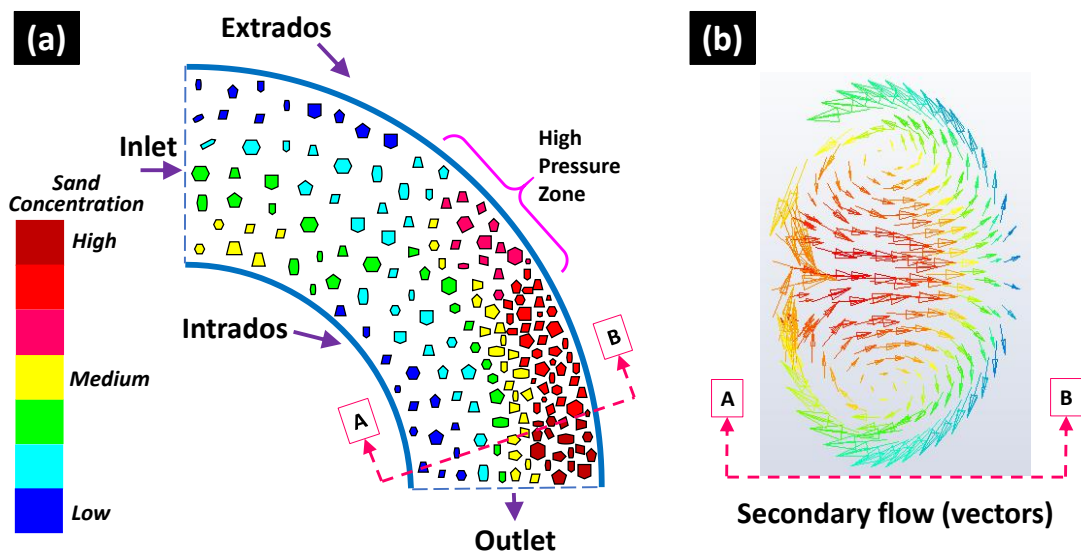
Figure 4.52 Schematic diagram of (a) Sand concentration at 90º elbow test section, and (b) Secondary flow (vectors) at the cross-section "AB"

The surface characterizations were carried out after EC tests in the circulating loop system. The SEM worn-surface morphologies [Figure 4.45(a-d)] of electrodes E9 with maximum EC rate demonstrate that relatively fewer grooves and valleys are formed on the laser-treated electrode surface. It suggests that laser surface melted samples were able to protect the steel substrate from severe erosion-corrosion and material removal due to wear. 3D surface topographies [Figure 4.47(a-d)] observed by Atomic Force Microscopy (AFM) also confirm that laser-treated samples show more protective behavior against erosion-corrosion in this aggressive corrosive environment. 3D surface topographies [Figure 4.48(a-d)] and surface roughness parameters (Table 4.19) of 2.5 kW laser power samples (E5, E7, E9, and E17) obtained from optical profilometry scans demonstrate that extrados electrodes (E5, E7, E9) are having more uneven surfaces with ridges and valleys compared to intrados electrode (innermost) E17. Among these electrodes, downstream side extrados electrode E9 ($\varphi = 180°$, $\theta = 15°$) shows more ridges and gullies and highest arithmetic mean height value (Ra = 0.195 µm), whereas the smoother surface and lowest Ra value is for the intrados electrode E17 ($\varphi = 0°$, $\theta = 45°$) (Ra = 0.142 µm).

4.4.8   Summary

The effect of erosion-corrosion (EC) on untreated and laser surface melted (LSM) API X70 steel samples was investigated with the help of a circulating loop system. This study reveals that the synergetic effect of electrochemical reaction, wear phenomena, and hydrodynamic parameters resulted in EC of X70 samples. Furthermore, the LSM samples were exhibited better EC resistance than untreated samples. The following major conclusions were made from this slurry erosion-corrosion study.

- From the weight loss measurements, electrochemical impedance spectroscopy (EIS), and Tafel extrapolation tests, it is clear that laser surface melted X70 samples have more erosion-corrosion resistance than the untreated counterpart.
- The major reasons for the improvement in erosion-corrosion resistance of laser surface melted samples are the alteration of surface metallurgy and the improvement in surface hardness.

- Rapid melting and solidification processes associated with the laser surface melting resulted in a homogeneous, refined, martensite microstructure. These microstructural changes with improved surface hardness led to high EC resistance of the LSM sample.

- The protective passive layer formation of the LSM samples benefited from the grain-boundary microalloying elemental segregation that occurred during rapid melting and solidification process led to significant EC resistance improvement.

- Furthermore, it observed that, within the elbow, erosion-corrosion was fluctuating for different samples positioned at various locations. Particularly, severe erosion-corrosion occurred on the samples located at the extrados (outer face) - downstream side of the elbow.

- From the results of CFD simulations, it was understood that the elbow wall was influenced by different flow patterns and sand concentrations at various locations of the elbow.

- CFD simulation suggests that the secondary flow effect and high sand concentration at the extrados (outer face) - downstream side of the elbow resulted in severe erosion-corrosion of the samples placed in that region.

- SEM surface morphologies, Atomic Force Microscopy (AFM) topographies, optical profilometry scans also supported the experimental and simulation results. More ridges and valleys were observed on the extrados electrode surfaces and less on LSM samples (compared to untreated samples) after EC tests.

5 CONCLUSIONS AND FUTURE WORK

5.1 Conclusions

Effect of flow accelerated corrosion (FAC) and erosion-corrosion (EC) on API X70 line pipe steel (90° pipe elbow) were studied in the oilfield environment. A loop system was utilized to imitate the flow through a pipe more realistically. To mitigate FAC and EC of X70 steel two different approaches were also investigated. One such method to mitigate FAC is the use of a green organic inhibitor (oleic acid hydrazide - OAH). Another method is the surface modification of X70 steel by laser surface melting (LSM). Computational fluid dynamics (CFD) simulation is also facilitated to understand the synergetic effect of hydrodynamics behavior of the fluid flow and electrochemical reactions.

- The study shows that API X70 steel exhibited a higher corrosion rate and reduced charge transfer resistance under flow (dynamic) condition over the static condition in the simulated oilfield environment. The turbulent fluid flow with high velocity and wall shear stress intensified the electrochemical reactivity and mass transfer process at the metal electrolyte interface by removing the protective passive films from the internal pipe wall repeatedly.

- Corrosion rate and corrosion current density at the intrados are more (charge transfer resistances at the intrados are less) as compared to the extrados and onward the flow path corrosion rate is increased. This variation in corrosion properties with respect to the position of the electrode is due to the fluctuations of the hydrodynamic parameters within the 90° pipe elbow.

- The electrochemical experimental results were in good agreement with the CFD simulation results.

- The performance of a green inhibitor, a fatty acid derivative, oleic acid hydrazide (OAH) is used in FAC condition at three different concentrations (0.05 g/L, 0.15 g/L, 0.30 g/L). It is found that OAH is good in the protection of the X70 steel with higher efficiency at 0.30 g/L concentration. The maximum inhibitor efficiency was found 87.7% at 0.30 g/L concentration. This protection is due to the formation of metal-inhibitor complexes by the adsorption behavior of the organic adsorbate on

the sample surface. The inhibition efficiencies of the X70 steel samples at the elbow test section are also changing with the positions due to the drastic changes in flow patterns.

- The effect of laser surface melting - LSM (laser powers 2, 2.5, and 3 kW) on API X70 steel was also studied. The corrosion resistance of the X70 steel was significantly improved by the laser surface melting (LSM) process due to the surface metallurgy alteration. Rapid melting and solidification processes associated with the LSM resulted in the formation of a homogeneous, refined, martensite microstructure on the X70 steel.

- The passive layer formation and FAC resistance improvement of the LSM samples benefited from the grain-boundary microalloying elemental segregation and grain refinement that occurred during rapid melting and solidification.

- To compare corrosion resistance in terms of polarization resistance of untreated, with OAH inhibitor (0.30 g/L) and LSM treated condition at 2.5 kW laser power, LSM treated steel exhibited the highest FAC resistance.

- Slurry erosion-corrosion tests were conducted on untreated and laser surface melted (LSM) X70 steel samples with the help of the circulating loop system. This study reveals that the synergetic effect of electrochemical reaction, wear phenomena, and hydrodynamic parameters resulted in erosion-corrosion of X70 steel. The LSM samples exhibit better EC resistance than the untreated counterpart after the transformation to harder, refined, homogeneous, martensitic microstructure by the LSM process.

- Erosion-corrosion also depends on the position or location of the samples within the elbow. Severe erosion-corrosion occurred on the samples located at the extrados (outer face) - downstream side region of the elbow due to the high sand concentration and secondary flow effect.

5.2   Suggestions for future work

The oilfield water or produced water contains dissolved gases such as H_2S and CO_2, which easily promote internal corrosion of the pipeline (Palacios 2016). Therefore, further studies can be carried out to analyze the effect of those gases on FAC and EC of *API 5L grade* steels in a loop system. Effect of other corrosion inhibitors which are effective under static conditions can be studied in FAC conditions using the loop system. There is a scope for a detailed study on the effect of laser processing parameters on *API 5L grade* steels and their effect on FAC and EC.

APPENDIX

- **DETAILED CALCULATIONS**

- **Density (ρ) of the oilfield water**

The density (ρ) is an elementary physical property of a matter. For a homogeneous object, it is defined as the ratio of its mass (m) to its volume (V). It was determined using a method specified in ASTM D1217 (ASTM D1217 2016) using the equation given below.

Density, $\rho = \dfrac{m}{V} = \dfrac{25.7611}{25} = 1.0304$ g cm^{-3} = **1030.4** kg m^{-3}

where: Mass of empty pycnometer, $m_0 = 22.8364$ g

Mass of pycnometer with oilfield water, $m_1 = 48.5975$ g

Mass of oilfield water, $m = m_1 - m_0 = 25.7611$ g

Volume of oilfield water, $V = 25$ ml

- **Kinematic viscosity (v) of the oilfield water**

The kinematic viscosity (v), was calculated from the measured flow times (t), and the viscometer constant (C), using the equation given below. It was determined by using a method specified in ASTM D445 (ASTM D445 2016).

Kinematic viscosity, $v = C \times t = 0.0097$ mm^2 s^{-2} $\times$ 74 s $= 0.7178$ mm^2 s^{-1}

where: C - calibration constant of the viscometer, mm^2 s^{-2}

t - measured flow times, s

- **Dynamic (absolute) viscosity (μ) of the oilfield water**

The dynamic viscosity (μ) was calculated from the calculated kinematic viscosity (v), and the density (ρ), using the equation given below.

Dynamic viscosity, $\mu = v \times \rho \times 10^{-3} = 0.7178 \times 1030.4 \times 10^{-3} = 0.74$ mPa.s

$= 0.00074$ Pa. s (or) Ns m^{-2} (or) kg m^{-1} s^{-1}

where: ρ - density, kg m^{-3}

v - kinematic viscosity, mm^2 s^{-1}.

- **Reynolds number (R_e) of the fluid flow**

To classify the type of flow through the loop system, the Reynolds number (R_e) was calculated using the equation given below (Murdock 2006).

$$\text{Reynolds number, } R_e = \frac{inertia\ forces}{viscous\ forces} = \frac{\rho VD}{\mu} = (1030.4 \times 3 \times 0.048) / 0.00074$$

$$= \textbf{200613}$$

Where: V - average velocity, 3 m s^{-1}

D - Pipe internal diameter or Hydraulic diameter, 0.048 m

ρ – Oilfield water density, 1030.4 kg m^{-3}

μ - Dynamic (absolute) viscosity, 0.00074 Ns m^{-2}

- **Entrance length (L_e) for the elbow test section**

For a turbulent fluid flow, the entrance length is 50 times the hydraulic diameter (D) (Shalaby 2018a).

Entrance length, $L_e = 50D = 50 \times 0.048$ m = **2.4 m**

- **Turbulent intensity (I) of the fluid flow**

Turbulent intensity (I) was calculated from the Reynolds number (R_e) using the equation given below (Zeng et al. 2016b).

Turbulent intensity, $I = 0.16 \times (R_e)^{-1/8} = 0.16 \times (200613)^{-1/8} = 0.03477 = \textbf{3.5\%}$

- **Sand particle density (ρ)**

Density is defined as the ratio of its mass (m) to its volume (v). The density (ρ) of the sand particles was measured by the volume replacement method using the equation given below.

$$\text{Density of the sand particles } (\rho) = \frac{m}{V} = \frac{5}{2.32288} = 2.153 \text{ g cm}^{-3} = \textbf{2153 kg m}^{-3}$$

Where: Mass of the sand particles = 5 g

Density of the water at 25 ml $= \frac{m}{V} = \frac{24.792}{25} = 0.992$ g cm^{-3}

Mass of the water and sand at 25 ml = 27.860 g

Mass of water = 27.860 – 5 = 22.860 g

Volume of water = 22.860 × 0.992 = 22.67712 ml

Volume of sand particles = 25 – 22.67712 = 2.32288 ml

- **Mass flow rate of sand particles (ω)**

The calculation of the mass flow rate of sand particles was done based on sand loading (1.5 wt.%) of the erosion-corrosion test using the equation given below (Shook and Roco 1991).

Mass flow rate (ω) $= \rho AV \times \frac{1.5}{100} = (2153 \times 0.00180955 \times 3) \times \frac{1.5}{100} = 0.175$ kg s^{-1}

Where: ρ – sand particle density = 2153 kg m^{-3}

A – cross-sectional area of pipe $= \pi \times (\text{radius})^2 = 3.14 \times (0.024)^2 = 0.00180955$ m^2

V – average fluid flow velocity = 3 m s^{-1}

REFERENCES

Agarwal, N., Chaudhari, G. P., and Nath, S. K. (2014). "Slurry and cavitation erosion of HSLA steel processed by warm multidirectional forging and inter-critical annealing." *Tribol. Int.*, 70, 18–25.

Ahmad, Z. (2006). "Corrosion Control by Inhibition." *Princ. Corros. Eng. Corros. Control*, Oxford, UK: Elsevier, 352–381.

Ahmed, W. H. (2012). "Flow Accelerated Corrosion in Nuclear Power Plants." *Nucl. Power Pract. Asp.*, W. H. Ahmed, ed., Rijeka, Croatia: InTech, 153–178.

Ajmal, T. S., Arya, S. B., and Udupa, K. R. (2019). "Effect of hydrodynamics on the flow accelerated corrosion (FAC) and electrochemical impedance behavior of line pipe steel for petroleum industry." *Int. J. Press. Vessel. Pip.*, 174(March), 42–53.

Alaneme, K. K., Olusegun, S. J., and Adelowo, O. T. (2016). "Corrosion inhibition and adsorption mechanism studies of Hunteria umbellata seed husk extracts on mild steel immersed in acidic solutions." *Alexandria Eng. J.*, 55(1), 673–681.

Alizadeh, M., and Bordbar, S. (2013). "The influence of microstructure on the protective properties of the corrosion product layer generated on the welded API X70 steel in chloride solution." *Corros. Sci.*, 70, 170–179.

AlMangour, B., Kim, Y. K., Grzesiak, D., and Lee, K. A. (2019). "Novel TiB2-reinforced 316L stainless steel nanocomposites with excellent room- and high-temperature yield strength developed by additive manufacturing." *Compos. Part B Eng.*, 156(April 2018), 51–63.

Alves, V. A., Brett, C. M. A., and Cavaleiro, A. (2001). "Influence of heat treatment on the corrosion of high speed steel." *J. Appl. Electrochem.*, 31(1), 65–72.

Ameh, P. O., Kolo, A. M., Ahmed, A., and Ajanaku, I. K. (2017). "Electrochemical study of the corrosion inhibition of Delonix regia for mild steel in sulphuric acid medium." *J. Ind. Environ. Chem.*, 1(1), 15–21.

Anderhalt, R. (2007). "X-ray Microanalysis in Nanomaterials." *Scanning Microsc. Nanotechnol.*, W. Zhou and Z. L. Wang, eds., New York, USA: Springer, 76–

100.

Anderson, J. M., and Voskerician, G. (2010). "The challenge of biocompatibility evaluation of biocomposites." *Biomed. Compos.*, L. Ambrosio, ed., Oxford, UK: Woodhead Publishing, 325–353.

API 5L. (2018). *Line Pipe, API SPECIFICATION 5L FORTY-SIXTH EDITION*. Washington, DC: American Petroleum Institute.

Ashassi-Sorkhabi, H., and Asghari, E. (2008). "Effect of hydrodynamic conditions on the inhibition performance of l-methionine as a 'green' inhibitor." *Electrochim. Acta*, 54(2), 162–167.

ASTM. (2014). "ASTM E415-14: Standard Test Method for Analysis of Carbon and Low-Alloy Steel by Spark Atomic Emission Spectrometry." *ASTM Int.*, (April 1999), 1–13.

ASTM D1217, 15. (2016). *Standard Test Method for Density and Relative Density (Specific Gravity) of Liquids by Bingham Pycnometer*. West Conshohocken, PA: ASTM International.

ASTM D445, 15a. (2016). *Standard Test Method for Kinematic Viscosity of Transparent and Opaque Liquids (and Calculation of Dynamic Viscosity)*. West Conshohocken, PA: ASTM International.

ASTM G1, 03. (2003). *Standard Practice for Preparing, Cleaning, and Evaluating Corrosion Test Specimens*. West Conshohocken, PA: ASTM International.

ASTM G3, 13. (2013). *Standard Practice for Conventions Applicable to Electrochemical Measurements in Corrosion Testing*. West Conshohocken, PA: ASTM International.

Avner, S. H. (1997). "The Heat Treatment of Steel." *Introd. to Phys. Metall.*, S. H. Avner, ed., New York: Tata McGraw-Hill, 256–260.

Barceló, D., and Farré, M. (2012). "Introduction to the Analysis and Risk of Nanomaterials in Environmental and Food Samples." *Compr. Anal. Chem.*, Elsevier, 1–32.

Barker, R., Hu, X., Neville, A., and Cushnaghan, S. (2013). "Inhibition of flow-induced corrosion and erosion-corrosion for carbon steel pipe work from an offshore oil and gas facility." *Corrosion*, 69(2), 193–203.

Basha, S. S., Periasamy, V. M., Kamaraj, M., and Shariff, S. M. (2013). "Improvement of slurry erosion wear resistance of 16Cr-5Ni martensite stainless steel by LSA and LTH." *J. Mater. Eng. Perform.*, 22(12), 3689–3698.

Benarrache, S., Benchatti, T., and Benhorma, H. (2019). "Formation and Dissolution of Carbides and Nitrides in the Weld Seam of X70 Steel by the Effects of Heat Treatments." *Ann. Chim. - Sci. des Matériaux*, 43(1), 11–16.

Bhadeshia, H. K. D. H., and Honeycombe, R. W. K. (2017). *Steels: Microstructure and Properties*. Cambridge, United States: Butterworth-Heinemann (Elsevier).

Bindu, P., and Thomas, S. (2014). "Estimation of lattice strain in ZnO nanoparticles: X-ray peak profile analysis." *J. Theor. Appl. Phys.*, 8(4), 123–134.

Bruice, P. Y. (2014). "Identification of Organic Compounds." *Org. Chem.*, J. Jaworski, A., Zalesky, ed., Pearson Education, Inc., 594–648.

Callister Jr., W. D., and Rethwisch, D. G. (2014). "Phase Transformations." *Mater. Sci. Eng. An Introd.*, D. Sayre, ed., 111 River Street, Hoboken, NJ: John Wiley & Sons, Inc., 376–378.

Carboni, C., Peyre, P., Béranger, G., and Lemaitre, C. (2002). "Influence of high power diode laser surface melting on the pitting corrosion resistance of type 316L stainless steel." *J. Mater. Sci.*, 37(17), 3715–3723.

Carter, J., Dawson, P., and Nixon, R. (2006). "Explosion at the Conoco Humber Refinery - 16TH April 2001." *IChemE J. LPB*, 14–20.

Cervantes-Tobón, A., Díaz-Cruz, M., González-Velázquez, J. L., and Godínez-Salcedo, J. G. (2014). "Effect of corrosion products formed and flow rate over the surface of steels API 5L X-52 and X-70 on the rate of corrosion in brine added with kerosene and H2S." *Int. J. Electrochem. Sci.*, 9(5), 2254–2265.

Cervantes Tobón, A., Díaz Cruz, M., Domínguez Aguilar, M. A., and González Velázquez, J. L. (2015). "Effect of flow rate on the corrosion products formed on traditional and new generation API 5L X-70 in a sour brine environment." *Int. J. Electrochem. Sci.*, 10(4), 2904–2920.

Cotell, C. M., and Sprague, J. A. (1994). *Surface Engineering (Vol. 5)*. Materials Park, OH: ASM International.

Cullity, B., and Stock, S. (2001). *Elements of X-Ray Diffraction*. London: Pearson Education, Inc.

Davis, J. R. (2001). *Surface Engineering for Corrosion and Wear Resistance*. (J. R. Davis, ed.), Materials Park, OH: ASM International.

Deardo, A. J. (2003). "Niobium in modern steels." *Int. Mater. Rev.*, 48(6), 371–402.

Dong, W. P., Sullivan, P. J., and Stout, K. J. (1994). "Comprehensive study of parameters for characterising three-dimensional surface topography." *Wear*, 178(1–2), 45–60.

Dooley, R. B., and Chexal, V. K. (2000). "Flow-accelerated corrosion of pressure vessels in fossil plants." *Int. J. Press. Vessel. Pip.*, 77(2–3), 85–90.

Du, C. W., Li, X. G., Liang, P., Liu, Z. Y., Jia, G. F., and Cheng, Y. F. (2009). "Effects of Microstructure on Corrosion of X70 Pipe Steel in an Alkaline Soil." *J. Mater. Eng. Perform.*, 18(2), 216–220.

Dunne, D. P., Hejazi, D., Saleh, A. A., Haq, A. J., Calka, A., and Pereloma, E. V. (2016). "Investigation of the effect of electrolytic hydrogen charging of X70 steel: I. The effect of microstructure on hydrogen-induced cold cracking and blistering." *Int. J. Hydrogen Energy*, 41(28), 12411–12423.

Durnie, W., Marco, R. De, Jefferson, A., and Kinsella, B. (1999). "Development of a Structure-Activity Relationship for Oil Field Corrosion Inhibitors." *J. Electrochem. Soc.*, 146(5), 1751.

Dutta, P., Saha, S. K., Nandi, N., and Pal, N. (2016). "Numerical study on flow

separation in 90° pipe bend under high Reynolds number by k-ε modelling." *Eng. Sci. Technol. an Int. J.*, 19(2), 904–910.

Efird, K. D. (2011a). "Flow Effects on Corrosion." *Uhlig's Corros. Handb.*, R. W. REVIE, ed., Hoboken, New Jersey: John Wiley & Sons, Inc., 203–213.

Efird, K. D. (2011b). "Controlling Flow Effects on Corrosion." *Uhlig's Corros. Handb.*, R. W. Revie, ed., Hoboken, New Jersey: John Wiley & Sons, Inc., 903–905.

Efird, K. D. (2011c). "Testing for Flow Effects on Corrosion." *Uhlig's Corros. Handb.*, R. W. Revie, ed., Hoboken, New Jersey: John Wiley & Sons, Inc., 1059–1062.

Efird, K. D., Wright, E. J., Boros, J. A., and Hailey, T. G. (1993). "Correlation of steel corrosion in pipe flow with jet impingement and rotating cylinder tests." *Corrosion*, 49(12), 992–1003.

El-Gammal, M., Mazhar, H., Cotton, J. S., Shefski, C., Pietralik, J., and Ching, C. Y. (2010). "The hydrodynamic effects of single-phase flow on flow accelerated corrosion in a 90-degree elbow." *Nucl. Eng. Des.*, 240(6), 1589–1598.

Elemuren, R., Evitts, R., Oguocha, I., Kennell, G., Gerspacher, R., and Odeshi, A. (2018). "Slurry erosion-corrosion of 90° AISI 1018 steel elbow in saturated potash brine containing abrasive silica particles." *Wear*, 410–411(June), 149–155.

Elemuren, R., Evitts, R., Oguocha, I. N. A., Kennell, G., Gerspacher, R., and Odeshi, A. G. (2020). "Full factorial, microscopic and spectroscopic study of erosion-corrosion of AISI 1018 steel elbows in potash brine-sand slurry." *Tribol. Int.*, 142(September 2019), 105989.

Elemuren, R., Tamsaki, A., Evitts, R., Oguocha, I. N. A., Kennell, G., Gerspacher, R., and Odeshi, A. (2019). "Erosion-corrosion of 90° AISI 1018 steel elbows in potash slurry: Effect of particle concentration on surface roughness." *Wear*, 430–431(March), 37–49.

Gheisari, R., and Polycarpou, A. A. (2018). "Three-body abrasive wear of hard coatings: Effects of hardness and roughness." *Thin Solid Films*, 666(September), 66–75.

Grzesik, W., Rech, J., and Żak, K. (2015). "Characterization of surface textures generated on hardened steel parts in high-precision machining operations." *Int. J. Adv. Manuf. Technol.*, 78(9–12), 2049–2056.

Guo, S., Xu, L., Zhang, L., Chang, W., and Lu, M. (2016). "Characterization of corrosion scale formed on 3Cr steel in CO_2-saturated formation water." *Corros. Sci.*, 110, 123–133.

Gussev, M. N., and Leonard, K. J. (2019). "In situ SEM-EBSD analysis of plastic deformation mechanisms in neutron-irradiated austenitic steel." *J. Nucl. Mater.*, 517, 45–56.

Guzonas, D. A., Rochefort, P. A., and Turner, C. W. (1998). "Corrosion product characterisation by fibre optic Raman spectroscopy." *Third Int. Steam Gener. Heat Exch. Conf.*, Toronto, Ontario, Canada: Canadian Nuclear Society, 628–639.

Hanesch, M. (2009). "Raman spectroscopy of iron oxides and (oxy)hydroxides at low laser power and possible applications in environmental magnetic studies." *Geophys. J. Int.*, 177(3), 941–948.

Hargreaves, J. S. J. (2016). "Some considerations related to the use of the Scherrer equation in powder X-ray diffraction as applied to heterogeneous catalysts." *Catal. Struct. React.*, 2(1–4), 33–37.

Heitz, E. (1991). "Chemo-mechanical effects of flow on corrosion." *Corrosion*, 47(2), 135–145.

Hellström, L. H. O., Sinha, A., and Smits, A. J. (2011). "Visualizing the very-large-scale motions in turbulent pipe flow." *Phys. Fluids*, 23(1), 011703.

Heydari, M., and Javidi, M. (2012). "Corrosion inhibition and adsorption behaviour of an amido-imidazoline derivative on API 5L X52 steel in CO_2-saturated solution and synergistic effect of iodide ions." *Corros. Sci.*, 61, 148–155.

Hodgkiess, T., Neville, A., and Shrestha, S. (1999). "Electrochemical and mechanical interactions during erosion–corrosion of a high-velocity oxy-fuel coating and a stainless steel." *Wear*, 233–235, 623–634.

Holzwarth, U., and Gibson, N. (2011). "The Scherrer equation versus the 'Debye-Scherrer equation.'" *Nat. Nanotechnol.*, 6(9), 534–534.

Hu, X., Barker, R., Neville, A., and Gnanavelu, A. (2011). "Case study on erosion-corrosion degradation of pipework located on an offshore oil and gas facility." *Wear*, 271(9–10), 1295–1301.

Huang, H., Tian, J., Zhang, G., and Pan, Z. (2016). "The corrosion of X52 steel at an elbow of loop system based on array electrode technology." *Mater. Chem. Phys.*, 181, 312–320.

Ilman, M. N., and Kusmono. (2014). "Analysis of internal corrosion in subsea oil pipeline." *Case Stud. Eng. Fail. Anal.*, 2(1), 1–8.

Iordanova, I., Antonov, V., and Gurkovsky, S. (2002). "Changes of microstructure and mechanical properties of cold-rolled low carbon steel due to its surface treatment by Nd:glass pulsed laser." *Surf. Coatings Technol.*, 153(2–3), 267–275.

Islam, A., and Farhat, Z. N. (2013). "The synergistic effect between erosion and corrosion of API pipeline in CO_2 and saline medium." *Tribiology Int.*, 68, 26–34.

Islam, M. A., and Farhat, Z. (2017). "Erosion-corrosion mechanism and comparison of erosion-corrosion performance of API steels." *Wear*, 376–377, 533–541.

ISO 25178, 2. (2012). "Geometrical product specifications (GPS) — Surface texture: Areal — Part 2: Terms, definitions and surface texture parameters."

Jayaroopa, P., Ajay Kumar, K., and Vasanth Kumar, G. (2013). "Synthesis of 2,5-disubstituted-1,3,4-oxadiazoles using ethyl oleate as precursor." *Int. J. ChemTech Res.*, 5(5), 2516–2520.

Jiang, S., Chai, F., Su, H., and Yang, C. (2017). "Influence of chromium on the flow-accelerated corrosion behavior of low alloy steels in 3.5% NaCl solution." *Corros. Sci.*, 123(September 2016), 217–227.

Jiang, X., Zheng, Y. G., and Ke, W. (2005). "Effect of flow velocity and entrained sand on inhibition performances of two inhibitors for CO_2 corrosion of N80

steel in 3% NaCl solution." *Corros. Sci.*, 47(11), 2636–2658.

Jones, D. A. (1996). *Principles and Prevention of Corrosion*. Upper Saddle River, NJ: Prentice Hall.

Jovancicevic, V. (1999). "Molecular modeling of the inhibition of mild steel carbon dioxide corrosion by imidazolines." *Corrosion*, 55(3), 259–267.

Ju, J.-B. B., Lee, J.-S. S., Jang, J.-I. Il, Kim, W.-S. S., and Kwon, D. (2002). "Metallurgical and mechanical features of API 5L X65 pipeline steel weldment." *Proc. Int. Pipeline Conf. IPC*, A, 429–435.

Kain, V. (2014). "Flow accelerated corrosion: Forms, mechanisms and case studies." *Procedia Eng.*, 86, 576–588.

Kain, V., Roychowdhury, S., Ahmedabadi, P., and Barua, D. K. (2011). "Flow accelerated corrosion: Experience from examination of components from nuclear power plants." *Eng. Fail. Anal.*, 18(8), 2028–2041.

Karami, M. (2012). "Review of corrosion role in gas pipeline and some methods for preventing it." *J. Press. Vessel Technol. Trans. ASME*, 134(5).

Katritsis, D., Kaiktsis, L., Chaniotis, A., Pantos, J., Efstathopoulos, E. P., and Marmarelis, V. (2007). "Wall Shear Stress: Theoretical Considerations and Methods of Measurement." *Prog. Cardiovasc. Dis.*, 49(5), 307–329.

Kayali, Y., and Anaturk, B. (2013). "Investigation of electrochemical corrosion behavior in a 3.5wt.% NaCl solution of boronized dual-phase steel." *Mater. Des.*, 46, 776–783.

Kennedy, J. L. (1993). *Oil and Gas Pipeline Fundamentals*. PennWell Books.

Khan, P. F., Shanthi, V., Babu, R. K., Muralidharan, S., and Barik, R. C. (2015). "Effect of benzotriazole on corrosion inhibition of copper under flow conditions." *J. Environ. Chem. Eng.*, 3(1), 10–19.

Khan, R., Ya, H. H., and Pao, W. (2019). "An Experimental Study on the Erosion-Corrosion Performance of AISI 1018 Carbon Steel and AISI 304L Stainless Steel 90-Degree Elbow Pipe." *Metals (Basel).*, 9(1260), 1–15.

Khayatan, N., Ghasemi, H. M., and Abedini, M. (2018). "Study of Erosion-Corrosion and Corrosion Behavior of Commercially Pure-Ti during Slurry Erosion." *J. Tribol.*, 140(6), 061609.

Kim, B.-K., and Szpunar, J. A. (2009). "Orientation Imaging Microscopy in Research on High Temperature Oxidation." *Electron Backscatter Diffr. Mater. Sci.*, A. J. Schwartz, M. Kumar, B. L. Adams, and D. P. Field, eds., New York, USA: Springer US, 361–393.

Kim, J., Yadav, M., and Kim, S. (2014). "Characteristics of secondary flow induced by 90-degree elbow in turbulent pipe flow." *Eng. Appl. Comput. Fluid Mech.*, 8(2), 229–239.

Kiosidou, E. D., Karantonis, A., Pantelis, D. I., Silva, E. R., and Bordado, J. C. M. (2017). "Rust morphology characterization of silicone-based marine antifouling paints after salt spray test on scribed specimens." *J. Coatings Technol. Res.*, 14(2), 333–345.

Kitahara, H., Ueji, R., Tsuji, N., and Minamino, Y. (2006). "Crystallographic features of lath martensite in low-carbon steel." *Acta Mater.*, 54(5), 1279–1288.

Klug, H. P., and Alexander, L. E. (1974). *X-Ray Diffraction Procedures: For Polycrystalline and Amorphous Materials*. Wiley.

Kostic, M. M. (1996). "Manufacture, Properties, and Installation of X80 (550 MPa) Gas Transmission Linepipe." *Vol. 1 Regul. Codes, Stand. Curr. Issues; Mater. Corros. Integr.*, American Society of Mechanical Engineers, 203–207.

Krastev, D. (2012). "Improvement of Corrosion Resistance of Steels by Surface Modification." *Corros. Resist.*, H. Shih, ed., Rijeka, Croatia: InTech, 295–316.

Kusinski, J., Kac, S., Kopia, A., Radziszewska, A., Rozmus-Górnikowska, M., Major, B., Major, L., Marczak, J., and Lisiecki, A. (2012). "Laser modification of the materials surface layer – a review paper." *Bull. Polish Acad. Sci. Tech. Sci.*, 60(4), 711–728.

Kwok, C. T., Cheng, F. T., and Man, H. C. (2007). "Microstructure and

corrosion behavior of laser surface-melted high-speed steels." *Surf. Coatings Technol.*, 202(2), 336–348.

L. Riggs Jr, O. (1973). "Theoretical Aspects of Corrosion Inhibitors and Inhibition." *Corros. Inhib.*, C. C. Nathan, ed., Houston, TX: National Association of Corrosion Engineers (NACE), 7–27.

Lakshmi, M. R., and Kumar, V. D. (2015). "Anthropogenic hazard and disaster relief operations : A case study of GAIL pipeline blaze in east Godavari of A . P." *Procedia - Soc. Behav. Sci.*, 189, 198–207.

Lavigne, O., Kotousov, A., and Luzin, V. (2017). "Microstructural, mechanical, texture and residual stress characterizations of X52 pipeline steel." *Metals (Basel).*, 7(8), 1–10.

Li, C., Wang, Y., and Han, B. (2011). "Microstructure, hardness and stress in melted zone of 42CrMo steel by wide-band laser surface melting." *Opt. Lasers Eng.*, 49(4), 530–535.

Li, J., Sun, C., Shuang, S., Roostaei, M., Fattahpour, V., Mahmoudi, M., Zeng, H., and Luo, J. L. (2019). "Investigation on the flow-induced corrosion and degradation behavior of underground J55 pipe in a water production well in the Athabasca oil sands reservoir." *J. Pet. Sci. Eng.*, 182(July), 106325.

LI, W., FU, A., TIAN, Y., JU, Y., XUE, M., YIN, C., and ZHANG, Q. (2021). "Flow Corrosion Behavior of X100 Pipeline Steel in Simulated Formation Water." *Electrochemistry*, 89(1), 59–66.

Lin, C. H., and Ferng, Y. M. (2014). "Predictions of hydrodynamic characteristics and corrosion rates using CFD in the piping systems of pressurized-water reactor power plant." *Ann. Nucl. Energy*, 65, 214–222.

Liu, F. G., Du, M., Zhang, J., and Qiu, M. (2009). "Electrochemical behavior of Q235 steel in saltwater saturated with carbon dioxide based on new imidazoline derivative inhibitor." *Corros. Sci.*, 51(1), 102–109.

Liu, H., Xu, D., Dao, A. Q., Zhang, G., Lv, Y., and Liu, H. (2015). "Study of

corrosion behavior and mechanism of carbon steel in the presence of Chlorella vulgaris." *Corros. Sci.*, 101, 84–93.

Lopes-Sesenes, R., Dominguez-Patiño, G. F., Gonzalez-Rodriguez, J. G., and Uruchurtu-Chavarin, J. (2013). "Effect of flowing conditions on the corrosion inhibition of carbon steel by extract of buddleia perfoliata." *Int. J. Electrochem. Sci.*, 8(1), 477–489.

Lu, B. T., and Luo, J. L. (2015). "Correlation between surface-hardness degradation and erosion resistance of carbon steel - Effects of slurry chemistry." *Tribol. Int.*, 83, 146–155.

Luo, Z. J., Shen, J. C., Su, H., Ding, Y. H., Yang, C. F., and Zhu, X. (2010). "Effect of substructure on toughness of lath martensite/bainite mixed structure in low-carbon steels." *J. Iron Steel Res. Int.*, 17(11), 40–48.

Majumdar, J. D., and Manna, I. (1999). "Laser surface alloying of AISI 304-stainless steel with molybdenum for improvement in pitting and erosion-corrosion resistance." *Mater. Sci. Eng. A*, 267(1), 50–59.

Martino, S. F. Di, and Thewlis, G. (2014). "Transformation characteristics of ferrite/carbide aggregate in continuously cooled, low carbon-manganese steels." *Metall. Mater. Trans. A Phys. Metall. Mater. Sci.*, 45(2), 579–594.

Masoumi, M., Echeverri, E. A. A., Tschiptschin, A. P., and Goldenstein, H. (2019). "Improvement of wear resistance in a pearlitic rail steel via quenching and partitioning processing." *Sci. Rep.*, 9(1), 7454.

Masoumi, M., Silva, C. C., Béreš, M., Ladino, D. H., and Abreu, H. F. G. de. (2017). "Role of crystallographic texture on the improvement of hydrogen-induced crack resistance in API 5L X70 pipeline steel." *Int. J. Hydrogen Energy*, 42(2), 1318–1326.

Miranda, M. A. R., and Sasaki, J. M. (2018). "The limit of application of the Scherrer equation." *Acta Crystallogr. Sect. A Found. Adv.*, 74(1), 54–65.

Mistry, B. D. (2009). "Infrared Spectroscopy." *A Handb. Spectrosc. data Chem.*

- *UV, IR, PMR, 13CNMR mass Spectrosc.*, Jaipur, India: Oxford Book Company, 26–63.

Mohtadi-Bonab, M. A., Eskandari, M., Karimdadashi, R., and Szpunar, J. A. (2017). "Effect of different microstructural parameters on hydrogen induced cracking in an API X70 pipeline steel." *Met. Mater. Int.*, 23(4), 726–735.

Mudali, U. K., and Dayal, R. K. (1992). "Improving intergranular corrosion resistance of sensitized type 316 austenitic stainless steel by laser surface melting." *J. Mater. Eng. Perform.*, 1(3), 341–345.

Muhammadu, M. M., Md Sheriff, J., and Hamzahb, E. (2013). "Effect of flow pattern at pipe bends on corrosion behaviour of low carbon steek and its challenges." *J. Teknol. (Sciences Eng.*, 63(1), 55–65.

Murdock, J. W. (2006). "Mechanics of fluids." *Marks. Stand. Handb. Mech. Eng.*, E. Avallone, T. Baumeister, and A. Sadegh, eds., New York: McGraw-Hill, 3–43.

Muthanna, B. G. N., Amara, M., Meliani, M. H., Mettai, B., Božić, Ž., Suleiman, R., and Sorour, A. A. (2019). "Inspection of internal erosion-corrosion of elbow pipe in the desalination station." *Eng. Fail. Anal.*, 102, 293–302.

NACE/ASTM. (2012). "NACE/ASTM G193-12d, Standard Terminology and Acronyms Relating to Corrosion." *NACE Houston. Tx*.

Nam, N. D., Somers, A., Mathesh, M., Seter, M., Hinton, B., Forsyth, M., and Tan, M. Y. J. (2014). "The behaviour of praseodymium 4-hydroxycinnamate as an inhibitor for carbon dioxide corrosion and oxygen corrosion of steel in NaCl solutions." *Corros. Sci.*, 80, 128–138.

Neville, A., and Wang, C. (2009). "Erosion-corrosion mitigation by corrosion inhibitors-An assessment of mechanisms." *Wear*, 267(1–4), 195–203.

Nishiyama, Z. (1978). *Martensitic Transformation*. (M. E. Fine, M. Meshii, and C. M. Wayman, eds.), New York, USA: Academic Press.

Obanijesu, E. O. (2009). "Modeling the H_2S contribution to internal corrosion

rate of natural gas pipeline." *Energy Sources, Part A Recover. Util. Environ. Eff.*, 31(4), 348–363.

Oguzie, E. E., Li, Y., and Wang, F. H. (2007). "Corrosion inhibition and adsorption behavior of methionine on mild steel in sulfuric acid and synergistic effect of iodide ion." *J. Colloid Interface Sci.*, 310(1), 90–98.

Okafor, P. C., Liu, X., and Zheng, Y. G. (2009). "Corrosion inhibition of mild steel by ethylamino imidazoline derivative in CO_2-saturated solution." *Corros. Sci.*, 51(4), 761–768.

Ossai, C. I., Boswell, B., and Davies, I. J. (2015). "Pipeline failures in corrosive environments - A conceptual analysis of trends and effects." *Eng. Fail. Anal.*, 53, 36–58.

Pagani, L., Qi, Q., Jiang, X., and Scott, P. J. (2017). "Towards a new definition of areal surface texture parameters on freeform surface." *Measurement*, 109, 281–291.

Palacios, C. A. (2016). *Corrosion and Asset Integrity Management for Upstream Installations in the Oil/Gas Industry: The Journey of a Corrosion/Integrity Engineer - Real Life Experiences*. Basenji Studios, LLC, USA.

Papavinasam, S. (2014a). "Oil and Gas Industry Network." *Corros. Control Oil Gas Ind.*, Oxford, UK: Elsevier, 41–131.

Papavinasam, S. (2014b). "Mitigation – Internal Corrosion." *Corros. Control Oil Gas Ind.*, 1st, ed., Oxford, UK: Elsevier, 361–424.

Popoola, L. T., Grema, A. S., Latinwo, G. K., Gutti, B., and Balogun, A. S. (2013). "Corrosion problems during oil and gas production and its mitigation." *Int. J. Ind. Chem.*, 4(1), 35.

Postlethwaite, J., and Nesic, S. (2011). "Erosion–Corrosion in Single- and Multiphase Flow." *Uhlig's Corros. Handb.*, R. W. Revie, ed., Hoboken, New Jersey: John Wiley & Sons, Inc., 215–227.

Poulson, B. (1999). "Complexities in predicting erosion corrosion." *Wear*, 233–235, 497–504.

Qi, Q., Li, T., Scott, P. J., and Jiang, X. (2015). "A Correlational Study of Areal Surface Texture Parameters on Some Typical Machined Surfaces." *Procedia CIRP*, 27, 149–154.

Quaraishi, M. A., Jamal, D., and Tariq Saeed, M. (2000). "Fatty acid derivatives as corrosion inhibitors for mild steel and oil-well tubular steel in 15% boiling hydrochloric acid." *J. Am. Oil Chem. Soc.*, 77(3), 265–268.

Quraishi, M. A., and Ansari, F. A. (2003). "Inhibitive effect of FA derivatives on mild steel corrosion in the presence of formic acid." *J. Am. Oil Chem. Soc.*, 80(7), 705–710.

Rai, R., Triloki, T., and Singh, B. K. (2016). "X-ray diffraction line profile analysis of KBr thin films." *Appl. Phys. A*, 122(8), 774.

Raja, P. B., and Sethuraman, M. G. (2008). "Natural products as corrosion inhibitor for metals in corrosive media - A review." *Mater. Lett.*, 62(1), 113–116.

Ralston, K. D., and Birbilis, N. (2010). "Effect of grain size on corrosion: A review." *Corrosion*, 66(7), 0750051–07500513.

Ravikumar, V. V., and Kumaran, S. (2018). "Microstructure and corrosion behaviour of precipitation hardened and thermo-mechanical treated high strength Al-12Zn-3Mg-2.5Cu alloy." *Anti-Corrosion Methods Mater.*, 65(1), 79–86.

Sant'anna, P. C., Rizzo, E. M. S., Gomes, S. I. N., and Ferreira, I. (2002). "Mechanical Properties of Api 5L X65 Steel Submited To Intercritical Heat Treatments." *XV CBECiMat - Brazilian Congr. Mater. Sci. Eng.*, Natal (RN), Brasil: Univ. Fed. de São Carlos, 2659–2665.

Sastri, V. S. (2011). "Adsorption in Corrosion Inhibition." *Green Corros. Inhib. - Theory Pract.*, Hoboken, New Jersey: John Wiley & Sons, Inc., 108–110.

Sauvage, X., Breton, J. . Le, Guillet, A., Meyer, A., and Teillet, J. (2003). "Phase transformations in surface layers of machined steels investigated by X-ray diffraction and Mössbauer spectrometry." *Mater. Sci. Eng. A*, 362(1–2), 181–186.

Schmitt, G., and Bakalli, M. (2008). "Advanced models for erosion corrosion

and its mitigation." *Mater. Corros.*, 59(2), 181–192.

Schmitt, H. G., and Bakalli, M. (2009). "Flow Assisted Corrosion." *Shreir's Corros.*, R. A. Cottis and T. J. A. Richardson, eds., Amsterdam, Netherlands: Elsevier Science, 954–987.

Schwarzer, R. A., Field, D. P., Adams, B. L., Kumar, M., and Schwartz, A. J. (2009). "Present State of Electron Backscatter Diffraction and Prospective Developments." *Electron Backscatter Diffr. Mater. Sci.*, A. J. Schwartz, M. Kumar, B. L. Adams, and D. P. Field, eds., New York, USA: Springer US, 1–19.

Shabarchin, O., and Tesfamariam, S. (2016). "Internal corrosion hazard assessment of oil & gas pipelines using Bayesian belief network model." *J. Loss Prev. Process Ind.*, 40, 479–495.

Shalaby, A. I. (2018a). "Flow Resistance Equations." *Fluid Mech. Civ. Environ. Eng.*, J. Plant, ed., Boca Raton, Florida, USA: CRC Press, 643–726.

Shalaby, A. I. (2018b). "Pipe Flow." *Fluid Mech. Civ. Environ. Eng.*, J. Plant, ed., Boca Raton, Florida, USA: CRC Press, 919–1113.

Shariff, S. M., Pal, T. K., Padmanabham, G., and Joshi, S. V. (2010). "Sliding wear behaviour of laser surface modified pearlitic rail steel." *Surf. Eng.*, 26(3), 199–208.

Sherif, E. S. M., and Almajid, A. A. (2015). "Electrochemical corrosion behavior of API X-70 5L grade steel in 4.0 wt. % sodium chloride solutions after different immersion periods of time." *Int. J. Electrochem. Sci.*, 10(1), 34–45.

Shi, G. (2013). "Research and application on laser surface modification of sucker rod and tubing." *China Univ. Pet. Qingdao, China*.

Shin, S. Y., Hwang, B., Lee, S., Kim, N. J., and Ahn, S. S. (2007). "Correlation of microstructure and charpy impact properties in API X70 and X80 line-pipe steels." *Mater. Sci. Eng. A*, 458(1–2), 281–289.

Shook, C. A., and Roco, M. C. (1991). "Basic Concepts for Single-Phase Fluids and Particles." *Slurry Flow*, Elsevier, 1–25.

Shukla, R., Ghosh, S. K., Chakrabarti, D., and Chatterjee, S. (2013). "Microstructure, texture, property relationship in thermo-mechanically processed ultra-low carbon microalloyed steel for pipeline application." *Mater. Sci. Eng. A*, 587, 201–208.

Shukla, S. K., Kumar, S., De, S., Bhakat, A. K., and Saxena, A. (2016). "Development of API X70 Grade Hot Rolled (HR) Coils for Spiral Welded (SW) Pipes." 5(1), 9–14.

Si, X., Si, H., Li, M., Zhang, R., and Zhou, K. (2020). "Investigation of corrosion behavior at elbow by array electrode and computational fluid dynamics simulation." *Mater. Corros.*, (March), 1–14.

Si, X., Zhang, R., Xu, Q., and Zhou, K. (2019). "Effects of local velocity components on flow-accelerated corrosion at 90° elbow." *Mater. Res. Express*, 6(1).

Sivanandham, N., Rajadurai, A., Shariff, S. M., Senthilselvan, J., and Mahalingam, A. (2013). "Microstructural and corrosion resistance studies on SUS 420F and EN32B steels under surface treatment by high power diode laser." *J. Surf. Sci. Technol.*, 29(3–4), 1–11.

Sivanandham, N., Rajadurai, A., Shariff, S. M., Senthilselvan, J., and Mahalingam, A. (2017). "Microstructure, mechanical properties and corrosion resistance of laser surface melted EN353 low carbon low alloy steel." *Int. J. Surf. Sci. Eng.*, 11(2), 118–132.

Sun, J., Sun, C., Zhang, G., Li, X., Zhao, W., Jiang, T., Liu, H., Cheng, X., and Wang, Y. (2016). "Effect of O_2 and H_2S impurities on the corrosion behavior of X65 steel in water-saturated supercritical CO_2 system." *Corros. Sci.*, 107, 31–40.

Synetos, A., and Tousoulis, D. (2018). "Invasive Imaging Techniques." *Coron. Artery Dis.*, D. Tousoulis, ed., Academic Press, Elsevier, 359–376.

Takahashi, A., and Iino, M. (1996). "Thermo-mechanical Control Process as a Tool to Grain-refine the Low Manganese Containing Steel for Sour Service Line Pipe." *ISIJ Int.*, 36(2), 235–240.

Tang, C. H., Cheng, F. T., and Man, H. C. (2004a). "Improvement in cavitation erosion resistance of a copper-based propeller alloy by laser surface melting." *Surf. Coatings Technol.*, 182(2–3), 300–307.

Tang, C. H., Cheng, F. T., and Man, H. C. (2004b). "Effect of laser surface melting on the corrosion and cavitation erosion behaviors of a manganese–nickel–aluminium bronze." *Mater. Sci. Eng. A*, 373(1–2), 195–203.

Thibeau, R. J., Brown, C. W., and Heidersbach, R. H. (1978). "Raman Spectra of Possible Corrosion Products of Iron." *Appl. Spectrosc.*, 32(6), 532–535.

Usman, B. J., Umoren, S. A., and Gasem, Z. M. (2017). "Inhibition of API 5L X60 steel corrosion in CO_2-saturated 3.5% NaCl solution by tannic acid and synergistic effect of KI additive." *J. Mol. Liq.*, 237(November), 146–156.

Vera, R., Vinciguerra, F., and Bagnara, M. (2015). "Comparative study of the behavior of API 5L-X65 grade steel and ASTM A53-B grade steel against corrosion in seawater." *Int. J. Electrochem. Sci.*, 10(8), 6187–6198.

Verlinden, B., Driver, J., Samajdar, I., and Doherty, R. (2007). *Thermo-Mechanical Processing of Metallic Materials*. (R. W. Cahn, ed.), Oxford, UK: Elsevier Ltd.

Verma, H. R. (2007). *Atomic and Nuclear Analytical Methods*. Springer-Verlag Berlin Heidelberg.

Vilar, R. (2012). "Laser surface modification of steels and cast irons for corrosion resistance." *Laser Surf. Modif. Alloy. Corros. Eros. Resist.*, C. T. Kwok, ed., Cambridge, UK: Woodhead Publishing, 3–9.

Villalobos, J. C., Del-Pozo, A., Campillo, B., Mayen, J., and Serna, S. (2018). "Microalloyed steels through history until 2018: Review of chemical composition, processing and hydrogen service." *Metals (Basel).*, 8(5).

Visscher, M., and Struik, K. G. (1994). "Optical profilometry and its application to mechanically inaccessible surfaces Part I: Principles of focus error detection." *Precis. Eng.*, 16(3), 192–198.

Vora, H. D., and Dahotre, N. B. (2013). "Laser Surface Heat Treatment and Modification." *Adv. Mater. Process. (ASM Int.*, 171(11), 45–47.

Waikar, R. A., and Guo, Y. B. (2008). "A comprehensive characterization of 3D surface topography induced by hard turning versus grinding." *J. Mater. Process. Technol.*, 197(1–3), 189–199.

Walczak, M., Sharifi, S., and Stack, M. M. (2020). "On a multiphysics approach to modelling the erosion – enhanced corrosion of low – alloy carbon steel in chloride containing environments." *Corros. Sci.*, 176(November (109045)).

Wang, S., Ren, C., Sun, Y., Yang, X., and Tu, J. (2016). "A Study on the instantaneous turbulent flow field in a 90-degree elbow pipe with circular section." *Sci. Technol. Nucl. Install.*, 2016, 1–8.

Wang, X. Y., and Li, D. Y. (2003). "Mechanical , electrochemical and tribological properties of nano-crystalline surface of 304 stainless steel." 255, 836–845.

Weske, J. R. (1948). *Experimental Investigation of Velocity Distributions Downstream of single Duct Bends. Natl. Advis. Comm. Aeronaut.*, Washington: NACA.

Wood, R. J. K. (2007). "6.09 - Erosion/Corrosion." *Compr. Struct. Integr.*, Elsevier Ltd, 395–427.

Wood, R. J. K. (2009). "Tribocorrosion." *Shreir's Corros.*, T. J. A. Richardson, ed., Elsevier, 1005–1050.

Yaro, A. S., Abdul-Khalik, K. R., and Khadom, A. A. (2015). "Effect of CO_2 corrosion behavior of mild steel in oilfield produced water." *J. Loss Prev. Process Ind.*, 38, 24–38.

Yilbas, B. S., Patel, F., and Karatas, C. (2013). "Laser controlled melting of HSLA steel surface with presence of B_4C particles." *Appl. Surf. Sci.*, 282, 601–606.

Zai, L., Zhang, C., Wang, Y., Guo, W., Wellmann, D., Tong, X., and Tian, Y. (2020). "Laser Powder Bed Fusion of Precipitation-Hardened Martensitic Stainless Steels: A Review." *Metals (Basel).*, 10(2), 255.

Zeng, L., Chen, G., and Chen, H. (2020). "Comparative Study on Flow-

Accelerated Corrosion and Erosion–Corrosion at a 90° Carbon Steel Bend." *Materials (Basel).*, 13(7), 1780.

Zeng, L., Shuang, S., Guo, X. P., and Zhang, G. A. (2016a). "Erosion-corrosion of stainless steel at different locations of a 90° elbow." *Corros. Sci.*, 111, 72–83.

Zeng, L., Zhang, G. A., and Guo, X. P. (2014). "Erosion-corrosion at different locations of X65 carbon steel elbow." *Corros. Sci.*, 85, 318–330.

Zeng, L., Zhang, G. A., and Guo, X. P. (2016b). "Effect of hydrodynamics on the inhibition effect of thioureido imidazoline inhibitor for the flow accelerated corrosion of X65 pipeline steel." *Corrosion*, 72(5), 598–614.

Zeng, L., Zhang, G. A., and Guo, X. P. (2017). "Hydrodynamic Effect on the Inhibition for the Flow Accelerated Corrosion of an Elbow." *Corros. Sci. Technol.*, 16(1), 23–30.

Zeng, L., Zhang, G. A., Guo, X. P., and Chai, C. W. (2015). "Inhibition effect of thioureidoimidazoline inhibitor for the flow accelerated corrosion of an elbow." *Corros. Sci.*, 90(1), 202–215.

Zhang, G. A., and Cheng, Y. F. (2009). "Corrosion of X65 steel in CO2-saturated oilfield formation water in the absence and presence of acetic acid." *Corros. Sci.*, 51(8), 1589–1595.

Zhang, G. A., and Cheng, Y. F. (2010). "Electrochemical characterization and computational fluid dynamics simulation of flow-accelerated corrosion of X65 steel in a CO2-saturated oilfield formation water." *Corros. Sci.*, 52(8), 2716–2724.

Zhang, G. A., and Cheng, Y. F. (2011). "Localized corrosion of carbon steel in a CO2-saturated oilfield formation water." *Electrochim. Acta*, 56(3), 1676–1685.

Zhang, G. A., Zeng, L., Huang, H. L., and Guo, X. P. (2013). "A study of flow accelerated corrosion at elbow of carbon steel pipeline by array electrode and computational fluid dynamics simulation." *Corros. Sci.*, 77, 334–341.

Zhang, J., and Guyot, F. (1999). "Experimental study of the bcc-fcc phase transformations in the Fe-rich system Fe-Si at high pressures." *Phys. Chem. Miner.*,

26(6), 419–424.

Zhang, P., Chen, Y., Xiao, W., Ping, D., and Zhao, X. (2016). "Twin structure of the lath martensite in low carbon steel." *Prog. Nat. Sci. Mater. Int.*, 26(2), 169–172.

Zhang, W., Zhou, M., Zhu, H., Tian, Y., Wang, K., Wei, J., Ji, F., Li, X., Li, Z., Zhang, P., and Wu, D. (2011a). "Tribological properties of oleic acid-modified graphene as lubricant oil additives." *J. Phys. D. Appl. Phys.*, 44(20), 205303.

Zhang, X., Xiao, K., Dong, C., Wu, J., Li, X., and Huang, Y. (2011b). "In situ Raman spectroscopy study of corrosion products on the surface of carbon steel in solution containing Cl^- and SO_4^{2-}." *Eng. Fail. Anal.*, 18(8), 1981–1989.

Zhao, J., and Chen, G. (2012). "The synergistic inhibition effect of oleic-based imidazoline and sodium benzoate on mild steel corrosion in a CO_2 saturated brine solution." *Electrochim. Acta*, 69, 247–255.

Zhao, J., Xiong, D., Gu, Y., Zeng, Q., and Tian, B. (2019). "A comparative study on the corrosion behaviors of X100 steel in simulated oilfield brines under the static and dynamic conditions." *J. Pet. Sci. Eng.*, 173(April 2018), 1109–1120.

Zhao, W., Wang, C., Zhang, T., Yang, M., Han, B., and Neville, A. (2016). "Effects of laser surface melting on erosion–corrosion of X65 steel in liquid–solid jet impingement conditions." *Wear*, 362–363, 39–52.

Zhao, Y., Zhou, F., Yao, J., Dong, S., and Li, N. (2015). "Erosion-corrosion behavior and corrosion resistance of AISI 316 stainless steel in flow jet impingement." *Wear*, 328–329, 464–474.

Zhilyaev, A. P., Nurislamova, G. V., Kim, B. K., Baró, M. D., Szpunar, J. A., and Langdon, T. G. (2003). "Experimental parameters influencing grain refinement and microstructural evolution during high-pressure torsion." *Acta Mater.*, 51(3), 753–765.

Zhong, X., Shang, T., Zhang, C., Hu, J., Zhang, Z., Zhang, Q., Yuan, X., Hou, D., Zeng, D., and Shi, T. (2020). "In situ study of flow accelerated corrosion and its mitigation at different locations of a gradual contraction of N80 steel." *J. Alloys Compd.*, 824, 153947.

Zhou, W., Apkarian, R., Wang, Z. L., and Joy, D. (2007). "Fundamentals of Scanning Electron Microscopy (SEM)." *Scanning Microsc. Nanotechnol.*, W. Zhou and Z. L. Wang, eds., New York, USA: Springer, 1–40.

Zhou, Y., Zhang, P., Zuo, Y., Liu, D., and Yan, F. (2017). "The structure and composition of corrosion product film and its relation to corrosion rate for carbon steels in CO_2 saturated solutions at different temperatures." *J. Braz. Chem. Soc.*, 28(12), 2490–2499.

LIST OF PUBLICATIONS

a) In Journals

1. Ajmal, T. S., Arya, S. B., and Udupa, K. R. (2019). "Effect of hydrodynamics on the flow accelerated corrosion (FAC) and electrochemical impedance behavior of line pipe steel for petroleum industry." *Int. J. Press. Vessel. Pip.*, 174(March), 42–53.

2. Ajmal, T. S., Arya, S. B., Thippeswamy, L. R., Quraishi, M. A., and Haque, J. (2020). "Influence of green inhibitor on flow-accelerated corrosion of API X70 line pipe steel in synthetic oilfield water." *Corros. Eng. Sci. Technol.*, 55(6), 487–496.

3. Ajmal, T. S., S.B. Arya, P. Maurya, S.M. Shariff. "Effect of laser surface melting on slurry erosion-corrosion of API X70 line pipe steel in synthetic oilfield slurry." *Corros. Sci.* (article under review).

4. Ajmal, T. S., S.B. Arya, P. Maurya, S.M. Shariff. "Influence of laser surface melting on flow accelerated corrosion of API X70 line pipe steel in synthetic oilfield water." *Surf. Coatings Technol.* (article submitted).

b) In Conferences

1. T. S. Ajmal, T. Baskaran, Abheepsit Raturi, K. R. Udupa, S. B. Arya, "Study of Flow Accelerated Corrosion at Elbow of 304 Stainless Steel Pipeline in Oil Field Water" Paper No. IC-23, International Corrosion Conference and Expo CORCON 2016 (NACE), 18-21 Sep. 2016, New Delhi, India.

2. T. S. Ajmal, T. Baskaran, K. R. Udupa, S. B. Arya, "Flow Accelerated Corrosion at 304 Stainless Steel Pipeline Elbow in Oil Field Water" Paper No. NTC2016-597, National Tribology Conference 2016, 8-10 Dec. 2016, IIT (BHU) Varanasi.

3. T. S. Ajmal, Shashi Bhushan Arya, K. Rajendra Udupa, Flow Accelerated Corrosion of API X70 Pipeline Steel in Oilfield Water, 5th CORSYM, 23-24 March 2018, IIT Madras, Chennai, India. *ISBN 9788193342824, 75-76*

4. T.S. Ajmal, Shashi Bhushan Arya, S.M. Shariff, Influence of laser surface modification on flow assisted corrosion (FAC) behaviour of API X70 steel in oilfield water, NMD-ATM-2019, Nov. 13-16, 2019, Trivandrum, India. *TCM-CRP23, Page No. 323*

BIODATA

PERSONAL INFORMATION

Name   : Ajmal T S

DOB   : 27-Nov-1986

Place of birth   : Kasaragod, Kerala

Languages known   : English, Hindi, Malayalam, Tamil

Gender   : Male

Marital status   : Married

Contact number   : +91 7899 344 365

Email id   : tsajmal@gmail.com

Address   : Thalayillathu (H), Kadumeni (P.O.),

Kasaragod, Kerala – 670511.

EDUCATION DETAILS

Qualification	Year	Institution/University
Ph.D.	Defended the thesis in October 2021	NITK, Surathkal
M.Tech. (Manufacturing Technology)	2012-2014	PRIST University, Thanjavur
B.E. (Mechanical Engineering)	2004-2008	Anna University, Chennai